MAGNETIC GUIDANCE OF COCHLEAR-IMPLANT ELECTRODE ARRAYS AT CLINICAL SCALE

by

Lisandro Leon

A dissertation submitted to the faculty of
The University of Utah
in partial fulfillment of the requirements for the degree of

Doctor of Philosophy

Department of Mechanical Engineering

The University of Utah

August 2017

The University of Utah Graduate School

STATEMENT OF DISSERTATION APPROVAL

The dissertation of **Lisandro Leon**
has been approved by the following supervisory committee members:

Jake J. Abbott ,	Chair(s)	**24 April 2017** Date Approved
Frank M. Warren ,	Member	**28 April 2017** Date Approved
Robert W. Hitchcock ,	Member	**24 April 2017** Date Approved
John M. Hollerbach ,	Member	**24 April 2017** Date Approved
Stephen A. Mascaro ,	Member	**24 April 2017** Date Approved

by **Tim Ameel** , Chair/Dean of
the Department/College/School of **Mechanical Engineering**
and by **David B. Kieda** , Dean of The Graduate School.

ABSTRACT

For many with severe-to-profound hearing loss, a condition in which the cochlea is unable to convert sound vibration into neural information to the brain, the cochlear implant has become the standard treatment. The goal of a cochlear-implant system is to bypass the malfunctioned cochlea and directly stimulate the nerves responsible for hearing through an array of electrodes on a silicone-elastomer carrier. However, the insertion of the electrode arrays can often cause intracochlear damage and eliminate residual hearing. With increased focus on hearing preservation in cochlear implantation, methods to minimize intracochlear damage have become a priority in electrode-array insertions.

This dissertation explores the application of magnetic manipulation toward improved cochlear-implant electrode-array insertions. We start with initial 3-to-1 proof-of-concept experiments to demonstrate the feasibility of this approach. Then, to achieve relevancy at clinical scale, lateral-wall-type electrode-array models, used in the clinic, are slightly modified at the tip to include a tiny magnet. Next, a scala-tympani phantom is designed with both simulated cochleostomy and round-window openings to mimic both classes of insertions typically conducted. In particular, this is the first phantom to model a round-window opening and can be used reliably to simulate insertion forces in cadaver cochleae.

Electrode arrays are then magnetically guided through these phantoms with a statistically significant ($p < 0.05$) reduction in insertion forces, and by as much as 50% for some electrode-array models. In particular, guiding the electrode-array tip through the cochlear hook and the basal turn, in the same insertion, was demonstrated for the first time using this technology. All existing methods to guide the electrode array can only be accomplished for the basal turn.

Analysis is conducted to determine the optimal size and placement of a magnetic dipole-field source for use in the clinic. Its placement is determined to be consistently lateral to and anterior to the patient's cochlea. Its size depends on numerous factors including the patient, torque requirements, and registration error. Sensitivity curves summarizing

these factors are provided. The volume of the magnetic dipole-field source can be reduced by a factor of 5, on average, by moving it from the modiolar configuration originally proposed to this optimal configuration. We verify that magnetic forces do not pose any appreciable risk to the basilar membrane at the optimal configuration. Although patient-specific optimal configurations are characterized, a one-size-fits-all version is described that may be more practical and carries the benefit of substantial robustness to registration error.

For my long-suffering family

CONTENTS

LIST OF FIGURES

LIST OF TABLES

CHAPTER 1

INTRODUCTION

Hearing impairment affects 360 million people worldwide [1] and about 35 million people in the United States [2]. It is projected to to be the 9th leading contributor to global disease burden by 2030 with broad socioeconomic impact that includes economic hardship and low educational attainment [1]. Recommended interventions for hearing impairment are determined by the results of patient audiograms. Conventional hearing aids are most efficient for mild-to-moderate hearing loss but are ineffective for severe hearing loss in the high-frequency range (greater than 1 kHz) [3]. For this type of hearing loss, the only intervention is the cochlear implant.

There are approximately 219,000 recipients of cochlear implants worldwide [4], which makes it easily the most successful neural prosthetic device to date [5]. The goal of a cochlear-implant system is to bypass the malfunctioned cochlea and directly stimulate the nerves responsible for hearing. Because of the tonotopic organization of the cochlea, sound picked up by the microphone must be separated into specific frequency channels by the speech processor. The channels are then mapped to the appropriate electrodes based on their location inside the cochlea. Multiple electrodes are needed to reproduce the entire sound spectrum and are arranged in a linear array on a silicone carrier and inserted into the scala tympani chamber of the cochlea.

Despite the transformative success of cochlear implants, their utilization rate is still remarkably low. In the United States alone, there is an estimated 1.2 million potential candidates of cochlear implants [2]. Yet only about 71,000 individuals have received this intervention, 40% of which are children [4] who are at an educational disadvantage without such sensorineural hearing loss treatments [6, 7]. Such a low utilization rate (less than 6%) suggests that cochlear implants are not yet the standard-of-care that perhaps they could be. One postulated reason for this low utilization rate is the lack of specific

clinical guidelines addressing "best practices" regarding many factors in patient outcomes including residual hearing outcomes [2]. This seems relevant as many with hearing loss suffer from impairment that is characterized by normal-to-mild loss in the low-frequency region, with nearly complete deafness in the higher frequencies. The cochlear-implant community considered the presence of residual hearing to be a contraindication because compromised ipsilateral hearing was a typical outcome [8]. The reason is that the insertion of the electrode array can result in permanent loss of residual hearing, particularly if the electrode array perforates the basilar membrane and deviates into the adjacent scala [8,9]. At the time, no suitable intervention was available for these patients. They did not benefit much from conventional hearing aids as they are ineffective for high-frequency hearing loss. They were also excluded from the benefits of cochlear implants because of their residual low-frequency hearing.

In recent years, a third type of intervention has been advocated to address this specific market. It is known as electric-acoustic stimulation, and it combines electrical stimulation of high frequencies via a cochlear implant with acoustic stimulation of low frequencies via a hearing aid. By combining both electric and acoustic modalities, it is vital that the residual low-frequency hearing be preserved for effective results. This is not guaranteed as the insertion of the electrode array can often cause intracochlear damage if the insertion forces exceed the inherent strength of the tissue [5]. This has led some to advocate the use of shorter electrode arrays that are intended to be inserted only to an angular depth of 250°–300° [5, 10]. Due to the cochlea's tonotopic organization, this is sufficient to convey high frequencies (via electrical stimulation) while avoiding deeper insertions that may damage the patient's residual low-frequency hearing [11]. Recent advances have seen electric-acoustic stimulation confer improved hearing results over traditional cochlear implants in such areas as pitch and speech perception, listening with background noise, and music appreciation [12]. Moreover, this intervention has expanded the current patient population to include those who normally cannot receive cochlear implants but are beyond the scope of traditional hearing aids. It is also likely that the expansion of pediatric candidacy for cochlear implants [13] will further motivate the goal of atraumatic insertions, especially given that hearing preservation seems to occur more in children [14].

Methods to minimize trauma to preserve hearing have not just benefited those choos-

ing electric-acoustic stimulation. Evidence suggests that patients who opt for traditional cochler implants (i.e., electrical stimulation only) show improved outcomes when their hearing is preserved [15–17]. There is now overwhelming interest to minimize trauma and preserve residual hearing in cochlear implantation, whether in single or bimodal operation. Recommendations to minimize trauma to the cochlea can be broadly organized into (1) surgical techniques, (2) cochleostomy placement, and (3) electrode-array design [18]. Recommended surgical techniques include such things as avoidance of acoustic trauma using low-speed drills and the application of steroids to protect the organ of corti. These topics are beyond the scope of this project.

The first multichannel electrode arrays were straight and designed to rest on the lateral (i.e., outer) wall of the cochlea. Due to their stiffness, surgeons opted for cochleostomies for ease of insertion as the cochlear hook provided resistance early in the insertion process [19]. That is, prior to the development of more flexible electrode arrays, cochleostomies were in favor because stiffer multichannel electrode arrays required a straight route into the lumen to avoid the cochlear hook region [20]. While there are still many proponents of using cochleostomies [21], even when hearing preservation is desired [22], the primary benefits of using the round window for electrode-array insertions is direct entry into the scala tympani, at the outset, with minimal drilling [23]. This is guaranteed because the scala tympani terminates at the round window. Also, evidence from clinical practice indicates that using the round window for insertions produce a high percentage of complete scala-tympani placement [24]. Electrode arrays that are placed entirely within the scala tympani tend to produce better hearing outcomes [25].

In contrast, accurate placement of cochleostomies is mandatory to ensure the electrode array is initially inserted into the scala tympani. Unfortunately, it has been shown that there is a 20% probability that the cochleostomy will be sited incorrectly by practicing surgeons leading to potential misplacement of the electrode array into either the scala vestibuli or the vestibule from the very outset [26]. Even in cases where soft-surgery techniques are employed, cochleostomy sites may be different than originally intended [27]. This has renewed interest in using the round window for electrode-array insertions [28–31] with the recent literature favoring round window over cochleostomies when hearing preservation is the primary consideration [22, 32]. The electrode-array insertion is

known to cause intracochlear damage if the insertion forces exceed the inherent strength of the tissue [5]. The most traumatic damage occurs if the electrode array perforates the basilar membrane and deviates into the adjacent scala. The usual site for this is along the first turn, near 180°, where contact with the lateral wall sometimes deflects the electrode-array tip out-of-plane and into the basilar membrane [5, 33, 34]. This type of trauma is a strong predictor for permanent loss of residual hearing [9].

One approach has been to improve upon the insertion characteristics of the electrode arrays. Design of lateral-wall electrode arrays have considered parameters such as flexibility [35–37], dimensions [38–41], fabrication technique [42], and material selection [43]. In general, lateral-wall electrode arrays are designed to be thin and flexible so as to minimize trauma when the tip first contacts the lateral-wall of the cochlea.

Alternatively, perimodiolar electrode arrays have a preformed curvature designed to curl away from the lateral wall of the first turn and rest on the medial (i.e., inner) wall of the cochlea close to the modiolus. Prior to insertion, they are straightened with a stylet. During insertion, the electrode array is advanced off the stylet so that the preformed shape functions as a steering mechanism. Proper technique requires the stylet to be stabilized at the appropriate distance from the cochleostomy site so that the electrode array can avoid the lateral wall while being advanced. If done correctly, negligible insertion forces can be achieved while eliminating tip contact with the lateral wall [44–46]. In practice, scalar excursion is a common occurrence with these perimodiolar electrode arrays precisely at the location where it should be curling away from the lateral wall. This can happen if the stylet is stabilized deeper into the insertion than intended. Considerations for improving the insertion of perimodiolar electrode arrays have included insertion techniques [44, 46], alternatives to stylets [47], curling behavior [48], and automated robots [45, 49]. However, an additional complication arises when using perimodiolar electrode arrays through the round window. Recent evidence suggests that this may not be very safe [50–52]. A problem is that the stylet, which is needed to insert these devices, increases the overall thickness while reducing the flexibility, both of which is not suited for round-window approaches and may make it more difficult for the electrode array to pass through the cochlear hook [27,52]. Another finding is that early torsion of the electrode array during insertion always resulted in basilar membrane disruption [50]. In our opinion, early torsion twists the

electrode array so that it is no longer aligned properly to curl away from the lateral wall. If severe enough, the preformed shape directs the tip into the basilar membrane. In short, perimodiolar electrode arrays are designed to be used with the straight, initial trajectory accomplished through a cochleostomy.

In the clinic, major complications arising from just the insertion of the electrode array itself have been shown to occur in 3.8% of cochlear-implant surgeries [53]. If the insertions are automated, it seems reasonable that these types of complications may be reduced. Electrode arrays that are inserted manually, even by highly skilled surgeons, can exhibit a wide variability in insertion force application [49]. This variability can be greatly decreased using robot-assisted insertion techniques [49] where optimized path planning [54], insertion speed [55], and other insertion parameters can be more easily reproduced for repeatable insertions. Ideally, robotic-assisted insertions could be used to insert the electrode arrays already used in the clinic [45, 49].

Given the general success of perimodiolar electrode arrays, the desire to navigate the first turn of the cochlea has inspired many ideas. To make electrode arrays steerable typically requires mechanisms that make them inherently less flexible. In our opinion, this is undesirable. Mirzadeh et al. [56] designed a mechanism that positions the electrode array toward the medial wall after insertion, but the use of an external positioner has been shown to be traumatic in several temporal-bone studies [57]. Some are intended to be actively bent or steered during insertion to minimize insertion trauma [58–61], though only Zhang et al. [61] demonstrated insertion force reduction in their publication. This suggests that atraumatic insertions may not be easy to achieve with current prototypes to steer electrode arrays. The use of pneumatic actuation as suggested by Arcand et al. [58] brings an undesirable level of complexity to the electrode-array design. Some are difficult to reverse, once activated [56, 60], meaning that explantation can be difficult. Some require sufficient perilymph fluid to actuate [56, 59], which may be problematic if sufficient fluid is lost during surgery. These prototypes demonstrate the general challenge of developing steerable electrode arrays without increasing their stiffness. Attempts to navigate the electrode arrays through the cochlea typically require mechanical means that will decrease the flexibility of the electrode array, making it more unsafe if the navigation mechanism is not implemented correctly. This is particularly true if the electrode array is misaligned so

that the prototype's curvature direction is directed into the basilar membrane. This is the same problem disussed earlier regarding misaligned stylet-based electrode arrays due to torsion [50].

To address many of these concerns, we have developed a method to navigate a flexible, lateral-wall electrode array by embedding a magnet in the tip of the electrode array and guiding it through the scala tympani during insertion. Since adding a small magnet to the electrode-array tip does not fundamentally change the remainder of the electrode array, its stiffness is not increased, making it potentially safer than other steerable techniques. The advantage to this approach is that we can augment the inherent safety of thinner, flexible electrode arrays already being used clinically with the potential benefits of a steering capability. The electrode-array tip can be steered so as to avoid direct tip contact with the lateral wall at the first cochlear turn near 180 degrees, the site where most basilar membrane perforations occur [5,33]. In addition, the tip can also be steered to avoid direct tip contact with the medial wall at the cochlear hook, making it ideal for round-window insertions. To date, steerable electrode-array prototypes have only been designed to steer away from the lateral wall at the first cochlear turn and rightly have assumed cochleostomy insertions in approach. In our paradigm, the electrode array does not require a preformed shape or a preferred curvature direction. It can be designed completely symmetric about its long axis. The torque is applied "wirelessly", the magnitude and direction of which can be controlled through the motion of the external magnet. This eliminates the risk of misaligning the electrode array's curling mechanism toward the basilar membrane prior to steering. Finally, our approach can be robotically implemented as either a supervised automated process or a robotic system under surgeon manipulation, either of which should produce more repeatable insertions than manual insertions.

1.1 References

[1] S. D. Emmett and H. W. Francis, "The socioeconomic impact of hearing loss in u.s. adults," *Otol. Neurotol.*, vol. 36, no. 3, pp. 545–550, Mar 2015.

[2] D. L. Sorkin, "Cochlear implantation in the world's largest medical device market: utilization and awareness of cochlear implants in the united states," *Cochlear Implants Int.*, vol. 14 Suppl 1, pp. S4–12, Mar 2013.

[3] P. Van de Heyning and A. K. Punte, "Electric acoustic stimulation: A new era in

prosthetic hearing rehabilitation," *Adv. Otorhinolaryngol.*, vol. 67, pp. 1–5, 2010.

[4] National Institute on Deafness and Other Communication Disorders, "Fact sheet: Cochlear implants," 2011.

[5] F. G. Zeng, S. Rebscher, W. Harrison, X. Sun, and H. Feng, "Cochlear implants: System design, integration, and evaluation," *IEEE Reviews in Biomed. Eng.*, vol. 1, pp. 115–142, 2008.

[6] J. C. Blair, "The effects of mild sensorineural hearing loss on academic performance of young school-age children.," *Volta Review*, vol. 87, no. 2, pp. 87–93, 1985.

[7] F. H. Bess, J. Dodd-Murphy, and R. A. Parker, "Children with minimal sensorineural hearing loss: prevalence, educational performance, and functional status," *Ear and Hearing*, vol. 19, no. 5, pp. 339–354, 1998.

[8] A. P. Campbell, M. T. Dillon, C. A. Buchman, and O. F. Adunka, "Hearing preservation cochlear implantation," *Curr. Otorhinolaryngol. Rep.*, vol. 1, no. 2, pp. 69–79, 2013.

[9] G. B. Wanna, J. H. Noble, R. H. Gifford, M. S. Dietrich, A. D. Sweeney, D. Zhang, B. M. Dawant, A. Rivas, and R. F. Labadie, "Impact of intrascalar electrode location, electrode type, and angular insertion depth on residual hearing in cochlear implant patients: Preliminary results.," *Otol. Neurotol.*, vol. 36, no. 8, pp. 1343–1348, Sep 2015.

[10] B. J. Gantz, C. Turner, K. E. Gfeller, and M. W. Lowder, "Preservation of hearing in cochlear implant surgery: advantages of combined electrical and acoustical speech processing," *Laryngoscope*, vol. 115, no. 5, pp. 796–802, May 2005.

[11] O. Adunka and J. Kiefer, "Impact of electrode insertion depth on intracochlear trauma," *Otolaryngol. Head Neck Surg.*, vol. 135, no. 3, pp. 374–382, 2006.

[12] S. Irving, L. Gillespie, R. Richardson, D. Rowe, J. B. Fallon, and A. K. Wise, "Electroacoustic stimulation: now and into the future.," *Biomed. Res. Int.*, vol. 2014, pp. 350504, 2014.

[13] M. L. Carlson, D. P. Sladen, D. S. Haynes, C. L. Driscoll, M. D. DeJong, H. C. Erickson, L. W. Sunderhaus, A. Hedley-Williams, E. A. Rosenzweig, T. J. Davis, and R. H. Gifford, "Evidence for the expansion of pediatric cochlear implant candidacy.," *Otol. Neurotol.*, vol. 36, no. 1, pp. 43–50, Jan 2015.

[14] A. Anagiotos, N. Hamdan, R. Lang-Roth, A. Gostian, J. Lüers, K. Hüttenbrink, and D. Beutner, "Young age is a positive prognostic factor for residual hearing preservation in conventional cochlear implantation.," *Otol. Neurotol.*, vol. 36, no. 1, pp. 28–33, Jan 2015.

[15] I. A. Bruce, M. Felton, M. Lockley, C. Melling, S. K. Lloyd, S. R. Freeman, and K. M. J. Green, "Hearing preservation cochlear implantation in adolescents," *Otol. Neurotol.*, Aug 2014.

[16] M. L. Carlson, C. L. W. Driscoll, R. H. Gifford, G. J. Service, N. M. Tombers, B. J. Hughes-Borst, B. A. Neff, and C. W. Beatty, "Implications of minimizing trauma during conventional cochlear implantation," *Otol. Neurotol.*, vol. 32, no. 6, pp. 962–968, 2011.

[17] A. D'Elia, R. Bartoli, F. Giagnotti, and N. Quaranta, "The role of hearing preservation on electrical thresholds and speech performances in cochlear implantation," *Otol. Neurotol.*, vol. 33, no. 3, pp. 343–347, 2012.

[18] P. S. Roland, W. Gstöttner, and O. Adunka, "Method for hearing preservation in cochlear implant surgery," *Oper. Tech. Otolaryngol.*, vol. 16, no. 2, pp. 93–100, 2005.

[19] R. J.S. Briggs, M. Tykocinski, K. Stidham, and J. B. Roberson, "Cochleostomy site: implications for electrode placement and hearing preservation," *Acta Otolaryngol.*, vol. 125, no. 8, pp. 870–876, 2005.

[20] F. Hassepass, S. Bulla, W. Maier, R. Laszig, S. Arndt, R. Beck, L. Traser, and A. Aschendorff, "The new mid-scala electrode array: a radiologic and histologic study in human temporal bones," *Otol. Neurotol.*, vol. 35, no. 8, pp. 1415–20, Sep 2014.

[21] J. Addams-Williams, L. Munaweera, B. Coleman, R. Shepherd, and S. Backhouse, "Cochlear implant electrode insertion: in defence of cochleostomy and factors against the round window membrane approach," *Cochlear Implants Int.*, vol. 12 Suppl 2, pp. S36–9, Aug 2011.

[22] E. F. O'Connor and A. Fitzgerald, "Hearing preservation surgery: current opinions," *Adv. Otorhinolaryngol.*, vol. 67, pp. 108–115, 2010.

[23] C. Richard, J. N. Fayad, J. Doherty, and F. H. Linthicum Jr, "Round window versus cochleostomy technique in cochlear implantation: Histological findings," *Otol. Neurotol.*, vol. 33, no. 7, pp. 1181, 2012.

[24] I. Todt, G. Rademacher, J. Wagner, F. Göpel, D. Basta, E. Haider, and A. Ernst, "Evaluation of cochlear implant electrode position after a modified round window insertion by means of a 64-multislice ct," *Acta Otolaryngol.*, vol. 129, no. 9, pp. 966–70, Sep 2009.

[25] G. B. Wanna, J. H. Noble, M. L. Carlson, R. H. Gifford, M. S. Dietrich, D. S. Haynes, B. M. Dawant, and R. F. Labadie, "Impact of electrode design and surgical approach on scalar location and cochlear implant outcomes," *Laryngoscope*, 2014.

[26] O. F. Adunka, A. Radeloff, W. K. Gstoettner, H. C. Pillsbury, and C. A. Buchman, "Scala tympani cochleostomy ii: topography and histology," *Laryngoscope*, vol. 117, no. 12, pp. 2195–200, 2007.

[27] B. Fraysse, Á. R. Macías, O. Sterkers, S. Burdo, R. Ramsden, O. Deguine, T. Klenzner, T. Lenarz, M. M. Rodriguez, E. Von Wallenberg, and C. James, "Residual hearing conservation and electroacoustic stimulation with the nucleus 24 contour advance cochlear implant," *Otol. Neurotol.*, vol. 27, no. 5, pp. 624–633, 2006.

[28] R. J.S. Briggs, M. Tykocinski, J. Xu, F. Risi, M. Svehla, R. Cowan, T. Stover, P. Erfurt, and T. Lenarz, "Comparison of round window and cochleostomy approaches with a prototype hearing preservation electrode," *Audiol. Neurotol.*, vol. 11 Suppl 1, pp. 42–8, 2006.

[29] D. A. Gudis, M. Montes, D. C. Bigelow, and M. J. Ruckenstein, "The round window: is it the "cochleostomy" of choice? experience in 130 consecutive cochlear implants," *Otol. Neurotol.*, vol. 33, no. 9, pp. 1497–1501, 2012.

[30] S. Havenith, M. J. W. Lammers, R. A. Tange, F. Trabalzini, A. della Volpe, G. J. M. G. van der Heijden, and W. Grolman, "Hearing preservation surgery: cochleostomy or round window approach? a systematic review," *Otol. Neurotol.*, vol. 34, no. 4, pp. 667–74, Jun 2013.

[31] P. S. Roland, C. G. Wright, and B. Isaacson, "Cochlear Implant Electrode Insertion: The Round Window Revisited," *Laryngoscope*, vol. 117, no. 8, pp. 1397–1402, 2007.

[32] A. Causon, C. Verschuur, and T. A. Newman, "A retrospective analysis of the contribution of reported factors in cochlear implantation on hearing preservation outcomes.," *Otol. Neurotol.*, vol. 36, no. 7, pp. 1137–1145, Aug 2015.

[33] P. Wardrop, D. Whinney, S. J. Rebscher, J. T. Roland, Jr., W. Luxford, and P. A. Leake, "A temporal bone study of insertion trauma and intracochlear position of cochlear implant electrodes. I: comparison of Nucleus banded and Nucleus Contour electrodes," *Hear. Res.*, vol. 203, no. 1-2, pp. 54–67, 2005.

[34] M. L. Carlson, C. L.W. Driscoll, R. H. Gifford, and S. O. McMenomey, "Cochlear implantation: current and future device options," *Otolaryngol. Clin. N. America*, vol. 45, no. 1, pp. 221–248, 2012.

[35] W. Gstoettner, S. Helbig, C. Settevendemie, U. Baumann, J. Wagenblast, and C. Arnoldner, "A new electrode for residual hearing preservation in cochlear implantation: first clinical results," *Acta oto-laryngologica*, vol. 129, no. 4, pp. 372–379, 2009.

[36] C. Jolly, C. Garnham, H. Mirzadeh, E. Truy, A. Martini, J. Kiefer, and S. Braun, "Electrode features for hearing preservation and drug delivery strategies," *Adv. Otorhinolaryngol.*, vol. 67, pp. 28–42, 2010.

[37] H. Skarzynski and R. Podskarbi-Fayette, "A new cochlear implant electrode design for preservation of residual hearing: a temporal bone study," *Acta Otolaryngol.*, vol. 130, no. 4, pp. 435–42, Apr 2010.

[38] O. Adunka, J. Kiefer, M. H. Unkelbach, T. Lehnert, and W. Gstoettner, "Development and evaluation of an improved cochlear implant electrode design for electric acoustic stimulation," *Laryngoscope*, vol. 114, no. 7, pp. 1237–41, Jul 2004.

[39] T. Lenarz, T. Stover, A. Buechner, G. Paasche, R. Briggs, F. Risi, J. Pesch, and R. Battmer, "Temporal bone results and hearing preservation with a new straight electrode," *Audiol. Neurotol.*, vol. 11 Suppl 1, pp. 34–41, 2006.

[40] P. Mukherjee, H. Uzun-Coruhlu, C. C. Wong, I. S. Curthoys, A. S. Jones, and W. P. R. Gibson, "Assessment of intracochlear trauma caused by the insertion of a new straight research array," *Cochlear Implants Int.*, vol. 13, no. 3, pp. 156–62, Aug 2012.

[41] Y. Nguyen, I. Mosnier, S. Borel, E. Ambert-Dahan, D. Bouccara, A. Bozorg-Grayeli, E. Ferrary, and O. Sterkers, "Evolution of electrode array diameter for hearing preservation in cochlear implantation," *Acta oto-laryngologica*, vol. 133, no. 2, pp. 116–122, 2013.

[42] K. S. Min, S. H. Oh, M. Park, J. Jeong, and S. J. Kim, "A polymer-based multichannel cochlear electrode array," *Otol. Neurotol.*, vol. 35, no. 7, pp. 1179–86, Aug 2014.

[43] A. Radeloff, M. H. Unkelbach, M. G. Mack, C. Settevendemie, S. Helbig, J. Mueller, R. Hagen, and R. Mlynski, "A coated electrode carrier for cochlear implantation reduces insertion forces," *Laryngoscope*, vol. 119, no. 5, pp. 959–63, May 2009.

[44] J. T. Roland, Jr., "A model for cochlear implant electrode insertion and force evaluation: Results with a new electrode design and insertion technique," *Laryngoscope*, vol. 115, no. 8, pp. 1325–1339, 2005.

[45] D. Schurzig, R. J Webster, III, M. S. Dietrich, and R. F. Labadie, "Force of cochlear implant electrode insertion performed by a robotic insertion tool: Comparison of traditional versus advance off–stylet techniques," *Otol. Neurotol.*, vol. 31, no. 8, pp. 1207–1210, 2010.

[46] C. A. Todd, F. Naghdy, and M. J. Svehla, "Force application during cochlear implant insertion: An analysis for improvement of surgeon technique," *IEEE Trans. Biomed. Eng.*, vol. 54, no. 7, pp. 1247–1255, 2007.

[47] R. J. S. Briggs, M. Tykocinski, R. Lazsig, A. Aschendorff, T. Lenarz, T. Stöver, B. Fraysse, M. Marx, Jr. J. T. Roland, P. S. Roland, C. G. Wright, B. J. Gantz, J. F. Patrick, and F. Risi, "Development and evaluation of the modiolar research array–multi-centre collaborative study in human temporal bones," *Cochlear Implants Int.*, vol. 12, no. 3, pp. 129–139, 2011.

[48] T. S. Rau, A. Hussong, M. Leinung, T. Lenarz, and O. Majdani, "Automated insertion of preformed cochlear implant electrodes: evaluation of curling behaviour and insertion forces on an artificial cochlear model," *Int. J. CARS*, vol. 5, no. 2, pp. 173–81, Mar 2010.

[49] O. Majdani, D. Schurzig, A. Hussong, T. Rau, J. Wittkopf, T. Lenarz, and R. F. Labadie, "Force measurement of insertion of cochlear implant electrode arrays in vitro: comparison of surgeon to automated insertion tool," *Acta Otolaryngol.*, vol. 130, no. 1, pp. 31–36, 2010.

[50] A. Coordes, A. Ernst, G. Brademann, and I. Todt, "Round window membrane insertion with perimodiolar cochlear implant electrodes," *Otol. Neurotol.*, vol. 34, no. 6, pp. 1027–1032, 2013.

[51] A. Jeyakumar, S. F. Peña, and T. M. Brickman, "Round window insertion of precurved electrodes is traumatic," *Otol. Neurotol.*, vol. 35, no. 1, pp. 52–7, Jan 2014.

[52] M. A. Souter, R. J.S Briggs, C. G. Wright, and P. S. Roland, "Round window insertion of precurved perimodiolar electrode arrays: how successful is it?," *Otol. Neurotol.*, vol. 32, no. 1, pp. 58–63, 2011.

[53] R. Brito, T. A. Monteiro, A. F. Leal, R. K. Tsuji, M. H. Pinna, and R. F. Bento, "Surgical complications in 550 consecutive cochlear implantation," *Braz. J. Otorhinolaryngol.*, vol. 78, no. 3, pp. 80–5, Jun 2012.

[54] J. Zhang, J. T. Roland, Jr., S. Manolidis, and N. Simaan, "Optimal path planning for robotic insertion of steerable electrode arrays in cochlear implant surgery," *J. Med. Devices*, vol. 3, no. 011001, 2009.

[55] J. Pile and N. Simaan, "Characterization of friction and speed effects and methods for detection of cochlear implant electrode tip fold-over," in *IEEE Int. Conf. Robot. Autom.*, 2013.

[56] H. Mirzadeh and F. Abbasi, "Segmented detachable structure of cochlear–implant electrodes for close-hugging engagement with the modiolus," *J. Biomed. Mater. Res. B Appl. Biomater.*, vol. 68B, no. 2, pp. 191–198, 2004.

[57] R. J. S. Briggs, M. Tykocinski, E. Saunders, W. Hellier, M. Dahm, B. Pyman, and G. M. Clark, "Surgical implications of perimodiolar cochlear implant electrode design: avoiding intracochlear damage and scala vestibuli insertion," *Cochlear Implants Int.*, vol. 2, no. 2, pp. 135–149, 2001.

[58] B. Y. Arcand, P. T. Bhatti, N. V. Butala, J. Wang, C. R. Friedrich, and K. D. Wise, "Active positioning device for a perimodiolar cochlear electrode array," *Microsys.Tech.*, vol. 10, pp. 478–483, 2004.

[59] J. Wu, L. Yan, H. Xu, W. C. Tang, and F. Zeng, "A curvature-controlled 3D micro-electrode array for cochlear implants," in *IEEE Int. Conf. Solid St. Sens. Act. Microsys.*, 2005, vol. 2, pp. 1636–1639.

[60] B. Chen, H. N. Kha, and G. M. Clark, "Development of a steerable cochlear implant electrode array," in *IFMBE Int. Conf. Biomed. Eng.*, 2007, vol. 15, pp. 607–610.

[61] J. Zhang, W. Wei, J. Ding, J. T. Roland, Jr., S. Manolidis, and N. Simaan, "Inroads toward robot-assisted cochlear implant surgery using steerable electrode arrays," *Otol. Neurotol.*, vol. 31, no. 8, pp. 1199–1206, 2010.

CHAPTER 2

MAGNETIC GUIDANCE OF COCHLEAR IMPLANTS: PROOF-OF-CONCEPT AND INITIAL FEASIBILITY STUDY

The article in this chapter was originally published in the *Journal of Medical Devices*. It is reproduced here without modification and with permission of the publisher.

Prior methods to steer an electrode array through the cochlea have either fundamentally altered the shape of the electrode array or require an internal mechanism, often wire-based, to curl the electrode array during insertion. In the following article, the curling behavior is "wirelessly" obtained through magnetic manipulation. 3-to-1 scale proof-of-concept experiments demonstrate the feasibility of this approach.

My contributions to this work include integration of the digital servo controller, conducting experiments, the scaling analysis in Section 5, and manuscript editing.

Magnetic Guidance of Cochlear Implants: Proof-of-Concept and Initial Feasibility Study

James R. Clark
e-mail: james.r.clark@utah.edu

Lisandro Leon[1]
e-mail: l.leon@utah.edu

Department of Mechanical Engineering,
University of Utah,
Salt Lake City, UT 84112

Frank M. Warren
Department of Otolaryngology,
Division of Otology and Skull Base Surgery,
Oregon Health & Science University,
Portland, OR 97239
e-mail: warrenf@ohsu.edu

Jake J. Abbott
Department of Mechanical Engineering,
University of Utah,
Salt Lake City, UT 84112
e-mail: jake.abbott@utah.edu

Cochlear implants have become a standard treatment for many with severe to profound sensorineural hearing loss. However, delicate cochlear structures can be damaged during surgical insertion, which can lead to loss of residual hearing and decreased implant effectiveness. We propose a magnetic guidance concept in which a magnetically tipped cochlear implant is guided as it is inserted into the cochlea. In a scaled in vitro experimental study, we record insertion forces for nonguided and magnetically guided insertion experiments and compare the results. Results indicate that magnetic guidance reduced insertion forces by approximately 50%. Using first principles, we discuss the effects of scaling down our in vitro experiments, and account for realistic clinical dimensions. We conclude that scale–down effects are negligible, but to produce the same field strength as in our experiments and provide sufficient clearance between the patient and the manipulator, the magnet dimensions should be increased by approximately four times. [DOI: 10.1115/1.4007099]

1 Introduction

A cochlear implant (CI) is an array of electrodes embedded in silicone that is surgically inserted into the scala tympani (ST) chamber of the cochlea to electrically stimulate the nerves responsible for hearing (Fig. 1). Cochlear implants have become a standard treatment for many with severe to profound sensorineural hearing loss. However, the majority of CI users still have difficulty understanding speech in an environment with competing noise and difficulty distinguishing a full range of sounds. Future CIs will need to address three widely accepted goals [1]: (1) deeper insertion into the ST to access lower frequency cochlear neurons, (2) better proximity to the modiolus (the central axis of the cochlea) for greater operating efficiency, defined as a reduction in the stimulus charge required to produce a comfortable loudness level, and (3) reduced intracochlear damage during surgical insertion (Fig. 2) to preserve residual hearing and improve implant effectiveness.

Two major factors that contribute to the extent of damage during insertion are electrode–array design and surgical technique [2]. Numerous electrode–array designs have been developed with varied success [1–5], and to date, no single design has been able to achieve all three objectives of deeper insertion, proximity to the modiolus, and consistent atraumatic insertion [1]. Straight free–fitting CIs designed for deeper insertions can increase the risk of trauma and typically do not lie close to the modiolus [3,4]. Precurved CIs with stylets, designed to hug the modiolus, can be inserted with minimal insertion forces for nearly the entire procedure using the advance-off-stylet technique [6–8]. However, advancing the CI off the stylet too early can cause the implant tip to fold-over, and late stylet removal can result in the implant contacting the ST outer wall, potentially causing damage. The variability in human cochlear dimensions poses a challenge when using stylet withdrawal techniques, since the point during insertion when stylet removal should begin is patient dependent [1]. Further, insertions into the apical regions of the cochlea are not possible with these designs because they are significantly shorter than those designed for deep insertions.

Due to the limitations of existing CIs, several groups have developed electrode–array prototypes to achieve a modiolar-hugging position within the cochlea [9], with some actively bent or steered during insertion to minimize insertion trauma [10–13], though only Ref. [13] demonstrated insertion force reduction in their publication. Some designs [10,12,13] use mechanical means built into the CI to achieve bending, which can increase the stiffness of the CI as it is being inserted. If the CI is not formed to fit the ST well, or is misdirected down the channel, the increased CI stiffness could result in increased intracochlear trauma. Some are not reversible [9,12] or require sufficient perilymph fluid to actuate [9,11], which may be problematic if, during surgery, reinsertion is necessary [2] or sufficient fluid is lost. Finally, the wide variability in surgical force application has motivated the use of robotic assistance [14–16] and optimized path planning [13] to produce more repeatable insertions.

In this paper, we propose a magnetic guidance concept in which a magnetically tipped CI is guided as it is inserted into the cochlea. With a rotating manipulator magnet located near the patient's head, we apply magnetic torque to the implant tip, causing it to bend away from the ST walls during insertion. We conduct proof–of–concept experiments of two proposed magnetic guidance methods, using an automated experimental apparatus to

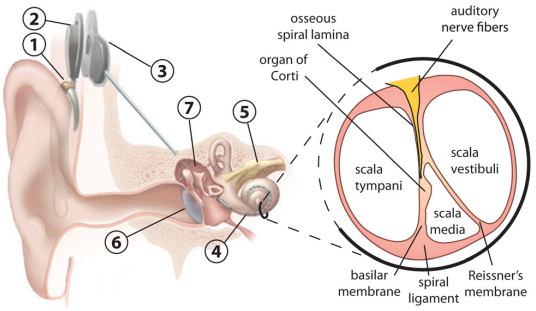

Fig. 1 Cochlear implant system with blow-up of cochlea cross-section showing the location of several cochlear structures (National Institutes of Health public domain image with added labels). Labeled items are the (1) microphone and speech processor, (2) transmitter, (3) receiver, (4) electrode array inserted into the cochlea (referred to as the "cochlear implant" herein), (5) auditory nerve, (6) ear drum, and (7) ossicles.

[1]Corresponding author.

Manuscript received July 29, 2011; final manuscript received April 3, 2012; published online August 10, 2012. Assoc. Editor: Foster B. Stulen.

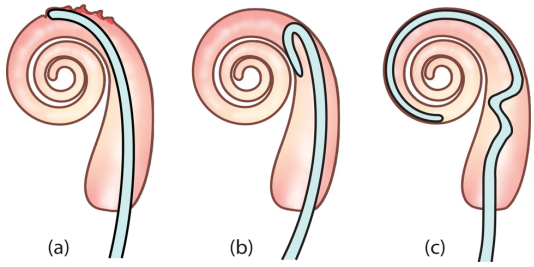

Fig. 2 Some causes of intracochlear trauma during cochlear implant insertions: (*a*) tip scraping [4], (*b*) tip fold-over [1], and (*c*) buckling [2,4]

insert a scaled magnetically tipped implant prototype into a custom 3:1 scale ST phantom [17]. We record insertion forces during nonguided and magnetically guided insertion experiments and compare the results. The data show that magnetic guidance can reduce insertion forces by approximately 50%. Our method is consistent with the current practice of using insertion force measurements (which encode implant–ST contact forces) as a metric for evaluation of insertion trauma [6–8,13–15]. Our approach is an adaptable means of guidance that could be robotically implemented as either a supervised automated process or a robotic system under surgeon manipulation. The basic idea of magnetic guidance for CIs has been proposed previously [18], but no technical results were presented to demonstrate how it could be accomplished in practice.

2 Magnetic Guidance Concept

A clinical concept for magnetically guided CI insertions is shown in Fig. 3. To achieve CI guidance, a small permanent magnet is located at the tip of the implant. A large manipulator magnet located near the patient's head is used to apply a magnetic field to the CI tip. The manipulator magnet's orientation is controlled by a motor, with the magnet's magnetization direction perpendicular to the axis of rotation. The rotation axis is approximately aligned with the central spiral axis of the cochlea. As the CI is inserted, the manipulator magnet is rotated to actively bend the implant, directing it away from cochlear walls and reducing the contact forces between the CI and the walls of the ST. The motor is allowed to translate along its rotation axis, varying the distance between the manipulator magnet and the patient, effectively changing the strength of the applied magnetic field acting on the CI tip. The CI insertion is automated and synchronized with the movement of the manipulator magnet in our developed control software.

The field $\mathbf{B}$ (T) generated by the manipulator magnet, modeled as a magnetic dipole $\mathbf{M}(\mathrm{A}\cdot\mathrm{m}^2)$, can be approximated by the point–dipole model

$$\mathbf{B}(\mathbf{p}) = \frac{\mu_0}{4\pi|\mathbf{p}|^3}\left(\frac{3(\mathbf{M}\cdot\mathbf{p})\mathbf{p}}{|\mathbf{p}|^2} - \mathbf{M}\right) \tag{1}$$

where μ_0 is the permeability of free space ($\mu_0 = 4\pi\times10^{-7}$ T·m·A^{-1}) and $\mathbf{p}$ is the location of a point in space with respect to the magnet's center (m). A magnet's dipole strength $|\mathbf{M}|$ is the product of its volume (m^3) and its average magnetization (A/m). Magnetic forces and torques will act upon any magnet placed within this nonuniform field. If we represent the permanent magnet embedded in the CI's tip by the dipole $\mathbf{m}$, then the force and torque acting on it due to the manipulator magnet are

$$\mathbf{F} = \left[\frac{\partial}{\partial x}\mathbf{B} \quad \frac{\partial}{\partial y}\mathbf{B} \quad \frac{\partial}{\partial z}\mathbf{B}\right]^{\mathrm{T}}\mathbf{m} \tag{2}$$

$$\mathbf{T} = \mathbf{m}\times\mathbf{B} \tag{3}$$

where $\mathbf{B}$ is the field at the location of $\mathbf{m}$, $\mathbf{F}$ is force (N), and $\mathbf{T}$ is the torque (N·m), expressed in the same frame in which the spatial derivatives are taken [19]. From Eq. (2) we see that the force in a given direction is the inner product of the derivative of the field in that direction and the magnetization of the magnet placed in the field. This means that a force will only act on the magnet in a given direction if both a field gradient and some component of $\mathbf{m}$ exist in that direction. The applied torque is the cross product of the magnet's dipole with the applied field, meaning that a torque will only act on the magnet if its dipole is not parallel to the applied field.

Figure 4 demonstrates how our clinical configuration allows Eqs. (1)–(3) to be simplified. Note the CI magnet is positioned approximately on the manipulator magnet's rotation axis and can be rotated about the y–axis in the xz–plane to any rotation angle θ between $\mathbf{m}$ and the local $\mathbf{B}$. The vector $\mathbf{p}$ points from the manipulator magnet to the CI magnet. Moving the manipulator toward or away from the patient along the manipulator's rotation axis will change the strength of the field applied at the CI tip, but the field direction will not change unless the manipulator magnet is rotated. Since CI tip rotations are largely confined to the xz–plane within the ST channel, the torque of Eq. (3) simplifies to

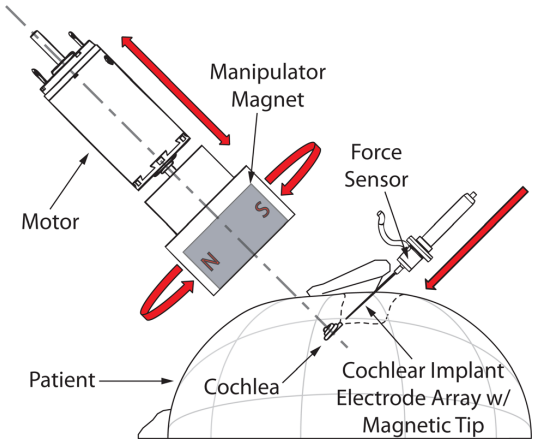

Fig. 3 Concept for magnetically guided cochlear implant surgery. Red wide arrows indicate the three controlled degrees of freedom.

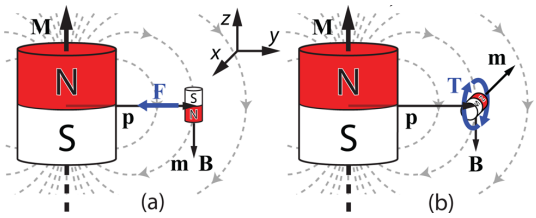

Fig. 4 Magnetic force and torque in clinical arrangement of Fig. 3. The large magnet is the manipulator magnet, with the coordinate frame origin at its dipole center (shown offset for clarity). The implant tip magnet is placed along the manipulator's rotation axis making M and p orthogonal. Two directions of the implant tip magnet with resulting forces and torques are shown. (*a*) Negative z-direction ($\theta = 0$ deg): force in negative y-direction. (*b*) Negative x-direction ($\theta = 90$ deg): negative torque about y-axis.

$$|\mathbf{T}| = |\mathbf{m}||\mathbf{B}|\sin(\theta) \tag{4}$$

Maximum torque occurs when the dipoles are perpendicular to one another; when the dipoles are aligned, the torque is zero. The general equation for the field strength in Eq. (1) and its gradient also simplify along the axis of the motor:

$$|\mathbf{B}| = \frac{\mu_0|\mathbf{M}|}{4\pi|\mathbf{p}|^3} \tag{5}$$

$$\frac{d|\mathbf{B}|}{d|\mathbf{p}|} = -\frac{3\mu_0|\mathbf{M}|}{4\pi|\mathbf{p}|^4} \tag{6}$$

Furthermore, after some manipulation, the magnetic force of Eq. (2) can be expressed in a form that more clearly shows its behavior when **m** is located along the rotation axis:

$$\mathbf{F} = \frac{d|\mathbf{B}|}{d|\mathbf{p}|}\begin{bmatrix} 0 & 0 & 0 \\ 0 & 0 & -1 \\ 0 & -1 & 0 \end{bmatrix}\mathbf{m} \tag{7}$$

We see from Eq. (7) that no gradient exists in the x-direction (first row), whereas gradients do exist in the y- and z-directions (second and third rows, respectively). Since there is no x-direction gradient, forces will not act on the magnet in the x-direction for any **m**. The second row indicates that a force will only act in the y-direction if some component of **m** points in the z-direction. This force reaches a maximum magnitude when **m** is completely aligned with the z-direction, as shown in Fig. 4(*a*). The third row indicates that a force will only act in the z-direction if some component of **m** points in the y-direction; however, since the CI tip is confined to rotate largely in the xz-plane, the components of **m** point largely in the x- and z-direction. Thus, we assume that the z-direction force is negligible. In practice, the CI tip rotation will not be strictly confined to the xz-plane, but the minor deviations we expect should only result in minor forces and torques along directions not shown in Fig. 4.

We have devised two control algorithms to synchronize the motions of the manipulator magnet and the CI insertion (Fig. 5). The first is the maximum-field method, which places the manipulator magnet as close to the patient as is physically possible for the duration of the insertion. By minimizing the separation distance between the manipulator magnet and the implant magnet ($|\mathbf{p}|$), the magnitude of the magnetic field is always at its maximum, Eq. (5). Since the CI tip is nearly aligned with the manipulator magnet for much of the insertion due to attractive forces, the implant can be directed through the ST by simply rotating the manipulator magnet. Unfortunately, these attractive forces direct the CI tip toward the delicate basilar membrane (see Fig. 1 and Fig. 4(*a*)). The primary benefit of this algorithm is reduced complexity, as it does not require the use of a controlled linear stage to vary the distance between the manipulator magnet and the patient. The second algorithm is the maximum-torque method, in which the applied field is always maintained approximately perpendicular to the CI tip, resulting in a pure magnetic torque with negligible attractive forces (see Fig. 4(*b*)). That is, at any given separation distance ($|\mathbf{p}|$), the maximum torque that can be applied to the implant occurs when the magnet dipoles are orthogonal to each other, Eq. (4). Unlike the first method, this requires variable distance between the manipulator magnet and the patient in order to control the amount of torque applied onto the CI tip throughout the insertion (since increasing torque is required for deeper insertions).

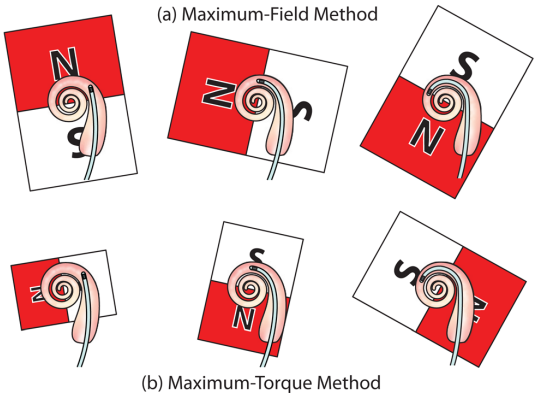

Fig. 5 Two guidance methods explored in experiments. (*a*) Maximum-field method: the dipoles are nearly aligned. (*b*) Maximum-torque method: the dipoles are nearly perpendicular. The increasing manipulator magnet size in the maximum-torque diagram indicates that the manipulator is advancing toward the cochlea.

3 Experimental Methods

To validate the basic magnetic-guidance method, we constructed an automated experimental apparatus shown in Fig. 6 consisting of a CI prototype, a force sensor, custom mounting fixtures, an ST phantom, linear stages, a manipulator magnet, a servo system (not labeled), and a standard personal computer (not shown).

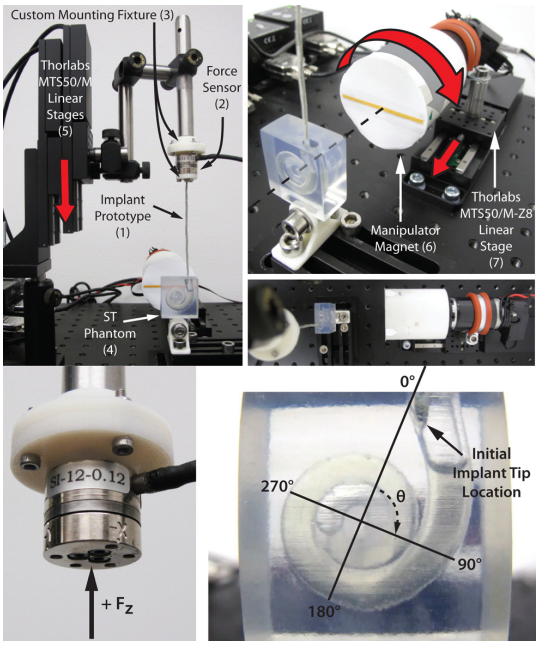

Fig. 6 Experimental setup. (top) The prototype (1) was attached to a force/torque sensor (2) with custom mounting fixtures (3) and inserted into a phantom (4) using linear stages (5). The manipulator (6) is attached to a brushed dc motor shaft and mounted to a linear stage (7), which translates the manipulator toward the phantom. The dashed line shows that the manipulator rotation axis and cochlear central spiral axis are aligned. The curved arrow above the manipulator (6) shows the manipulator rotation direction. The straight arrows on (5) and (7) show the translation direction of the linear stages. The stripe on the front of the manipulator marks the dipole direction of the enclosed axially magnetized magnet. (bottom-left) ATI Nano17 force/torque sensor with definition of positive force. (bottom-right) Insertion angle based on the phantom model [17].

Fig. 7 (top) The MED-EL practice electrode shown is a straight, free-fitting electrode array with a length of 32 mm, and it tapers from a base diameter of 1.3 mm to a tip diameter of 0.5 mm. (bottom) Our 3:1 prototype has a length of 83 mm and a constant diameter of 1.6 mm.

We constructed a prototype CI with a small (1 mm diameter × 2 mm long) permanent magnet (of approximate dipole strength 2 mA·m^2) embedded in its tip; the prototype is a 3:1 scale model of a free-fitting straight CI. Our goal was not to duplicate a scaled version of a commercial CI but to develop one that could be used to validate our magnetic guidance concept. We also wanted the prototype to qualitatively mimic some important properties of a real CI (such as the MED-EL practice electrode in Fig. 7), including graded stiffness, bending properties, and the use of silicone rubber. The process to fabricate the prototypes is shown in Fig. 8.

We inserted the implant into a custom 3:1 scale scala-tympani phantom filled with soap solution; the phantom's model, described in detail in Ref. [17], is based on published anatomical data and can be manufactured to a desired scale.

An ATI Nano17 six–axis force/torque sensor was used to collect force data during insertion experiments. Along the sensor z-axis, the minimum resolution is 3.125 mN and the maximum measurement uncertainty is 170 mN, which is the maximum amount of error in any single measurement. However, under certain loading conditions, the sensor performs significantly better. In the accompanying calibration report, measurement uncertainty of 1.7–3.4 mN was reported for sensor loading along its z-axis exclusively, which is the loading condition of our experimental setup.

Custom mounting fixtures, printed in ABS*plus* thermoplastic using a Dimension 3D printer, were used to attach the force sensor to the Thorlabs mounting posts and the implant prototype to the front (tool side) of the sensor.

The manipulator consists of a Delrin housing attached to a motor shaft with a 25.4–mm–diameter × 25.4–mm–long NdFeB permanent magnet placed in the housing. The cylindrical magnet is axially magnetized with a measured dipole strength of 10.2 A·m^2.

The rotation of the manipulator magnet was controlled using commercial servo components, including a digital servo drive (Advanced Motion Controls DigiFlex Performance DPR Series), dc power supply (GW Instek GPS-3303), and a brushed dc motor and encoder unit (Maxon A-max 32 and HEDS 5540). The motion of the CI was captured through the transparent phantom using a commercial camera (Canon PowerShot G10). System control and data logging were performed with a personal computer running Windows.

The experiments were conducted on a Thorlabs metric optical table with the following arrangement. The implant prototype was mounted to the vertically stacked stages oriented so that the prototype pointed downward. The 3:1 ST phantom was attached vertically to the table so that the entrance of the chamber was facing upward, with the ST chamber spiraling toward the manipulator magnet. Adjustments were made so that the manipulator rotation axis was approximately aligned with the central spiral axis of the cochlea.

The sensor itself experiences forces and torques from the manipulator magnet since the sensor is made of ferromagnetic material. Thus, to calibrate for these effects, insertion measurements were taken while running experiments without the CI prototype attached to the sensor. Five calibration runs were averaged and subtracted from the insertion measurements recorded with the prototype attached.

We conducted nonguided and magnetically guided experiments on the same CI, with all other factors held constant. During the experiments, the closest distance between the manipulator magnet and the CI tip corresponded to a dipole-to-dipole distance of 29 mm. The ideal trajectory for the prototype is one in which its tip avoids the most contact with the ST walls during the experiment. Toward this end, the position of the manipulator magnet (both rotation and translation toward the phantom) at each 1 mm discrete translation of the prototype was experimentally predetermined through visual inspection of the CI tip in relation to the ST walls (i.e., to maintain the tip parallel to the channel). With the maximum-field strategy, only the rotation of the manipulator magnet was predetermined. With the maximum-torque method, however, both parameters were predetermined with the additional constraint that the magnet dipoles were kept orthogonal to each other throughout the insertion. The predetermined manipulator trajectory was preprogrammed and automated with respect to the translation of the prototype. At each discrete 1 mm interval along this trajectory, 10 ms of force data were collected and averaged, until a total translation of 74 mm was achieved.

4 Experimental Results

The measured insertion forces are shown in Fig. 9. The variance between runs was calculated and presented as solid vertical lines indicating the two-standard deviation interval at each depth. Insertion depths are measured from the initial implant position shown in Fig. 6. The vertical dashed lines show the approximate insertion depths where the implant first made contact with the phantom outer wall. Their corresponding images are shown in Fig. 9(*d*). For the nonguided insertions, initial outer-wall contact (which can be reasonably described as a direct impingement of the tip onto the wall) occurred at 17.5 mm. Using magnetic guidance, our prototype avoids contact with the first cochlear turn and clearly allows the CI to be inserted deeper into the ST phantom before it makes initial contact. Additionally, guided insertions produce a more distributed initial contact than nonguided insertions. For an

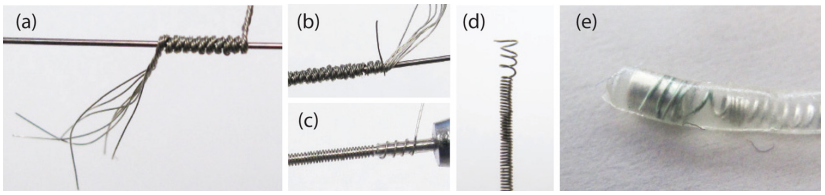

Fig. 8 Key steps for production of the wire core used in the implant prototype. (*a*) Wires twisted together and wrapped around a cylindrical shaft. (*b*) Snip off one wire at a certain length and wrap the remaining wires. Repeat this process until only one wire is left. This creates a tapered stiffness, which was observed in the MED-EL device. (*c*) Wrap remaining wire around tubing to create a coil that the magnet can be slid into. (*d*) The result of the wire wrapping prior to placing the magnet. (*e*) Magnet is placed at the end of the coil and encased in silicone using an acrylic mold.

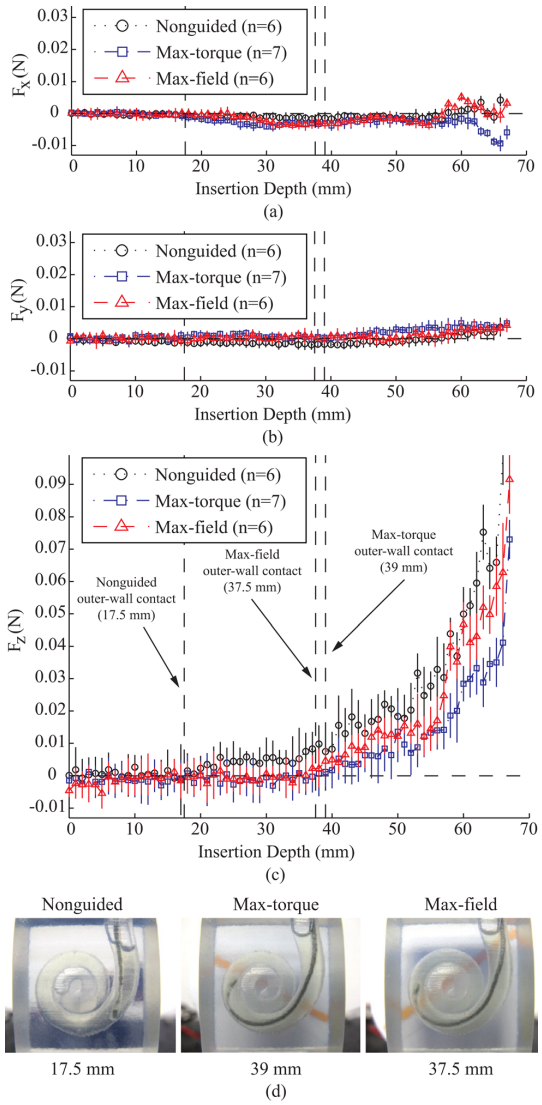

Fig. 9 (*a–c*) Force measurements for all three insertion methods. The direction of F_x, F_y, and F_z are defined in Fig. 4 and Fig. 6. Each data point represents the average of *n* runs, where the collected measurement for each run is an average of 10 samples at the corresponding insertion depth. The solid vertical bar with each data point shows the two-standard-deviation interval. Vertical dashed lines mark the approximate locations where the implant first made contact with the ST outer wall. (*d*) Corresponding images showing implant positions at first instance of outer-wall contact.

insertion depth between 0 mm and 25 mm, no method shows a clear advantage. However, the magnitudes of the forces in this region are so small that they are of limited interest. After 25 mm, the nonguided approach is inferior to both magnetically guided strategies. As long as the prototype avoids contact with the ST, insertions forces are negligible, and although the guided implant eventually slides against the ST outer wall, the CI touches the wall softer when using guidance, and the tip is bent away from the wall, decreasing both frictional and tip contact forces (Fig. 10). In general, nonguided insertions resulted in the highest force and the

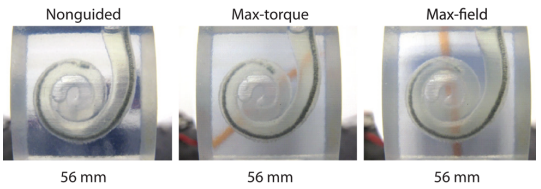

Fig. 10 The tip of the implant is directed away from the outer wall using both the maximum-torque and maximum-field methods, even at significant insertion depths

maximum-torque method generally resulted in the lowest force. This is consistent with our hypothesized outcome described in Sec. 2: the maximum-torque method minimizes attractive forces between the CI and the manipulator magnet, which in turn minimizes lateral scraping on the ST wall. Nevertheless, any lateral scraping caused by attractive forces in the maximum-field method does not negate the benefits of guiding the CI tip through the channel. This is reasonable given that an estimate of the maximum attractive force of only 10 mN was computed using Eq. (7) at the closest dipole-to-dipole distance of 29 mm with the maximum-field method. These results show that insertion forces can be reduced by approximately 50% using magnetic guidance, indicating that significant insertion-force reduction is possible with our approach.

5 Discussion

Without guidance, the inherent stiffness in a free-fitting CI produces a mechanical restoring torque that presses the CI against the outer ST wall, resulting in increased friction and insertion force. With magnetic guidance, the torque acting on the CI tip counteracts this mechanical restoring torque. If the magnetic torque is sufficient, the CI will be directed completely away from the wall. If not, the magnetic torque will still provide some decrease in contact forces, as demonstrated by the reductions shown in Fig. 9. While the required applied torque is a function of the prototype's bending stiffness and its distribution, our main goal was not to determine the required torques needed to insert clinical CIs. Rather, this proof-of-concept study endeavored to demonstrate the viability of insertion-force reduction with the magnetic guidance strategies proposed. To this end, a rigorous method to measure the prototype's bending stiffness seemed unnecessary when a prototype that qualitatively matched the stiffness of a commercial CI was sufficient.

Our straight, free-fitting prototype limits the benefit of magnetic guidance since eventually the applied magnetic torque cannot overcome the natural tendency of the prototype to maintain its relaxed, straight shape. If the CI were fabricated so that its relaxed shape approximated the ST curvature (as is done with some current clinical CIs) then we could use our magnetic guidance concept to uncoil these precurled CIs during insertion and conceivably achieve near-zero insertion force throughout the insertion. An ideal prototype would exhibit the desired bending properties such that a magnetic torque applied at the tip results in the most desirable uncoiled shape for insertion. This type of design would also address the aforementioned, second widely accepted goal [1] in that close proximity between the CI and the modiolus reduces the power consumption required by the electrodes and the cross–talk responsible for poor frequency resolution due to one electrode stimulating multiple locations on the nerve.

A second way in which our prototype limits the benefit of magnetic guidance is that insertions into our ST phantom beyond 560 deg are precluded because our prototype's tip diameter (1.6 mm) exceeds the local channel height (1.41 mm). Unlike our prototype, which has a constant diameter throughout, real CIs have a tapered shape; that is, they are thicker at the base and thinner at the tip. Tapering future prototypes to have a smaller diameter

(and a smaller embedded magnet) would allow deeper insertion into the ST, and the tapered shape would help provide the necessary basal stiffness to avoid buckling.

To achieve better proximity to the modiolus, a class of precurved CIs have been developed that are initially straightened with an internal stylet (i.e., a stiff metal wire) but return to their original spiral shape after its removal. One of the more promising CIs in this class uses an insertion technique, known as advance-off-stylet (AOS), in which the electrodes are pushed off the stylet at the beginning of the first cochlear turn [1]. As reported by several groups [6–8], the AOS technique shows a notable decrease in forces for nearly the entire insertion procedure in part because this technique can eliminate contact between the CI and the outer wall of the first cochlear turn [1]. This is advantageous since most insertion trauma occurs at or near the first site of contact with the lateral wall of the ST (i.e., the first cochlear turn), and any additional trauma past this point seems minimal, mainly since low incidence angles between the CI and the lateral wall are no longer likely [20]. However, the CIs designed for this insertion technique are approximately 22 mm in length, which is very short compared to the longest free-fitting arrays currently available. As a result, deep insertions into the apical regions of the cochlea are not possible. Using magnetic guidance, our prototype similarly avoids contact with the first cochlear turn (Fig. 11), yet this concept can be applied to longer CIs to achieve deeper insertions. Additionally, our concept can be easily adapted to improve the advance-off-stylet insertion technique by straightening the CI during the critical moments when withdrawing the stylet can result in the CI curving into the ST inner wall (see Fig. 2(*b*)).

In the experiments herein, we used force sensing only for analysis after the insertion had been performed. Others have used force feedback to regulate insertion speed during their experiments using a steerable prototype electrode array [13]. It seems reasonable to utilize force measurements and control algorithms in real-time to minimize insertion forces adaptively throughout the insertion, essentially allowing the CI to "feel around in the dark," as opposed to relying on medical imaging for guidance. This capability would be advantageous since preoperative imaging to determine the dimensions of the patient's cochlea is not a current practice for CI surgery [1]. By including measured mechanical properties of the basilar membrane into a force control strategy, a surgeon can detect if the CI is about to rupture into adjacent cochlear chambers. Unexpected increases in force will be detected before they become problematic. Corrective action can be taken by adapting the guidance continuously or by reversing the insertion for a small distance and then modifying the magnetic guidance plan.

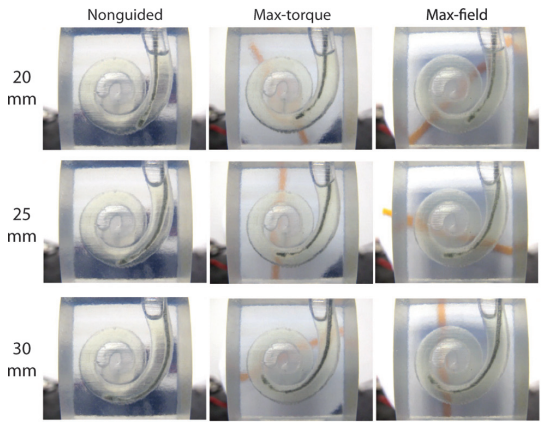

Fig. 11 Images of implant through the first turn

Implementing force feedback control is complicated by the fact that the force sensor is not colocated with the implant tip. Interpreting tip forces, especially since the implant is flexible, may be difficult. That is, forces on the tip (including ST contact forces and attractive magnetic forces) may not be easily measured with a force sensor located at the base. In the experiments of Fig. 9, the measured forces in the direction of the basilar membrane (y-direction of Fig. 4) did not exceed 2 mN even though the attractive magnetic force (as discussed earlier) is as high as 10 mN using the maximum-field strategy. That said, neither the estimated attractive force (10 mN) nor the measured force in the direction of the basilar membrane (2 mN distributed along the entire implant length) exceeded the force required to puncture the basilar membrane (26–35 mN as measured by one group [21]). Further, in our implementation, the dominant magnetic torque is used to align the implant tip in the direction of the ST channel, which is parallel to the ST walls (Fig. 10). Thus, the typical scenario of basilar perforation in which the electrode tip impinges on the basilar membrane is avoided. Clearly, the attractive forces on the implant did not increase the overall friction because the insertion force ($\mathbf{F}_z$) decreased with the use of magnetic guidance. This seems reasonable given that the friction due to lateral scraping from the attractive forces is partially muted by the soap solution. More importantly, the actual friction in a real insertion may only be about 1–2 mN (for the estimated 10 mN of attractive forces) based on measured friction coefficients (0.10–0.20) between clinical CIs and the endosteum lining of the ST [22]. Some attractive force may even be beneficial to direct the implant towards the apex of the cochlea (Fig. 3). This topic requires further investigation.

Our magnetic guidance approach can be scaled according to clinical demands. The magnetic field strength of any source is homothetic, meaning that the field of a permanent magnet is unchanged as the dimensions are scaled. The field gradient, however, is not homothetic. The field of a small magnet changes faster spatially than that of a large magnet. This can be demonstrated through some manipulation of Eqs. (5) and (6). If we scale the magnet's linear dimensions by a factor s then its volume scales as s^3. Therefore, assuming identical magnetization, the dipole strength $\mathbf{M}$ and the resulting field strength and gradient will also scale as s^3. Now suppose that we measure the field at a distance $s|\mathbf{p}|$ from the scaled magnet so that the distance has been scaled by the same factor as the magnet's linear dimensions. Equations (5) and (6) become

$$|\mathbf{B}| = \frac{\mu_0(s^3|\mathbf{M}|)}{4\pi(s^3|\mathbf{p}|^3)} = \frac{\mu_0|\mathbf{M}|}{4\pi|\mathbf{p}|^3} \tag{8}$$

and

$$\frac{d|\mathbf{B}|}{d|\mathbf{p}|} = -\frac{3\mu_0(s^3|\mathbf{M}|)}{4\pi(s^4|\mathbf{p}|^4)} = -\frac{3\mu_0|\mathbf{M}|}{4\pi|\mathbf{p}|^4}\left(\frac{1}{s}\right) \tag{9}$$

The field strength of a permanent magnet scaled by a factor s measured a scaled distance $s|\mathbf{p}|$ away from the its center is the same as the field strength measured a distance $|\mathbf{p}|$ away from the original magnet. This is the homothetic property of the field. The field gradient, however, is $1/s$ times that of the originally measured gradient.

Our experimental setup and results used a scaled 3:1 implant prototype and ST phantom. The effects of scaling down to 1:1 can be initially assessed by modeling the implant as a cantilever beam with a pure torque at its tip, resulting in the following expression for the deflected angle at the tip [23]

$$\theta = \frac{TL}{EI} \tag{10}$$

where T is the torque applied at the implant tip, L and E are the length and Young's modulus of the implant, respectively, and I is the moment of inertia of the cross-sectional area, which, if approximated as a circle of diameter d, is

$$I = \frac{\pi d^4}{64} \tag{11}$$

By substituting Eq. (11) into Eq. (10), the tip deflection angle can be expressed as

$$\theta = \frac{64TL}{\pi E d^4} \tag{12}$$

Scaling down the implant by a factor s will reduce the implant's length and diameter by the same factor s. To accommodate the smaller geometric constraints of the scaled-down implant, a smaller implant magnet will be required. If this is represented as a reduction in its linear dimension by the same factor s, then the volumetric reduction (s^3) of the implant magnet reduces the applied torque at the tip by s^3. The result of scaling down the implant is no effect on the tip deflection angle, as seen in Eq. (13):

$$\theta = \frac{64(T/s^3)(L/s)}{\pi E (d/s)^4} = \frac{64TL}{\pi E d^4} \tag{13}$$

Scaling of the phantom does not affect the tip deflection angles required to navigate through it. Therefore, scaling our experiments down to 1:1 (i.e., reducing the implant, its magnet, and the phantom) likely will not have major effects on the results.

Having demonstrated scaling effects of the magnetic field and the implant, we can now discuss the approximate scale of a clinical arrangement. As indicated earlier, the nearest dipole-to-dipole distance in these experiments is about 30 mm. Increasing the dipole-to-dipole distance to 120 mm will require a 102–mm–diameter × 102–mm–long manipulator magnet to produce the same field strength as in our experiments. Since the distance from the apex of the cochlea to the edge of the head along the axis of the cochlea is approximately 60 mm, a 10 mm clearance between the edge of the head and the edge of the manipulator magnet can be achieved in a clinical setting with a 102–mm–diameter × 102–mm–long manipulator magnet. It should be noted that the manipulator magnet size can be reduced by increasing the grade of NdFeB magnet used, and the strength of the required field can be reduced by modifying certain implant design factors such as increased implant flexibility.

The effect of strong magnetic fields on implanted medical devices has been a longstanding concern ever since magnetic resonance (MR) scanners became a common diagnostic tool for clinicians. Numerous studies have scrutinized cochlear implants in the strong magnetic fields (1.5 T) of an MR scanner [24–26]. It is now generally accepted that heating and electrical stimulation in the electrodes of a cochlear implant electrode array due to eddy currents induced by changing magnetic fields in an MR scanner are largely negligible and well within healthy thresholds [26]. It also seems reasonable to expect that the electrode array does not shift during an MR scan since concerns over potential device displacement is typically associated with the internal receiver magnet [26] (see Fig. 1). Since the magnetic field in an MR scanner is significantly stronger than any field produced in our concept, it seems reasonable then to expect that any effect from the magnetic field (either from the manipulator or the implant magnet) on the actual electrodes in the cochlear implant electrode array is negligible.

Progress toward clinical feasibility will require several issues to be addressed. The obvious concerns regarding MR scanner safety can be addressed by a CI prototype design with a removable magnetic tip. Alignment of the manipulator rotation axis with the central axis of the cochlea may be difficult in practice and warrants some study on the effects of misalignment. Further, the implant magnet is never truly situated on the manipulator's axis of rotation (as shown in Fig. 4) since the implant magnet is always off-axis while tracing out the cochlear spiral. These off-axis effects warrant further study. In the conventional otologic position (Fig. 3), the initial insertion angle is not oriented as shown in our experiments. Improved *in vitro* studies should orient the phantom to mimic the initial insertion angle and account for initial gravity effects on a flexible implant. Our experimental setup and results used a scaled 3:1 implant prototype and ST phantom. Eventually, these experiments must be performed at 1:1 scale, requiring a 1:1 scale implant and a 1:1 scale ST phantom with both cochleostomy and round-window openings and oriented to mimic the conventional otologic position. Deviations into other scalar chambers could not be assessed with our experiment since trajectories were preplanned through a phantom consisting of only the ST path. *In vitro* studies with ST phantoms and cadaver temporal bones directly comparing our prototype and insertion method against commercial CIs using standard techniques are required for proper evaluation.

6 Conclusion

We have presented a proof-of-concept study that demonstrates the efficacy of implementing magnetic guidance as a clinical strategy toward improved cochlear implant surgery. By applying magnetic torque to the tip of a cochlear-implant prototype during insertions, we reduced the insertions forces by approximately 50%. Such reductions will likely reduce insertion trauma by a proportional amount and may enable deeper insertion into the cochlea for improved performance.

Acknowledgment

This work was supported by the National Science Foundation under Grants IIS-0952718 and DGE-0654414. This work appeared in part at the 2011 IEEE/RSJ International Conference on Intelligent Robots and Systems. This research is part of a larger collaboration with Dr. Robert Webster at Vanderbilt University, and the authors would like to thank him for fruitful discussions.

References

[1] Rebscher, S. J., Hetherington, A., Bonham, B., Wardrop, P., Whinney, D., and Leake, P. A., 2008, "Considerations for Design of Future Cochlear Implant Electrode Arrays: Electrode Array Stiffness, Size, and Depth of Insertion," J. Rehabil. Res. Dev., **45**(5), pp. 731–747.
[2] Briggs, R. J. S., Tykocinski, M., Saunders, E., Hellier, W., Dahm, M., Pyman, B., and Clark, G. M., 2001, "Surgical Implications of Perimodiolar Cochlear Implant Electrode Design: Avoiding Intracochlear Damage and Scala Vestibuli Insertion," Cochlear Implants Int., **2**(2), pp. 135–149.
[3] Adunka, O., and Kiefer, J., 2006, "Impact of Electrode Insertion Depth on Intracochlear Trauma," Otolaryngol. Head Neck Surg., **135**(3), pp. 374–382.
[4] Gstoettner, W., Franz, P., Hamzavi, J., Plenk, H., Baumgartner, W., and Czerny, C., 1999, "Intracochlear Position of Cochlear Implant Electrodes," Acta Otolaryngol., **119**(2), pp. 229–233.
[5] Gstoettner, W. K., Adunka, O., Franz, P., Hamzavi, J., Plenk, H., Susani, M., Baumgartner, W., and Kiefer, J., 2001, "Perimodiolar Electrodes in Cochlear Implant Surgery," Acta Otolaryngol., **121**(2), pp. 216–219.
[6] Roland, Jr., J. T., 2005, "A Model for Cochlear Implant Electrode Insertion and Force Evaluation: Results With a New Electrode Design and Insertion Technique," Laryngoscope, **115**(8), pp. 1325–1339.
[7] Todd, C. A., Naghdy, F., and Svehla, M. J., 2007, "Force Application During Cochlear Implant Insertion: An Analysis for Improvement of Surgeon Technique," IEEE Trans. Biomed. Eng., **54**(7), pp. 1247–1255.
[8] Schurzig, D., Webster III, R. J., Dietrich, M. S., and Labadie, R. F., 2010, "Force of Cochlear Implant Electrode Insertion Performed by a Robotic Insertion Tool: Comparison of Traditional Versus Advance Off-Stylet Techniques," Otol. Neurotol., **31**(8), pp. 1207–1210.
[9] Mirzadeh, H., and Abbasi, F., 2004, "Segmented Detachable Structure of Cochlear-Implant Electrodes for Close-Hugging Engagement With the Modiolus," J. Biomed. Mater. Res. B Appl. Biomater., **68B**(2), pp. 191–198.
[10] Arcand, B. Y., Bhatti, P. T., Butala, N. V., Wang, J., Friedrich, C. R., and Wise, K. D., 2004, "Active Positioning Device for a Perimodiolar Cochlear Electrode Array," Microsys.Tech., **10**(6), pp. 478–483.
[11] Wu, J., Yan, L., Xu, H., Tang, W. C., and Zeng, F.-G., 2005, "A Curvature-Controlled 3D Micro-Electrode Array for Cochlear Implants," IEEE 13th International Conference on Solid-State Sensors, Actuators and Microsystems, TRANSDUCERS '05, Vol. 2, Seoul, Korea, June 5–9, pp. 1636–1639.
[12] Chen, B., Kha, H. N., and Clark, G. M., 2007, "Development of a Steerable Cochlear Implant Electrode Array," 3rd Kuala Lumpur International Conference on Biomedical Engineering 2006 (IFMBE Proceedings), Vol. 15 pp. 607–610.

[13] Zhang, J., Roland, Jr., J. T., Manolidis, S., and Simaan, N., 2009, "Optimal Path Planning for Robotic Insertion of Steerable Electrode Arrays in Cochlear Implant Surgery," ASME J. Med. Devices, **3**(1), p. 011001.
[14] Zhang, J., Wei, W., Ding, J., Roland, Jr., J. T., Manolidis, S., and Simaan, N., 2010, "Inroads Toward Robot-Assisted Cochlear Implant Surgery Using Steerable Electrode Arrays," Otol. Neurotol., **31**(8), pp. 1199–1206.
[15] Majdani, O., Schurzig, D., Hussong, A., Rau, T., Wittkopf, J., Lenarz, T., and Labadie, R. F., 2010, "Force Measurement of Insertion of Cochlear Implant Electrode Arrays in Vitro: Comparison of Surgeon to Automated Insertion Tool," Acta Otolaryngol., **130**(1), pp. 31–36.
[16] Schurzig, D., Labadie, R. F., Hussong, A., Rau, T. S., and Webster III, R. J., 2012, "Design of a Tool Integrating Force Sensing With Automated Insertion in Cochlear Implantation," IEEE/ASME Trans. Mechatronics, **17**(2), pp. 381–389.
[17] Clark, J. R., Warren, F. M., and Abbott, J. J., 2011, "A Scalable Model for Human Scala-Tympani Phantoms," ASME J. Med. Devices, **5**(1), p. 014501.
[18] Maghribi, M. N., Krulevitch, P. A., Davidson, J. C., and Hamilton, J. K., 2006, "Implantable Devices Using Magnetic Guidance," U.S. Patent No. 0052656.
[19] Abbott, J. J., Ergeneman, O., Kummer, M. P., Hirt, A. M., and Nelson, B. J., 2007, "Modeling Magnetic Torque and Force for Controlled Manipulation of Soft–Magnetic Bodies," IEEE Trans. Robot., **23**(6), pp. 1247–1252.
[20] Zeng, F.-G., Rebscher, S., Harrison, W., Sun, X., and Feng, H., 2008, "Cochlear Implants: System Design, Integration, and Evaluation," IEEE Rev. Biomed. Eng., **1**, pp. 115–142.
[21] Ishii, T., Takayama, M., and Takahashi, Y., 1995, "Mechanical Properties of Human Round Window, Basilar and Reissner's Membranes," Acta Otolaryngol., **115**(s519), pp. 78–82.
[22] Kha, H. N., and Chen, B. K., 2006, "Determination of Frictional Conditions Between Electrode Array and Endosteum Lining for Use in Cochlear Implant Models," J. Biomech., **39**(9), pp. 1752–1756.
[23] Howell, L. L., 2001, *Compliant Mechanisms*, John Wiley & Sons, Inc., New York.
[24] Teissl, C., Kremser, C., Hochmair, E. S., and Hochmair-Desoyer, I. J., 1999, "Magnetic Resonance Imaging and Cochlear Implants: Compatibility and Safety Aspects," J. Magn. Reson. Imaging, **9**(1), pp. 26–38.
[25] Gubbels, S. P., and McMenomey, S. O., 2006, "Safety Study of the Cochlear Nucleus 24 Device With Internal Magnet in the 1.5 Tesla Magnetic Resonance Imaging Scanner," Laryngoscope, **116**(6), pp. 865–871.
[26] Crane, B. T., Gottschalk, B., Kraut, M., Aygun, N., and Niparko, J. K., 2010, "Magnetic Resonance Imaging at 1.5 T After Cochlear Implantation," Otol. Neurotol., **31**(8), pp. 1215–1220.

CHAPTER 3

SCALA-TYMPANI PHANTOM WITH COCHLEOSTOMY AND ROUND-WINDOW OPENINGS FOR COCHLEAR-IMPLANT INSERTION EXPERIMENTS

The article in this chapter was originally published in the *Journal of Medical Devices*. It is reproduced here without modification and with permission of the publisher.

The article summarizes the design of a scala-tympani phantom that can be used to accurately simulate electrode-array insertions at clinical scale. In particular, it is the first phantom to model a round-window opening and can be used reliably to simulate insertion forces in cadaver cochleae.

Lisandro Leon[1]
Department of Mechanical Engineering,
University of Utah,
Salt Lake City, UT 84112
e-mail: l.leon@utah.edu

Matt S. Cavilla
Department of Mechanical Engineering,
University of Utah,
Salt Lake City, UT 84112
e-mail: matt.cavilla@utah.edu

Michael B. Doran
Department of Mechanical Engineering,
University of Utah,
Salt Lake City, UT 84112
e-mail: mike.doran@utah.edu

Frank M. Warren
Department of Otolaryngology,
Division of Otology and Skull Base Surgery,
Oregon Health & Science University,
Portland, OR 97239
e-mail: warrenf@ohsu.edu

Jake J. Abbott
Department of Mechanical Engineering,
University of Utah,
Salt Lake City, UT 84112
e-mail: jake.abbott@utah.edu

Scala-Tympani Phantom With Cochleostomy and Round-Window Openings for Cochlear-Implant Insertion Experiments

Experiments with scala-tympani (ST) phantoms are used to evaluate new electrode arrays and cochlear-implant insertion techniques. To date, phantoms have not accounted for clinical orientations and geometric differences between round-window (RW) insertions and anteroinferior cochleostomy insertions. For improved assessments of insertion experiments, we present a scala-tympani phantom that offers three distinct benefits over previous phantoms: it mimics the standard otologic position, it accommodates for both round-window and anteroinferior cochleostomy insertions, and it incorporates a visual coordinate system based on industry consensus making standardized angular measurements possible. [DOI: 10.1115/1.4027617]

1 Introduction

A cochlear implant (CI) is an array of electrodes that is surgically inserted into the ST chamber of the cochlea to partially restore hearing. Ongoing interest in atraumatic CI insertions has prompted numerous electrode-array designs and insertion techniques. A common method for evaluating the effectiveness of these novel designs and strategies is through insertion force experiments in an ST phantom, especially in the early stages of development, where the added cost and complexity of using temporal bones or in vivo experiments are not yet warranted.

Although many phantoms with varying levels of fidelity have been used [1–8], to date, there has not been one designed specifically to model the realistic surgical constraints present in clinical practice imposed upon CI insertions. Typical phantom openings do not model the geometries of the RW or an anteroinferior cochleostomy, which are the openings used in actual insertions. Orienting typical phantoms so that insertion experiments duplicate clinically realistic angles (Fig. 1) require data on the cochlea's orientation which, until now, has not been synthesized into one convenient source. Although Advanced Bionics (Valencia, CA) provides a base that will orient their cochlea phantom appropriately, they make no claims regarding its accuracy. Current phantoms have also not addressed recent industry consensus for a standardized coordinate system in response to the challenges of interpreting results from various investigators [9]. We address these concerns with an ST phantom designed for improved cochlear-implant insertion experiments.

2 Standard Otologic Position

CI surgery is performed in the conventional otologic position, with the patient's back flat on the operating table, and the head turned toward the side by approximately 65 deg. This orients the skull such that the angle between the operating table and the skull's midsagittal plane is approximately 25 deg (Fig. 1). If necessary, the table is further adjusted to provide an optimal view into the cochlea to perform the surgery.

The primary difficulty in orienting a phantom to mimic this standard position is that the orientation of the cochlea within the skull or with respect to specific landmarks on the body is not readily available. One group [10–12] interested in using standard radiographic techniques to determine the postoperative position of a CI's electrode bands inside the cochlea determined the required skull orientation relative to a central X-ray beam (Fig. 2) necessary to produce an optimized 2D radiograph of the cochlea (Fig. 3) in which the plane of the basal cochlear turn (and the electrode array) is essentially parallel to the film plane. This method, known as the cochlear view (CV), requires the X-ray beam to be parallel to the modiolar axis (the central spiral axis of the cochlea) and orthogonal to the basal turn. This has become the standard 2D radiologic view of the cochlea [13], with some regarding it as the optimal 2D view of the cochlea [9]. Their work effectively defined the spatial orientation of the cochlea inside the skull, which we adopt to orient the ST phantom with respect to a tabletop.

The three angles with respect to anatomic landmarks required to orient the cochlea are shown in Figs. 2 and 3 and summarized in Table 1. The first two angles (θ_1 and θ_2) orient the cochlear axis relative to the skull's midsagittal plane and infraorbitomeatal plane, respectively. The third angle (θ_3) locates the RW in the plane through the basal turn. Unlike the first two angles, which are given relative to anatomic landmarks, the third angle can be difficult to visualize since it is given with respect to an abstract reference (0 deg reference in Fig. 3).

To understand this abstract reference with respect to an anatomical landmark, we examine Fig. 4, which shows a detailed version of Fig. 2(*a*). The modiolar axis, the plane of the superior-semicircular canal (SSC), and the X-ray are nearly parallel, making the film plane nearly orthogonal to all three. Since the X-ray is

[1]Corresponding author.

Manuscript received January 7, 2014; final manuscript received May 1, 2014; published online August 19, 2014. Assoc. Editor: Rafael V. Davalos.

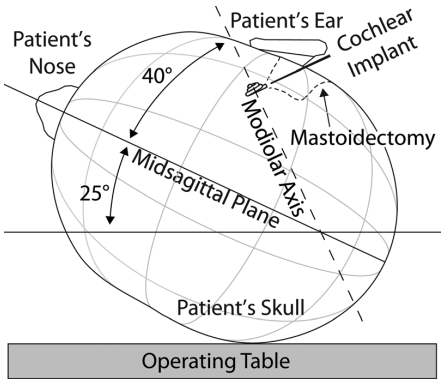

Fig. 1 Diagram of the standard otologic positioning

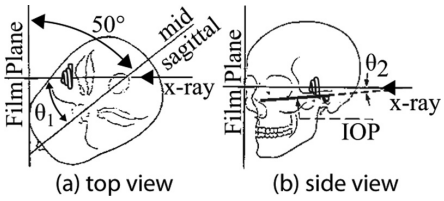

Fig. 2 The method to generate the cochlear view of Fig. 3 is summarized. (*a*) While the X-ray and film plane are maintained orthogonal to each other, the skull is positioned against the film such that the angle between it and the midsagittal plane is approximately 50 deg. (*b*) Next, the skull is adjusted so that the angle between the X-ray and the infraorbitomeatal plane (IOP) is near zero. Upon completion, the modiolar axis is nearly parallel to the X-ray. Modified image from Ref. [10] reproduced with permission of Wolters Kluwer Health.

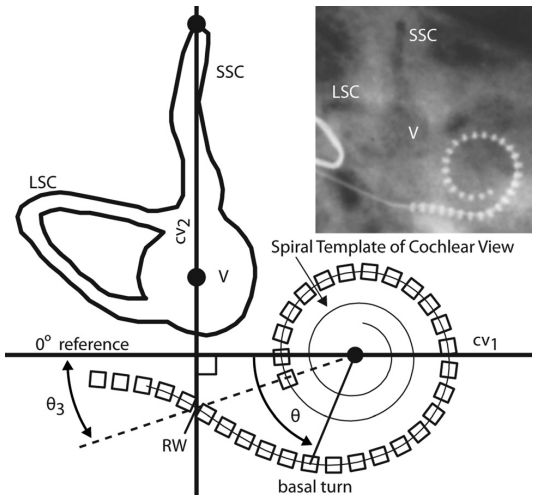

Fig. 3 The skull positioning of Fig. 2 results in the cochlear view, which contains a 2D image of the electrode array (shown as a series of squares) as a nonoverlapping spiral in the basal and middle turns. The spiral center is determined by fitting a mathematical spiral template to the position of the electrodes. The line cv_2 passes through the top of SSC and the midpoint of the vestibule (V). The line cv_1 passes through the spiral center and is orthogonal to cv_2. Angular insertion depth (θ) is measured from the geometric 0 deg reference, which is the line from the spiral center through the intersection of cv_1 and cv_2. The location of the RW entry, which is near the intersection of cv_2 and the electrode array, is measured from the 0 deg reference and shown here as θ_3. LSC is the lateral-semicircular canal. Modified image from Ref. [12] reproduced with permission of Wolters Kluwer Health.

parallel to the plane of the SSC, the SSC appears as a single structure [10]. Otherwise, it would appear as an elliptical loop similar to the view of the lateral-semicircular canal in Fig. 3. The line cv_2 in Fig. 3 drawn from the apex of the SSC through the center of the vestibule will lie in both the planes of the SSC and the film plane. The line cv_1 is drawn in the film plane orthogonal to cv_2, and by extension, must be orthogonal to the plane of the SSC.

The vertex view of Fig. 4 implies that the line-of-sight and the SSC plane are orthogonal to any transverse plane of the body (Fig. 5). Since θ_1 is neither 0 deg nor 90 deg, the SSC plane is never orthogonal to the coronal or sagittal planes. Therefore, cv_1 must lie on a transverse plane. This is convenient given that the infraorbitomeatal plane (sometimes referred to as the skull's horizontal plane [12]) can also be reasonably assumed to be parallel with any transverse plane. θ_3 can then be regarded as the angle between the infraorbitomeatal plane and the RW in the plane of the film (i.e., the plane of the basal cochlear turn), providing the anatomic landmark by which to interpret θ_3.

Since we are interested in orienting a phantom relative to a tabletop as in Fig. 1, the cochlear orientation relative to anatomic landmarks must be converted into angles relative to the operating table. The solution is as simple as implementing a series of coordinate frame rotations (Fig. 5). First, we assume the patient's back lies flat on an operating table whose surface is parallel with all coronal planes and orthogonal to all sagittal and transverse planes. Next, we define a cochlear Cartesian frame consisting of three orthogonal vectors that are initially aligned with the superior, lateral, and anterior vectors. The orientation of the modiolar axis is identical to the orientation of the anterior axis after the cochlear frame has been initially rotated by $-\theta_1$ about the superior axis (Fig. 5(*a*)) followed by a rotation of $+\theta_2$ about the new lateral axis (Fig. 5(*b*)). The 0 deg reference in Fig. 3 is identical to this new lateral axis. The location of the RW is located on the final lateral axis after rotation by $+\theta_3$ about the final anterior axis (Fig. 5(*c*)). The modiolar axis orientation relative to a tabletop surface as in Fig. 1 requires a final rotation of the cochlear frame by +65 deg about the original superior axis (not shown).

Table 1 Cochlea orientation with respect to anatomic landmarks

Description	References	Value
θ_1 between midsagittal plane and spiral axis of the cochlea	[10] [12]	40 deg 37.5 deg (range of 15.5 deg)
θ_2 between infraorbitomeatal plane and spiral axis of the cochlea	[10] [12]	0 deg 1.8 deg (range of 6 deg)
θ_3 locates round window in the plane of basal turn	[11] [9,14]	13.47 deg 13.5 deg (range of 12.4 deg)

3 Insertion Openings

Access to the ST for CI insertions are typically achieved through an incision in the RW membrane or through a cochleostomy sited anteroinferior to the RW on the cochlear promontory. The actual RW opening is typically sited on the vertical segment of the RW membrane (situated anteroinferiorly) rather than its horizontal segment (located posterosuperiorly) [16]. This is shown in the lower-left inset of Fig. 6 in which the RW opening is located in the apical half (i.e., the vertical segment) of the RW membrane. The mean entry points through the RW and through a

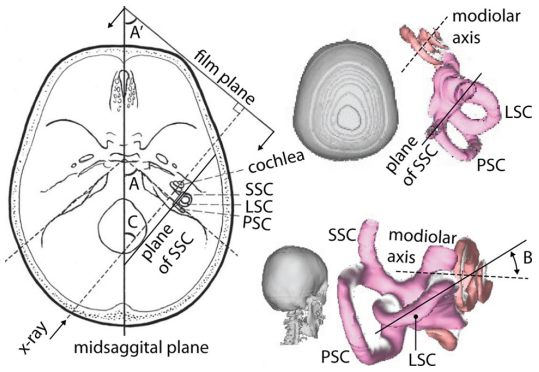

Fig. 4 The skull positioning of Fig. 2 was confirmed through more rigorous measurements using numerous temporal bones [12]. To confirm Fig. 2(*a*), they computed the angle *A* between the line passing the lower arm of the posterior semicircular canal (PSC) and the midsagittal plane, and assumed that *A* is nearly identical to *A*′ (left image). The mean value of *A* (for *n* = 102) is 52.5 deg. *C* is the complementary angle of *A* and is identical to θ_1 in Table 1 and Fig. 2. Next, to confirm Fig. 2(*b*), they computed the angle *B* between the lateral-semicircular canal (LSC) and the modiolar axis (bottom-right image). The mean value of *B* (for *n* = 10) is 28.2 deg. Since the LSC forms an angle of 30 deg upward from the infraorbitomeatal plane, they concluded that the modiolar axis is nearly parallel to this plane. Viewing the film plane in the direction indicated by the arrows results in the cochlear-view radiograph shown in Fig. 3. Modified left image is from Ref. [12] reproduced with permission of Wolters Kluwer Health. The right images are generated using software available for public use [15].

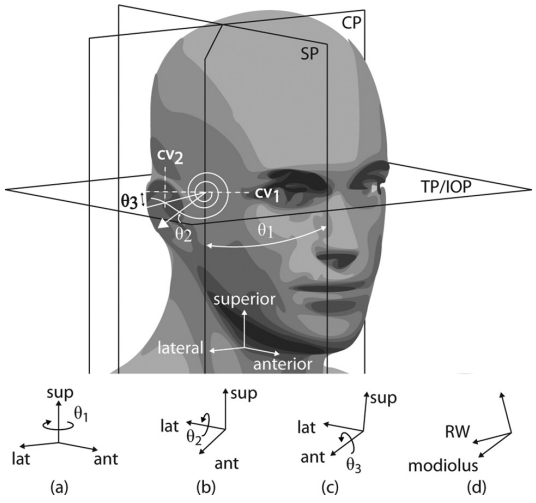

Fig. 5 Top: Orientation angles of Table 1 and cochlear-view axes (lines cv_1 and cv_2) are shown relative to the three orthogonal reference planes of the body: the sagittal plane (SP), coronal plane (CP), and the transverse plane (TP). θ_3 is measured in the plane formed by cv_1 and cv_2; modified public domain image. Bottom: cochlea orientation angles (shown as a series of successive rotations of a Cartesian frame originally aligned with the reference planes).

cochleostomy just apical of it are given as 13.5 deg (θ_3 in Table 1) and 23.8 deg, respectively, as measured in the plane of the basal cochlear turn from the 0 deg reference of the cochlear view [9]. The corresponding linear distances to these entry points are

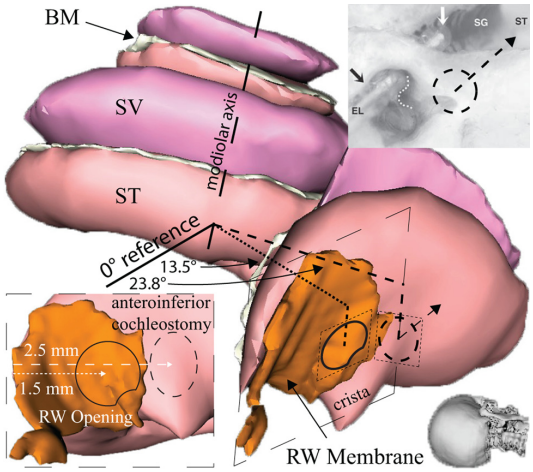

Fig. 6 Virtual model of the cochlea showing the basal end of the scala tympani (ST) as seen through the facial recess during surgery with an enlarged view of the RW region provided in the lower-left inset. Depictions of both insertion openings, RW opening and anteroinferior cochleostomy, are superimposed onto the virtual model to provide approximate locations with respect to the RW membrane. Basilar membrane (BM), scala vestibuli (SV), and the skull position corresponding to the cochlea orientation are provided for reference. Image is generated using software available for public use [15]. Top-right: posterior-superior lip of RW niche (black arrow) and bony projection from crista (outlined by dotted white line) restrict the angle of electrode (EL) entry so that the electrode tip (white arrow) is directed toward modiolar wall and spiral ganglion (SG) rather than the ST lumen. A well placed cochleostomy (shown as a dashed circle) can facilitate direct insertions into the ST lumen (dashed arrow). Modified image from Ref. [16] reproduced with permission of John Wiley and Sons.

approximately 1.5 mm and 2.5 mm as measured from the basal end of the ST. A virtual model of the cochlea, with approximate locations of the insertion holes, is shown in Fig. 6.

While a cochleostomy insertion can be replicated by a properly positioned hole, to model a RW insertion is more complicated due to the anatomy of the RW region. The RW membrane is recessed within a bony cavern called the RW niche (Fig. 7), which, in combination with the crista (i.e., the bony ridge adjacent to the RW membrane), restrict the entry angle such that the tip is directed toward the modiolar wall upon insertion [16] (top-right inset of Fig. 6). In extreme cases, where this interference prevents a compatible electrode path, reducing the posterior-superior lip of the RW niche and enlarging the opening at the anteroinferior margin will allow the surgeon to make insertions where the electrode is more aligned with the ST lumen. Since surgeons have the ability in practice to modify the anatomy for better visibility and access to the RW membrane [16,17], we assume that the surgeon has made the membrane accessible and replicate RW insertions by modeling only the incision into the RW membrane as an opening with a small protrusion near 5 o'clock to account for the obstruction due to the crista (bottom-left inset of Fig. 6).

Insertions through the RW are further complicated by a narrowing of the ST near the RW. This is illustrated in Fig. 7 as the cross-sectional width and height of the ST decrease toward the basal end of the RW. This narrowing is further exacerbated by a clockwise rotation of the osseous spiral lamina (OSL) from vertical at the posterior edge of the RW to more oblique angles deeper within the basal turn [18]. Thus, the initial trajectory of the electrode array is aligned with the short dimension of the ST rather than its long dimension. For example, at the middle of the RW

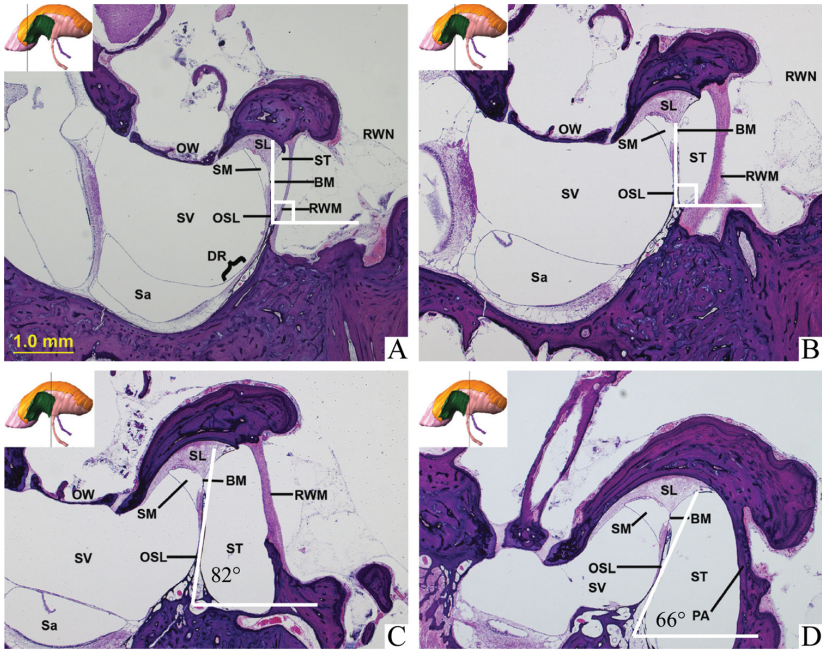

Fig. 7 Histological cross sections in the basal end of the cochlea. BM, basilar membrane; OSL, osseous spiral lamina; RWN, round-window niche; RWM, round-window membrane; SM, scala media; ST, scala tympani; SV, scala vestibuli. Modified images from Ref. [26] reproduced with permission of Lippincott Williams and Wilkins.

membrane, the long dimension of the ST has been effectively rotated away from the insertion direction such that the clearance between the inner wall of the ST and the electrode array tip upon insertion is only about 0.5 mm (Fig. 7(*b*)).

To model the narrowing of the RW region, we first note that the ST terminates near the RW [18], and assume that the basal end of the RW is near the beginning of the ST. Next, we approximate the RW membrane as a circle with a diameter of 2 mm, which is consistent with the dimensions reported by Nomura [19] and Erixon et al. [20]. Thus, the basal and apical end of the RW (Figs. 7(*a*) and 7(*c*)) corresponds to a distance of 0 mm and 2 mm, respectively, from the ST's beginning. With this, we can now align the various histological measurements, often given with respect to different reference markers [21–26].

Since detailed measurements of the OSL angle in the basal region of the cochlea are lacking in the available literature, we estimate this parameter by inspecting the OSL angle in the histology images found in Refs. [18,26] and with the software used to generate Fig. 6. (These estimates are listed in Table 3 as the ϕ values from $d = 0$ mm to $d = 5$ mm).

4 Consensus Cochlear Coordinates

To address the need to standardize CI insertion evaluations, a 3D cylindrical coordinate system, well suited for clinical measurements of CI insertions, was agreed upon by a panel of prominent researchers and manufacturers [9]. We adopt this coordinate system so that insertion experiments can be evaluated with the same metric as clinical insertions. A plane through the basal turn of the cochlea perpendicular to the modiolus is chosen as the plane of rotation. This is equivalent to the cochlear view, making this consensus framework straightforward to implement in our phantom. Angular measurements are measured from the center of the RW rather than the 0 deg reference of the cochlear view. The z-axis is placed through the center of the modiolus, with its origin at the level of the helicotrema (the apex of the cochlea). The radial distance from the modiolus to the implant completes the third component of the cylindrical coordinate system. Because our phantom is developed from a spiral model that computes radius and height as a function of angle (Eqs. (1)–(3)), the three coordinate values can be parameterized by a single angular measurement.

5 Construction of Scala-Tympani Phantom

5.1 Modeling the Scala Tympani. We now summarize the process to model the ST, which was originally described by Clark et al. [1]. The 3D spiral shape of the ST, expressed in cylindrical coordinates, can be described by the following equations:

$$R = C(1 - D\ln(\theta - \theta_0)) \qquad \theta < 100\,\text{deg} \qquad (1)$$

$$R = Ae^{-B(0.0002\theta^2 + 0.98\theta)} \qquad \theta \geq 100\,\text{deg} \qquad (2)$$

$$z = E(\theta - \theta_1) \qquad (3)$$

R is the distance from the spiral center in mm, z is the height value in mm, and θ is the angle in degrees. Equations (1) and (2) are based on the spiral template of the cochlear view (Fig. 3). The values for constants A, B, C, D, E, θ_0, and θ_1 are listed in Table 2. We generate the spiral curve for a range of θ from 6.8 deg to 910.3 deg in 0.1 deg increments (Fig. 8).

Starting at the basal end of the spiral and at each 1 mm increment toward the apical end, we model the ST sections (Fig. 8) as

Table 2 Values for constants of equations (1), (2), and (3)

A (mm)	B (mm)	C (mm)	D (mm)	E (mm)	θ_0 (deg)	θ_1 (deg)
3.762	0.001317	7.967	0.1287	0.003056	5.0	10.3

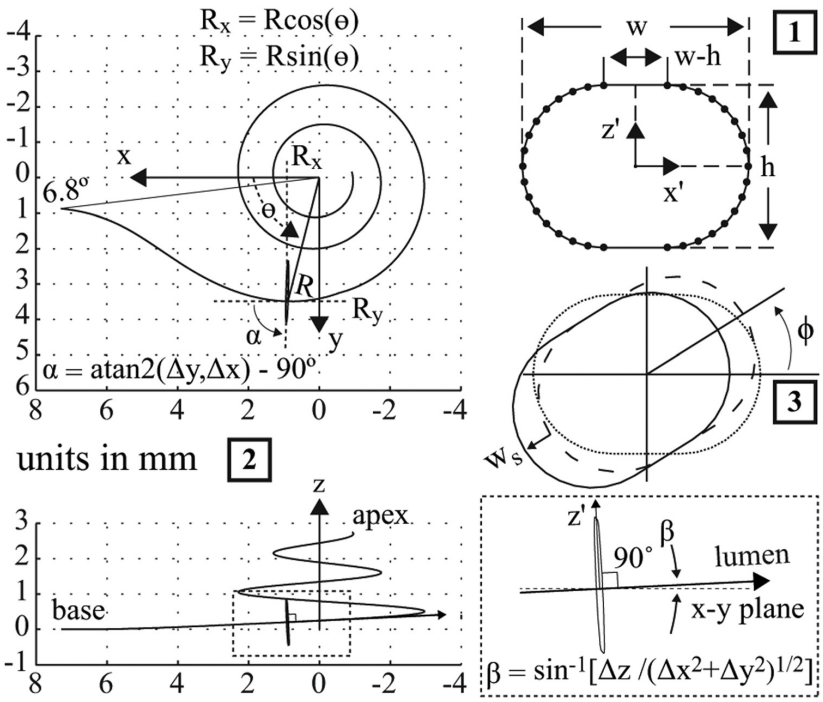

Fig. 8 Steps to model the scala tympani. (1) Create sections parameterized by *h* and *w*. (2) Place the origin of each section (intersection of *x*′ and *z*′) onto the spiral at 1 mm increments from its beginning, with *z*′ initially aligned with *z*, and orient the section such that it is orthogonal to the local spiral direction. (3) Rotate section counterclockwise by ϕ and shift section medially by w_s.

semicircular ends, connected by straight segments, parameterized by width and height values given in Table 3. The ST width and height from the previous phantom [1] were taken from Wysocki's mean width and height measurements of 25 temporal bones taken at 1 mm increments from the ST's beginning [21]. However, the ST height seemed undersized based on our experience. This is confirmed by comparing Wysocki's data against other published data [22–25] (Fig. 9). Since, in our opinion, this discrepancy indicates a systemic error with Wysocki's data, we averaged the height data from the other publications and use this for the ST height values instead. We also confirmed that no change was needed for the ST width as Wysocki's width measurements were consistent with the other data sets. Each section is oriented so that it is orthogonal to the lumen, rotated by ϕ to model the OSL angle, and shifted medially by w_s (Fig. 8) to better match Cohen's silastic models [11] and Kawano's reconstructions [27] (Fig. 10).

We note that the section at 0 mm in Ref. [1] is equivalent to the section at 2 mm here. The reason is that previously the first two cross sections were ignored, shortening the overall length of the ST and widening the phantom's opening. To include these initial cross sections, we extend the starting point of the spiral template from 10.3 deg to 6.8 deg. The previous starting point (10.3 deg) was used to approximate the basal end of the organ of Corti [28]. More recently, some have concluded that the actual basal end of the organ of Corti is likely closer to 5 deg than to 10 deg, which would indicate an earlier start angle [9]. Moreover, by lengthening the basal end of the spiral, the angular locations of the RW opening and cochleostomy are better matched to the appropriate linear distances from the basal end (see Fig. 6 inset). That is, the locations of the RW opening and the cochleostomy (the intersections of our ST's outer wall with 13.5 deg and 23.8 deg lines, respectively) should be about 1.5 mm and 2.5 mm, respectively, from the basal end (Fig. 11). Finally, the values for ϕ at 6 and 7 mm are interpolated to provide a smooth transition from the estimated OSL values to the values originally determined by Clark et al. from 8 mm on.

5.2 Phantom Design and Fabrication. The phantom design based on the modeled ST is illustrated in Fig. 12 and is based on the process detailed by Clark et al. [1]. Our phantom is designed such that if placed on a tabletop, the ST's orientation matches the values in Table 1. The angular grid is designed with the 0 deg reference through the center of the RW. An exit hole is placed at the top of the phantom to allow for fluid to travel through the cavity.

We model the cochleostomy opening as a 1.2 mm diameter hole centered near the intersection of the 23.8 deg line with the outer boundary of our modeled ST. Since the primary feature of a cochleostomy insertion is an initial electrode trajectory in line with the ST lumen (i.e., the longitudinal axis of the ST) [18], we orient the opening toward the lumen. The size of the opening is somewhat arbitrary as it will depend on surgeon preference and manufacturer recommendations. For example, a survey of surgeons resulted in a preferred cochleostomy range between 0.8 and 2.0 mm [29].

Similarly, the RW opening is a 1.2 mm diameter hole centered near the intersection of the 13.5 deg line with the outer boundary of our modeled ST. Since the phantom is essentially a solid structure with a cavity representing the ST, the insertion openings will have a tunnel effect due to the material wall thickness at the opening. This effect is an artifact of the design, and is not an inherent characteristic of the surgical insertion. To minimize this effect for RW insertions, we trim material to the boundary of the cavity (shown as a red dashed line in Fig. 12) to a wall thickness of

0.3 mm. This is not necessary for cochleostomy insertions since this artifact does not affect the initial electrode trajectory. Finally, a small protrusion near 5 o'clock is added to the RW opening to account for the obstruction due to the crista.

A usable phantom requires it to be transparent enough to visualize the implant during insertions and have a smooth internal surface to mimic the endosteum lining of the ST [6]. A multistep casting process, such as that used in the investment casting of jewelry, has been successfully used to produce transparent cochlea models [7]. However, the complexity of this multistep process is not ideal where only a few phantoms are desired. A simpler method is to 3D print the device directly from software.

We now note some limitations with 3D printing that affect the usability of this device. First, not all additive manufacturing processes can build with transparent materials. Second, the layer-by-layer building operations inherent in these processes leave a stair-step finish. Thus, the smoothness of the surface is limited by the resolution of the build layers. Third, designs with complex geometries, such as overhangs and tunnels often require the deposition of support material to act as a temporary scaffold while these features are built. In the case of our phantom, removal of this temporary support structure from within the internal cavity is difficult. Fourth, a nonsmooth surface finish usually results where the temporary support structure contacts the actual build material. Surface polishing, often used to smooth out these aforementioned features, is not a viable option since the internal channel is not easily accessible. It is conceivable that continual advancements in 3D printing technology will render these concerns obsolete in the future. For now, the best results are achieved by high-resolution machines that can build complex geometries with minimal, easily removable, support material.

We produced two sets of phantoms using the machines in Table 4. The Viper si2 SLA is a high-definition stereolithography machine capable of building in transparent plastic (Watershed XC11122) without requiring any support material, eliminating the problem of support-material removal from the internal cavity. The next generation of microstereolithography machines is capable of better resolutions and accuracies, but at this time is not widely available. The ProJet HD 3000*Plus*, operated in Xtreme high definition (XHD) mode, has the best resolution and accuracy in its class. The support material is completely meltable, allowing for hands-free removal of the build-support structures. The primary negative is that a transparent material is currently not available for use with this printer, which is not ideal for visualizing insertions. The SOLIDWORKS (Waltham, MA) renderings and the manufactured phantoms are shown in Fig. 13 with a MED-EL (Innsbruck, Austria) standard electrode inserted into them.

To account for the machine's resolution and accuracy, we recommend an enlarged ST channel to minimize the possibility that an undersized channel is produced. This adjustment seems reasonable given that an undersized ST will unnecessarily hinder insertion experiments. Rebscher et al. oversized the ST cavity in their ST model by 14% for this specific reason [7]. For a 1 mm × 2 mm cross section, this amounts to 0.14 mm to 0.28 mm. For perspective, the average of published standard deviations is about 0.14 mm [21–24]. Our ST prototypes are oversized by 0.14 mm in both width and height beyond the values given in Table 3.

5.3 Validation. We validate the usefulness of our phantoms through insertion experiments similar to those described in Ref. [2]. To automate the insertions, standard MED-EL electrodes are mounted to a Thorlabs (Newton, NJ) MTS50/M-Z8 linear stage. By rigidly mounting the phantoms onto an ATI (Apex, NC) Nano17, six-axis, force-torque sensor (3.125 mN resolution), forces on the phantoms can be measured during automated insertions. Prior to each insertion, the channel is filled with saline solution and the electrode tip is positioned just inside the opening.

The first set of experiments compares our cochleostomy phantom with the cochleostomy phantoms available through the three

Table 3 Values for the independent parameters (shown in Fig. 8) used to generate and locate the ST sections. *d* is the distance along the spiral from its beginning at $\theta = 6.83$ deg. *h* and *w* are the ST height and width, respectively, ϕ is the osseous spiral lamina angle, and w_s is the distance to shift the sections medially.

d (mm)	0	1	2	2.5	3	4	5	6	7	8	9	10	11	12	13	14	15	16	17
θ (deg)	6.8	9.5	15.1	19.0	23.5	34.3	46.7	60.4	75.3	91.3	108.4	126.1	144.2	162.8	181.9	201.5	221.6	242.4	263.7
h (mm)	0.3	0.6	1.30	1.58	1.53	1.36	1.33	1.28	1.27	1.26	1.22	1.18	1.14	1.10	1.07	1.03	1.00	0.97	0.96
w (mm)	0.7	1.5	2.10	2.10	2.10	1.95	1.85	1.80	1.74	1.70	1.68	1.63	1.60	1.59	1.51	1.50	1.54	1.46	1.45
ϕ (rad)	1.57	1.57	1.43	1.17	0.97	0.56	0.00	0.02	0.04	0.06	0.07	0.08	0.09	0.10	0.11	0.12	0.13	0.14	0.15
w_s (mm)	0.0	0.0	0.0	0.0	0.0	0.0	0.3	0.3	0.28	0.26	0.24	0.28	0.28	0.32	0.35	0.4	0.5	0.55	0.62
d (mm)	18	19	20	21	22	23	24	25	26	27	28	29	30	31	32	33	34	35	36
θ (deg)	285.8	308.5	332.0	356.4	381.6	407.8	435.1	463.6	493.4	524.6	557.3	591.9	628.4	667.2	708.6	753.0	800.9	853.0	910.1
h (mm)	0.93	0.92	0.92	0.92	0.91	0.91	0.92	0.94	0.93	0.89	0.82	0.76	0.73	0.77	0.73	0.70	0.65	0.67	0.58
w (mm)	1.43	1.38	1.33	1.32	1.31	1.30	1.30	1.30	1.30	1.30	1.30	1.30	1.31	1.31	1.26	1.15	1.23	1.25	1.45
ϕ (rad)	0.16	0.17	0.18	0.19	0.20	0.21	0.22	0.23	0.24	0.25	0.26	0.27	0.28	0.29	0.30	0.25	0.20	0.15	0.10
w_s (mm)	0.62	0.6	0.6	0.65	0.66	0.67	0.68	0.65	0.65	0.65	0.57	0.49	0.41	0.33	0.25	0.17	0.09	0.01	0.01

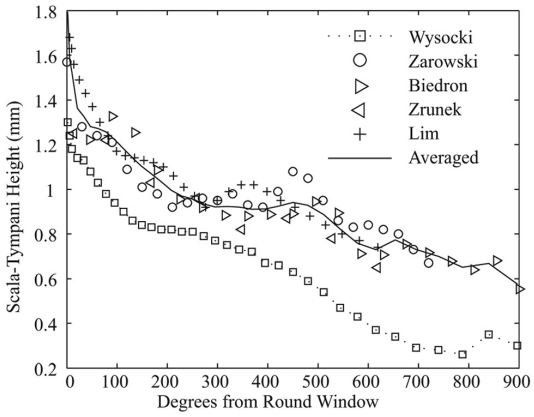

Fig. 9 Wysocki's height data [21] is smaller than other published values [22–25]. The solid line is the average of the non-Wysocki data sets.

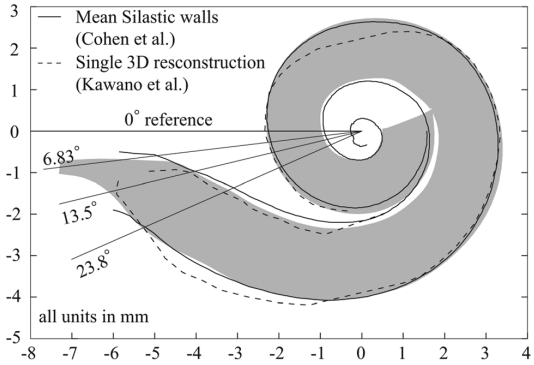

Fig. 10 Our scala-tympani model (shown in gray and limited to 1.5 turns to reduce visual clutter) is compared with Cohen's silastic models [11] and Kawano's reconstructions [27]. The intersections of the outer wall of our model with the 13.5 deg and 23.8 deg lines are the respective entry points through the round-window opening and an anteroinferior cochleostomy. Modified image from Ref. [9] reproduced with permission of Wolters Kluwer Health.

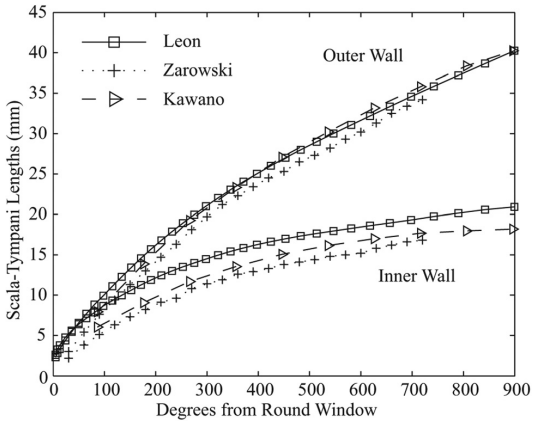

Fig. 11 Our scala-tympani wall lengths compared with published data [22,27]

Table 4 Machines used to build prototypes of Fig. 13

3D Systems (Rock Hill, SC)	ProJet HD 3000*Plus*	Viper si2 SLA
Layer thickness (μm)	16 (XHD Mode)	51 (Hi Res Mode)
Accuracy (μm)	25–50	127
Material	VisiJet Crystal	Watershed XC11122

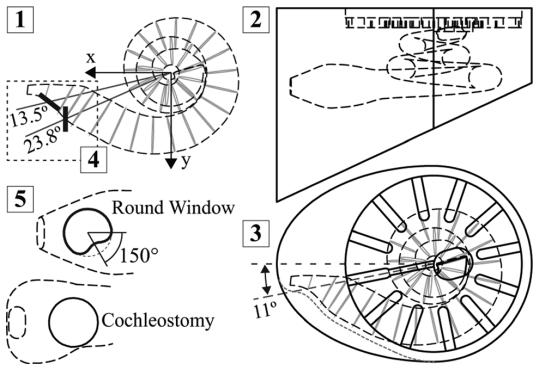

Fig. 12 Steps to design phantom in SolidWorks. (1) Create loft from imported *x-y-z* points that model the scala tympani. (2) Build a structure around the lofted cut to orient the phantom appropriately. (3) Create the angular grid system and an exit hole near center of the dial. For the round-window version, we trim material along the cavity boundary (red-dashed line) to reduce the tunnel effect from the phantom's wall thickness at the round-window opening. (4) Create sketch planes where the 13.5 deg and 23.8 deg lines intersect the lofted cut. (5) Create insertion openings on the defined sketch planes.

major CI device manufacturers (Fig. 14). The version from Advanced Bionics is made through a multistep casting process, but it models all three scala chambers as a single cavity. This overstates the channel size that the electrode travels through and makes insertions easier, which is especially evident for deeper insertions.

The version by MED-EL is made using stereolithography and has the shortest section between the opening and the basal turn. Thus, in the MED-EL model, electrodes travel a shorter distance to reach the same angular insertion depth as compared with the others and have the effect of overstating the insertion forces at deeper insertions.

The version by Cochlear (Sydney, Australia) is only a planar model. That is, it does not replicate a full 3D path for the electrode to travel through. The measured insertion forces are between the lower and upper bound set by Advanced Bionics and MED-EL, respectively.

The two versions of our cochleostomy phantoms are identified as numbers 4 and 5 in Fig. 14. Phantom 4 performed similarly to the version by Cochlear and phantom 5 resulted in lower insertion forces than phantom 4. This suggests that the ProJet HD 3000*Plus* produces a device with a smoother internal surface finish than that made by the Viper si2 SLA. This is consistent with the stated machine resolution and accuracy tolerances provided by manufacturer (Table 4). A significant disadvantage of the ProJet HD 3000*Plus* is that the material is only semitransparent and does not provide good visualization of an electrode inside it. Since both devices perform comparably with those widely in use, we recommend using the version made with the completely transparent plastic.

The second set of experiments compares our RW phantom with cadaver cochleae to determine if insertion force experiments conducted in our device can be a reliable indicator of insertion force measurements in an actual cadaver cochlea (Fig. 15). Unlike the

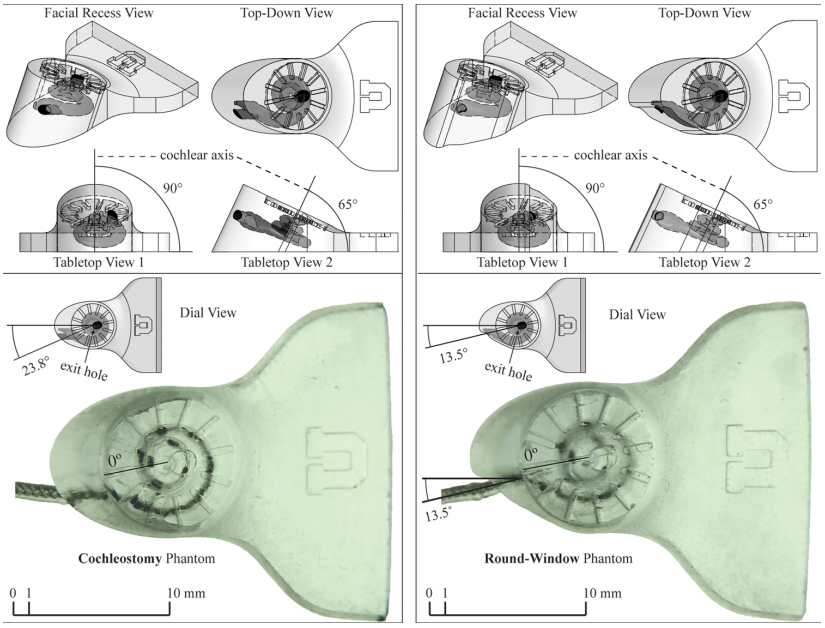

Fig. 13 SolidWorks renderings of the cochleostomy (top-left) and round-window (top-right) versions of our scala-tympani phantom are used to manufacture the corresponding devices below. The tabletop views assume the phantom is lying on a flat surface with the observer's line-of-sight at the level of the phantom. The facial recess views approximate the surgeon's view of the insertion openings, in the spirit of Fig. 6. The top-down views are taken above the phantom with the line-of-sight along the gravity vector. The dial views assume a line-of-sight directed toward and orthogonal to the face of the dial. Standard MED-EL electrodes are inserted as far as possible before buckling (to approximately 720 deg) into both phantoms.

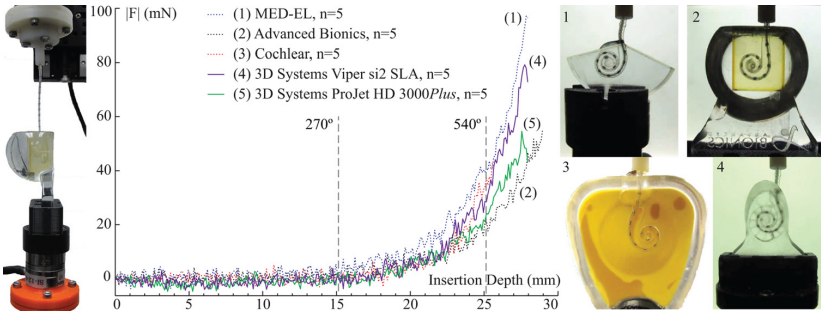

Fig. 14 Insertion force measurements are compared for five different phantoms, each of which is rigidly mounted onto a force sensor with the insertion opening oriented for vertical, automated insertions. An image of phantom number 5 is not provided because its semitransparent material did not provide good visualization of the electrode.

first set of experiments, the automated insertions are not conducted vertically but at an orientation that replicates actual surgical insertions. Bone sections containing the cochleae are dissected out of two temporal bones chosen randomly from the University of Utah Temporal Bone Lab and fixed with paraffin wax in a basket that is rigidly mounted to the force sensor. We carefully open the RW membrane, fill the cochleae with saline solution, and position the electrode with its tip just inside the RW. We conduct one automated insertion into each cadaver cochlea and stop the insertion if buckling occurs to protect the electrode array from permanent damage.

The measured forces are very similar between the cadaver cochleae and the RW phantom. A deeper insertion was achieved with cadaver cochlea 1 than with cadaver cochlea 2. Since the cadaver cochleae are not transparent, it is possible that the insertion stage was slightly misaligned relative to the ST hindering a full insertion. Although the number of cochleae was limited to two, they were chosen randomly, indicating that, in our opinion, insertion forces measured in our RW phantom can be used as an indicator of actual measurements in a cadaver cochlea.

6 Discussion

The orientation of our phantom is largely based on mean values of the required skull orientation angles to produce a radiographic image that is orthogonal to the cochlear axis and parallel to the plane of the basal cochlear turn. Although we have chosen to

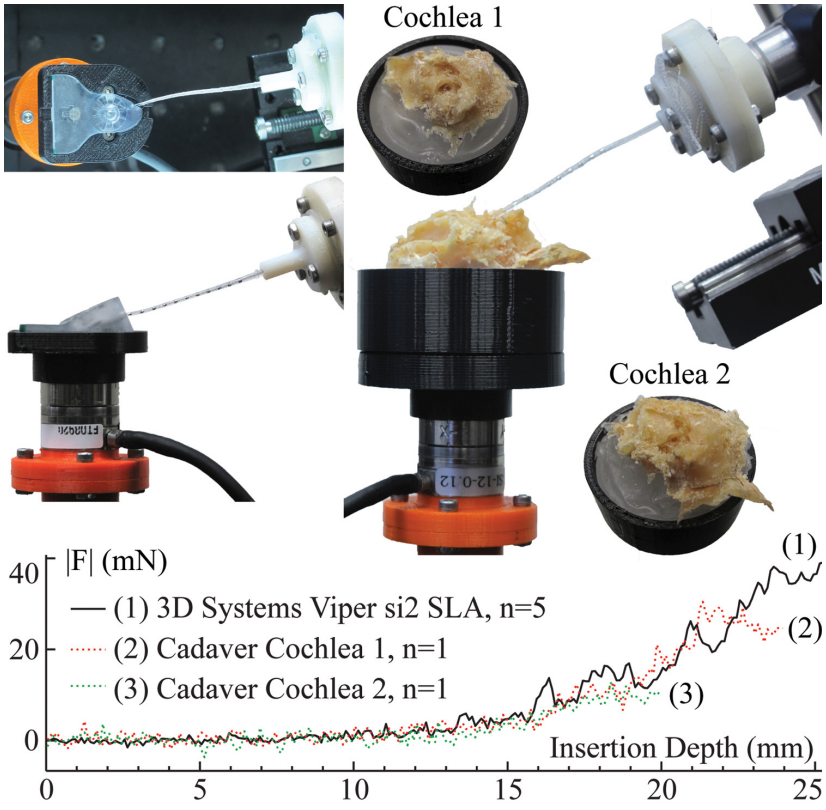

Fig. 15 Insertion force measurements, at clinically accurate insertion angles, are compared between the round-window phantom (left) and cadaver cochleae fixed in baskets with paraffin wax (right), mounted rigidly to the force sensor

incorporate the findings associated with the cochlear view, a different group, also interested in radiologic evaluations of CI insertions, published a different set of skull orientation angles ($\theta_1 = 30$ deg, $\theta_2 = 15$ deg) [30]. They do not, however, provide the location of the RW in their findings, which is a key feature of this phantom. Furthermore, the cochlear view appears to have gained larger clinical acceptance.

To orient the phantom with respect to the tabletop, two key assumptions were made. First, the infraorbitomeatal lines are determined by anatomical landmarks that are set in the patient's skull and will vary from patient to patient. We assume that these lines are parallel to the transverse plane since typically they are nearly horizontal [12]. Second, we assume that axis 2 of the cv_2 lies in the plane of the superior-semicircular canal, allowing us to regard θ_3 with respect to a plane parallel to the infraorbitomeatal plane. This simplifies the orientation of the phantom on a tabletop and is within the listed variability (Table 1).

Our phantom models an anteroinferior cochleostomy, but there is not complete consensus regarding the cochleostomy site through which CI insertions are least traumatic to the delicate intracochlear structures. Most seem to prefer an anteroinferior cochleostomy [8,26,29,31,32], though a cochleostomy that is mostly inferior [18] or mostly anterior [33] to the RW have their proponents. Still others involve the RW membrane itself into the cochleostomy [34]. Regardless, the ideal cochleostomy will facilitate electrode insertions with an insertion trajectory in line with the ST lumen, which we model in our phantom.

Insertions through the RW are actually more complicated than what has been modeled in our phantom because the RW membrane is recessed into a complex, cavernous structure (the RW niche) that limits visibility and access to the membrane. Rather than model the complex niche, which has been attempted [19], we assume that the surgeon has made the membrane accessible and simply model an incision into the RW membrane. Neglecting the niche simplifies the phantom model and is reasonable given that the surgeon has the ability in practice to remove portions of the niche for better visibility and access to the RW membrane [16,17]. That said, our model can be easily reconfigured to simulate the niche by setting the wall thickness at the RW to the measured depth of the niche [35].

Additionally, this phantom does not replicate the access limitations of the facial recess. This is true of all insertion experiments that use either cochlea models or cadaver cochleae that have been dissected out of temporal bones.

An angular grid has been designed into the phantom to accommodate the industry's movement toward standardization. As an added benefit, angular measurements can be interpreted in the context of the cochlea's tonotopic arrangement. That is, the electrode position given as an angular location from the RW can be used to determine the frequencies communicated to the cochlea. Furthermore, a metric of the proximity of the electrode position to the modiolus (to evaluate the effectiveness of modiolus-hugging designs) can be computed by dividing the angular insertion depth by the linear insertion depth [32].

7 Conclusions

A scala-tympani phantom for cochlear-implant insertions through the round-window or a cochleostomy has been presented.

It is primarily aimed at those performing insertion experiments but can also be used as part of an insertion simulation for training or education. More information about these phantoms, including SOLIDWORKS and MATLAB files, can be obtained from the University of Utah's Telerobotics Lab (www.telerobotics.utah.edu).

Acknowledgment

This material is based upon work supported by the National Science Foundation under Grant Nos. 0952718 and 0654414. We would like to thank Brian M. Chin, M.D. (Neuroradiology Fellow at the University of Utah School of Medicine) for his assistance in understanding skull positions of the Cochlear View. We also would like to thank Abhijit Kulkarni, Ph.D. and Kurt Koester, Ph.D. (Advanced Bionics) for insight regarding manufacturing of cochlea models. MED-EL electrode arrays and a MED-EL scala-tympani phantom were provided courtesy of Claude Jolly, Ph.D. and Mr. Anandhan Dhanasingh (MED-EL).

References

[1] Clark, J. R., Warren, F. M., and Abbott, J. J., 2011, "A Scalable Model for Human Scala-Tympani Phantoms," ASME J. Med. Dev., **5**(1), p. 014501.
[2] Clark, J. R., Leon, L., Warren, F. M., and Abbott, J. J., 2012, "Magnetic Guidance of Cochlear Implants: Proof-of-Concept and Initial Feasibility Study," ASME J. Med. Dev., **6**(3), p. 035002.
[3] Zhang, J., Wei, W., Ding, J., Roland, J. T., Jr., Manolidis, S., and Simaan, N., 2010, "Inroads Toward Robot-Assisted Cochlear Implant Surgery Using Steerable Electrode Arrays," Otol. Neurotol., **31**(8), pp. 1199–1206.
[4] Majdani, O., Schurzig, D., Hussong, A., Rau, T., Wittkopf, J., Lenarz, T., and Labadie, R. F., 2010, "Force Measurement of Insertion of Cochlear Implant Electrode Arrays In Vitro: Comparison of Surgeon to Automated Insertion Tool," Acta Otolaryngol., **130**(1), pp. 31–36.
[5] Verbist, B. M., Joemai, R. M. S., Teeuwisse, W. M., Veldkamp, W. J. H., Geleijns, J., and Frijns, J. H. M., 2008, "Evaluation of 4 Multisection CT Systems in Postoperative Imaging of a Cochlear Implant: A Human Cadaver and Phantom Study," Am. J. Neuroradiol., **29**(7), pp. 1382–1388.
[6] Todd, C. A., Naghdy, F., and Svehla, M. J., 2007, "Force Application During Cochlear Implant Insertion: An Analysis for Improvement of Surgeon Technique," IEEE Trans. Biomed. Eng., **54**(7), pp. 1247–1255.
[7] Rebscher, S. J., Talbot, N., Bruszewski, W., Heilmann, M., Brasell, J., and Merzenich, M. M., 1996, "A Transparent Model of the Human Scala Tympani Cavity," J. Neurosci. Methods, **64**(1), pp. 105–114.
[8] Rebscher, S. J., Hetherington, A., Bonham, B., Wardrop, P., Whinney, D., and Leake, P. A., 2008, "Considerations for Design of Future Cochlear Implant Electrode Arrays: Electrode Array Stiffness, Size, and Depth of Insertion," J. Rehabil. Res. Dev., **45**(5), pp. 731–747.
[9] Verbist, B. M., Skinner, M. W., Cohen, L. T., Leake, P. A., James, C., Boëx, C., Holden, T. A., Finley, C. C., Roland, P. S., Roland, J. T., Jr., Haller, M., Patrick, J. F., Jolly, C. N., Faltys, M. A., Briaire, J. J., and Frijns, J. H. M., 2010, "Consensus Panel on a Cochlear Coordinate System Applicable in Histologic, Physiologic, and Radiologic Studies of the Human Cochlea," Otol. Neurotol., **31**(5), pp. 722–730.
[10] Marsh, M. A., Xu, J., Blamey, P. J., Whitford, L. A., Xu, S. A., Silverman, J. M., and Clark, G. M., 1993, "Radiologic Evaluation of Multichannel Intracochlear Implant Insertion Depth," Am. J. Otol., **14**(4), pp. 386–391.
[11] Cohen, L. T., Xu, J., Xu, S. A., and Clark, G. M., 1996, "Improved and Simplified Methods for Specifying Positions of the Electrode Bands of a Cochlear Implant Array," Am. J. Otol., **17**(6), pp. 859–865.
[12] Xu, J., Xu, S. A., Cohen, L. T., and Clark, G. M., 2000, "Cochlear View: Postoperative Radiography for Cochlear Implantation," Am. J. Otol., **21**(1), pp. 49–56.
[13] Skinner, M. W., Holden, T. A., Whiting, B. R., Voie, A. H., Brunsden, B., Neely, J. G., Saxon, E. A., Hullar, T. E., and Finley, C. C., 2007, "In Vivo Estimates of the Position of Advanced Bionics Electrode Arrays in the Human Cochlea," Ann. Otol. Rhinol. Laryngol. Suppl., **116**(4), pp. 2–24.
[14] Verbist, B. M., Joemai, R. M., Briaire, J. J., Teeuwisse, W. M., Veldkamp, W. J., and Frijns, J. H., 2010, "Cochlear Coordinates in Regard to Cochlear Implantation: A Clinically Individually Applicable 3 Dimensional CT-Based Method," Otol. Neurotol., **31**(5), pp. 738–744.
[15] Wang, H., Northrop, C., Burgess, B., Liberman, M. C., and Merchant, S. N., 2006, "Three-Dimensional Virtual Model of the Human Temporal Bone: A Stand-Alone, Downloadable Teaching Tool," Otol. Neurotol., **27**(4), pp. 452–457.
[16] Roland, P. S., Wright, C. G., and Isaacson, B., 2007, "Cochlear Implant Electrode Insertion: The Round Window Revisited," Laryngoscope, **117**(8), pp. 1397–1402.
[17] Lenarz, T., Stover, T., Buechner, A., Paasche, G., Briggs, R., Risi, F., Pesch, J., and Battmer, R.-D., 2006, "Temporal Bone Results and Hearing Preservation With a New Straight Electrode," Audiol. Neurotol., **11**(Suppl. 1), pp. 34–41.
[18] Briggs, R. J. S., Tykocinski, M., Stidham, K., and Roberson, J. B., 2005, "Cochleostomy Site: Implications for Electrode Placement and Hearing Preservation," Acta Otolaryngol., **125**(8), pp. 870–876.
[19] Nomura, Y., 1984, "Otological Significance of the Round Window," Adv. Otorhinolaryngol., **33**, pp. 1–162.
[20] Erixon, E., Högstorp, H., Wadin, K., and Rask-Andersen, H., 2009, "Variational Anatomy of the Human Cochlea: Implications for Cochlear Implantation," Otol. Neurotol., **30**(1), pp. 14–22.
[21] Wysocki, J., 1999, "Dimensions of the Human Vestibular and Tympanic Scalae," Hear. Res., **135**(1–2), pp. 39–46.
[22] Zarowski, A., Offeciers, E., Postnov, A., Vanpoucke, F., and Peeters, S., 2008, "Micro-CT Anatomical Measurements in the Human Cochlea," *Auditory Research Bulletin 2007 Biennial Edition*, Advanced Bionics LLC, Valencia, CA.
[23] Biedron, S., Prescher, A., Ilgner, J., and Westhofen, M., 2010, "The Internal Dimensions of the Cochlear Scalae With Special Reference to Cochlear Electrode Insertion Trauma," Otol. Neurotol., **31**(5), pp. 731–737.
[24] Zrunek, M., Lischka, M., Hochmair-Desoyer, I., and Burian, K., 1980, "Dimensions of the Scala Tympani in Relation to the Diameters of Multichannel Electrodes," Eur. Arch. Otorhinolaryngol., **229**(3–4), pp. 159–165.
[25] Lim, Y. S., Park, S.-I., Kim, Y. H., Oh, S. H., and Kim, S. J., 2005, "Three-Dimensional Analysis of Electrode Behavior in a Human Cochlear Model," Med. Eng. Phys., **27**(8), pp. 695–703.
[26] Li, P. M. M. C., Wang, H., Northrop, C., Merchant, S. N., and Nadol, J. B., Jr., 2007, "Anatomy of the Round Window and Hook Region of the Cochlea With Implications for Cochlear Implantation and Other Endocochlear Surgical Procedures," Otol. Neurotol., **28**(5), pp. 641–648.
[27] Kawano, A., Seldon, H. L., and Clark, G. M., 1996, "Computer-Aided Three-Dimensional Reconstruction in Human Cochlear Maps: Measurement of the Lengths of Organ of Corti, Outer Wall, Inner Wall, and Rosenthal's Canal," Ann. Otol. Rhinol. Laryngol., **105**(9), pp. 701–709.
[28] Yoo, S. K., Wang, G., Rubinstein, J. T., Skinner, M. W., and Vannier, M. W., 2000, "Three-Dimensional Modeling and Visualization of the Cochlea on the Internet," IEEE Trans. Inf. Technol. Biomed., **4**(2), pp. 144–151.
[29] O'Connor, E. F., and Fitzgerald, A., 2010, "Hearing Preservation Surgery: Current Opinions," Adv. Otorhinolaryngol., **67**, pp. 108–115.
[30] Czerny, C., Steiner, E., Gstoettner, W., Baumgartner, W. D., and Imhof, H., 1997, "Postoperative Radiographic Assessment of the Combi 40 Cochlear Implant," Am. J. Roentgenol., **169**(6), pp. 1689–1694.
[31] Adunka, O. F., and Buchman, C. A., 2007, "Scala Tympani Cochleostomy I: Results of a Survey," Laryngoscope, **117**(12), pp. 2187–2194.
[32] Wardrop, P., Whinney, D., Rebscher, S. J., Luxford, W., and Leake, P., 2005, "A Temporal Bone Study of Insertion Trauma and Intracochlear Position of Cochlear Implant Electrodes. II: Comparison of Spiral Clarion and HiFocus II Electrodes," Hear. Res., **203**(1–2), pp. 68–79.
[33] Boyd, P. J., 2011, "Potential Benefits From Deeply Inserted Cochlear Implant Electrodes," Ear Hear., **32**(4), pp. 411–427.
[34] Majdani, O., Rau, T. S., Baron, S., Eilers, H., Baier, C., Heimann, B., Ortmaier, T., Bartling, S., Lenarz, T., and Leinung, M., 2009, "A Robot-Guided Minimally Invasive Approach for Cochlear Implant Surgery: Preliminary Results of a Temporal Bone Study," Int. J. Comput. Assist. Radiol. Surg., **4**(5), pp. 475–486.
[35] Su, W.-Y., Marion, M. S., Hinojosa, R., and Matz, G. J., 1982, "Anatomical Measurements of the Cochlear Aqueduct, Round Window Membrane, Round Window Niche, and Facial Recess," Laryngoscope, **92**(5), pp. 483–486.

CHAPTER 4

AN IN-VITRO INSERTION-FORCE STUDY OF MAGNETICALLY GUIDED, LATERAL-WALL, COCHLEAR-IMPLANT ELECTRODES, PART I: VIA COCHLEOSTOMY

Insertion experiments using clinical, lateral-wall-type electrodes through a simulated cochleostomy demonstrate that a statistically significant ($p < 0.05$) reduction in insertion forces, and by as much as 50% for some electrode models, can be achieved using magnetic guidance.

4.1 Abstract

Insertion forces can be reduced by magnetically guiding the tip of lateral-wall, cochlear-implant electrodes during insertion via cochleostomy. Alteration of the electrode tip to accommodate a tiny magnet is required but does not change the insertion characteristic of the electrode.

Steerable electrodes have the potential to minimize intracochlear trauma by reducing the severity of contact between the electrode tip and the lateral walls of the cochlea. We have experimented with lateral-wall electrodes that have been modified to include magnets at their tips, augmenting the superior flexibility of lateral-wall electrodes with a steerable mechanism.

Automated insertions of candidate electrodes are conducted into a scala-tympani phantom with a force sensor attached to it to provide the measurements needed to evaluate our hypothesis. To achieve magnetic guidance, an external magnet is used to apply the necessary magnetic bending torque to the magnetic tip of a clinical electrode with the goal of directing the tip down the lumen.

t-test results indicate that magnetic guidance does reduce insertion forces beyond 8 mm

while eliminating direct tip contact with the lateral wall. The amount of force reduction is electrode dependent and varies from minimal to near 50%. Altering the tip to accommodate a tiny magnet was found to have minor effects on the insertion forces (less than 2 mN) unless it altered the shape of the tip.

Direct contact between the electrode tip and the lateral walls of a scala-typani phantom was eliminated. Insertion forces were reduced by as much as 50% with certain lateral-wall, cochlear-implant electrodes.

4.2 Introduction

Cochlear implants have become the standard treatment for many with sensorineural hearing loss. However, electrode insertion can cause intracochlear trauma if the insertion forces exceed the inherent strength of the tissue [1, 2]. In particular, perforating the basilar membrane is detrimental to hearing preservation [3]. Many studies indicate that minimizing trauma to preserve hearing is a worthy goal [4–6], even if improved speech perception is not necessarily correlated with it [7].

One approach has been to improve upon the insertion characteristics of the cochlear-implant electrodes. Designs of lateral-wall (LW) electrodes have considered parameters such as flexibility [8–11], dimensions [12–19], fabrication technique [20], and material selection [21]. In general, LW electrodes are designed to be thin and flexible so as to minimize trauma when the tip first contacts the LW of the cochlea.

Alternatively, perimodiolar electrodes have a preformed curvature designed to curl away from the LW of the first turn. Prior to insertion, they are straightened with a stylet. During insertion, the electrode is advanced off the stylet (AOS) so that the preformed shape functions as a steering mechanism. Proper technique requires the stylet to be stabilized at the appropriate distance from the cochleostomy site so that the electrode can avoid the LW while being advanced. If done correctly, negligible insertion forces can be achieved while eliminating tip contact with the LW [22–25]. In practice, scalar excursion is a common occurrence with these perimodiolar electrodes precisely at the location where it should be curling away from the LW [26]. This can happen if the stylet is stabilized deeper into the insertion than intended [27]. It can also happen if torsion misaligns the electrode so that its tip curls into the basilar membrane [28]. Considerations for improving the insertion of

perimodiolar electrodes have focused on insertion techniques [23, 25], stylet alternatives [29], curling behavior [30], and automated robotic insertion [22, 24].

Given the success of AOS electrodes, the desire to navigate the first turn of the cochlea has inspired many ideas, all of which require some modification to current electrodes that would tend to make them less flexible [31–35]. To our knowledge, only one of these groups demonstrated actual reduction in insertion forces with their prototypes [35]. This suggests that atraumatic insertions may not be easy to achieve with current prototype steerable electrodes.

We have developed a method to navigate a LW electrode by bending its tip away from the LW of the cochlea during insertion and, in the process, reduce the pressure along the entire length of the electrode against the LW due to the elastic mechanical properties of the electrode. A detailed explanation of the physics is described in our prior work [36], and is only summarized here. The actuation method utilizes an external magnet (EM) to apply bending torque to the tip of an electrode. The electrode is equipped with a permanent magnet rigidly embedded in, or attached to, its tip such that its magnetic dipole (i.e., the vector that points from the magnet's south pole to north pole) is aligned with the long axis of the electrode. In the arrangement shown in Figure 4.1, the applied torque is dynamically changed during operation as follows. As the electrode is continuously inserted into the cochlea, the EM is rotated so that its magnetic dipole is orthogonal to the lumen at the location of the electrode's tip, resulting in the magnetic field applied to the electrode's tip leading the tip magnet by 90°, which is the configuration for maximum magnetic-torque generation on the tip. Simultaneously, the distance between the EM and the electrode's magnetic tip is adjusted to cause the electrode's tip to bend away from the LW. As an added benefit, magnetic forces are approximately zero in this configuration and can be neglected. In practice, the rotation of the EM can be preplanned by segmenting the cochlea [37] to determine the lumen heading as a function of insertion depth.

The amount of bending torque needed is based on the electrode stiffness and is expected to be unique to the specific model of electrode. Since electrode flexibility is a design parameter [9], in practice, the necessary bending torque can also be determined as a function of insertion depth. The translation of the EM relative to the cochlea (as illustrated in Figure 4.1) can be preplanned based on the required torque throughout the insertion. If

the motion of the EM can be determined by the insertion depth, the entire procedure can be completely preplanned for automated insertions that do not require real-time localization of the electrode tip relative to the cochlear walls. Real-time imaging [38, 39], if available, could provide supplemental data during insertion, but it is not necessary. To be clear, insertion depth in this context represents the translation of the insertion device at the proximal end of the electrode, not the lumen depth achieved by the tip, because we assume in a clinical build that the EM would be coordinated to the insertion device and not to the tip location. Otherwise, this would require real-time imaging.

Our prior work [36] suggests that magnetic guidance can reduce insertion forces; however, experiments were conducted with 3-to-1 scale dummy electrodes. This chapter presents the first attempt at steering actual clinical electrode arrays, modified to have a magnetic tip, using magnetic guidance. In addition, all experiments herein are conducted to mimic a clinical arrangement so as to better translate the results toward clinical application. Reduction in insertion force is the primary metric used for evaluation and has been used by other groups to evaluate prototypes and insertion techniques [20, 22, 23, 25, 40]. Temporal-bone histology has the benefit of visualizing the final position of the electrode and examining any intracochlear damage that might have occurred during the insertion, but the complexity of histology and limited access to temporal bones make insertion-force measurements in a transparent scala-tympani phantom a reasonable first step.

In this study, we test two hypotheses: (1) embedding a small magnet at the tip of a LW electrode does not significantly alter its inherent insertion characteristics, and (2) magnetically guiding a LW electrode reduces insertion forces. In our opinion, the main contribution herein is a method to avoid direct tip contact with the LW of the cochlea (an advantage of current perimodiolar electrodes) while keeping the superior flexibility of LW electrodes. This study is presented in two parts: in Part I (herein), we consider insertion via cochleostomy; in Part II, we consider insertion via the round window.

4.3 Materials and Methods

The experimental apparatus used to conduct this study is shown in Figure 4.2. Electrodes, mounted to a robotic linear stage (Figure 4.2-1), are inserted into a scala-tympani phantom through a simulated cochleostomy [41] (Figure 4.2-2). Grid markers are engraved

into the phantom and spaced at 30° increments from the round window as suggested by Verbist et al. [42]. Insertion forces are measured by mounting the phantom rigidly to a magnetically insensitive force-torque sensor (Figure 4.2-3). The motion of the EM (Figure 4.2-4) is coordinated with the insertion using a computer that is programmed with preplanned trajectories prior to experiments. Translation of the EM is accomplished with a robotic linear stage (Figure 4.2-5) while a geared servo-controlled DC motor (Figure 4.2-6) rotates the EM. To isolate the force-torque sensor from the motion of the actuators, the EM is mounted on a completely separate platform (Figure 4.2-7), and the electrode-insertion assembly is mounted on an optics bench that sits on sorbothane pads (Figure 4.2-8). A camera system (Figure 4.2-9) captures video of the insertion experiment. The electrode holder is aligned to the cochleostomy opening (Figure 4.2-10), and the rotation axis of the EM is aligned with the central (modiolar) axis of the scala-tympani model (shown by the dashed line in Figure 4.2).

The force-torque sensor used is an ATI (Apex, NC) Nano17 Titanium, factory calibrated to ATI's SI-8-0.05 specification. This yields a sensor resolution of 1.5 mN for all three-axes. A tool transform is implemented in software so that the measurements correspond to the origin of the phantom's coordinate system.

N52-grade NdFeB magnets were obtained from SuperMagnetMan (Birmingham, AL). The EM is a cube of 50-mm side-length with an estimated dipole moment of 131 $A \cdot m^2$. As implemented in our apparatus, the maximum magnetic field that can be generated at the center of the scala-tympani phantom is 225 mT. Cylindrical axially magnetized magnets (0.25-mm diameter by 0.41-mm length) were selected to fit into the tips of the electrodes used in this study.

All electrodes used (see Figure 4.3) were provided by MED-EL (Innsbruck, Austria). They consisted of three electrodes with magnets (labeled E1, E2, and E3) to test our concept and two unmodified reference electrodes (labeled R1 and R2) that served as our control group. In two of the three electrodes with magnets (E1 and E2), the silicone rubber used to encapsulate the magnet into the tip required a shore-hardness of 90, about twice the shore-hardness of the rest of the electrode. This was necessary to prevent the magnet from rotating inside the tip during experiments. The standard silicone rubber was not strong enough to securely fix the magnet at the tips of E1 and E2 when torque was applied by the

magnetic field.

Two separate experiment sets are conducted in the study described herein. The first set compares each reference electrode against its modified model, with all electrodes inserted through the simulated cochleostomy. The insertion speed for all trials is set to 0.2 mm/sec. Although this is slower than manual insertions measured in the clinic [43], recent work strongly suggests that slower insertions tend to have decreased electrode insertion forces [43] with less variability [22] and are associated with better hearing preservation [44, 45]. For this experiment set, magnetic guidance is not used since the goal is to determine if modifying the electrode tip to include a magnet changes the insertion forces.

The second set of experiments implements magnetically guided insertions of the electrodes with magnets using a supervised automated procedure comprising three distinct steps in a sequence that is repeated until the insertion is completed: (1) increment the insertion depth by 0.5 mm, (2) rotate the EM to a depth-specific value stored in a look-up table, and (3) translate the EM relative to the phantom using a depth-specific value stored in a look-up table. Again, the insertion depth corresponds to the motion of the insertion stage and not to the electrode tip. To obtain the values stored in the two look-up tables described above, prior to conducting the experiments, the motion of the EM was coordinated to the electrode insertion as follows. Each electrode was inserted into the phantom at 0.5 mm increments. After each increment, a camera was used to visualize the lumen direction at the current location of the electrode tip, and the EM was rotated such that its dipole was orthogonal to the lumen direction, which would cause its applied field to lead the dipole of the electrode's tip magnet by 90 degrees. Then, the distance between the EM and the phantom was adjusted until the electrode tip was centered in the channel. This procedure was repeated for each electrode tested to create electrode-specific look-up tables. In addition, to simulate supervisory control of the surgeon throughout the three-step insertion sequence (i.e., the system awaiting surgeon consent between steps in the sequence), the actuators were kept still for one full second between each step. For the control group, we insert the electrodes with magnets in 0.5 mm increments and with the EM positioned far away from the electrodes.

Prior to each trial conducted in all experiments described above, the phantom is filled with saline solution [40] and a small amount of silicone lubricant [12, 46] is applied to the

electrode tip.

4.4 Results

All angular insertion depth measurements herein locate the tip with respect to the round window. All linear depth measurements herein represent movement of the insertion stage. At 0 mm linear insertion depth, the insertion stage positions the most apical electrode band just outside the scala-tympani channel.

All force values shown in the plots of Figure 4.4 and Figure 4.5 are the magnitude of the averaged sensor values for every 0.5 mm of electrode insertion (to filter sensor noise). The number of trials conducted for each electrode tested is indicated in the legend. *t*-test analysis was computed on the difference of means and provided below the insertion forces with markers indicating where along the insertion the null hypothesis can be rejected with 95% confidence. Rejecting the null hypothesis would imply that there is a statistically meaningful difference between the two insertions compared. In other words, each marker tells us where along the insertion we can be 95% confident that the measured difference is not due to randomness. The 95% confidence intervals are displayed as shaded regions.

The results of Experiment 1 are compiled in Figure 4.4. Electrodes E2 and E3 have nearly identical insertion behavior as their corresponding reference electrode R2. The absolute difference between the measured insertion forces never exceeded 1.5 mN. There is a statistically meaningful difference near 8-9 mm (where the electrode tip first contacts the LW) although the measured effect ($\Delta \|\mathbf{F}\|$) is minimal at less than 1 mN. For E3, there are two additional regions from 10–12 mm and at 14 mm where statistically meaningful difference occurs, though the difference is also less than 1 mN.

Electrode E1, however, performs differently than reference R1 beyond an insertion depth of 15 mm, which is about 300°. Video capture shows that the tip of E1 tends to stick-slip in this region, whereas R1 does not. This phenomenon increases the insertion force by about 5 mN. There is also a statistically meaningful difference near 10-11 mm but with minimal effect (less than 1 mN).

The results of Experiment 2 are compiled in Figure 4.5. The top row provides the magnetic field generated at the phantom to accomplish the guided insertions of the electrodes with magnets. *t*-test results show that beyond 8 mm insertion depth, magnetically guiding

the electrodes through the channel significantly reduced insertion forces for all electrodes tested. The greatest improvements were achieved with E2, with negligible forces up to approximately 17 mm insertion depth and percent reduction at certain locations thereafter greater than 50%, followed by the results for E3. However, we note that the maximum required magnetic field applied to E2 was more than double that applied to E3, due to the larger magnetic dipole embedded in the tip of E3. Only modest reductions in insertion forces were achieved with E1.

To visualize a typical guided insertion, image snapshots of E2 are shown in Figure 4.5-B. With this method, the tip is able to reach approximately 180° before the apical section of the electrode contacts the LW. Beyond this location, the applied torque is only able to pull the tip away from the LW while the remainder of the electrode slides along the LW. However, recall that, due to the mechanical properties of the electrode, we know that the pressure is reduced along the entire length of the electrode due to the torque at the tip; the net effect is observed in the reduced insertion force.

We examine the manner in which the guided electrode (E2) contacts the LW (see Figure 4.6 containing a sequence of images demonstrating the initial contact). Two things should be noted. First, the electrode tip never directly contacts the LW through the first turn (120°–210°). Second, the initial contact between the electrode and the LW is no longer concentrated at the tip but is distributed over the apical section of the electrode.

We observe some unique responses for electrodes E1 and E3 under bending from the EM. The tip of E3, due to its added length to accommodate a second magnet, along with its hinge-like behavior, limits the amount of torque that can be applied because of the increased possibility that the tip will touch the medial wall (Figure 4.7-1 and Figure 4.7-2). This becomes more challenging as the channel becomes smaller for deeper insertions or where the channel narrows suddenly (Figure 4.7-3). Note that, in our experimental protocol, we chose to position the EM so as to center the tip magnet in the scala-tympani channel, but an alternate method could have been to position the EM to just slightly pull the tip away from the LW, which would have mitigated this concern; however, it is unclear what effect this change in protocol would have had on insertion forces.

Near 180°, the torque applied to the tip of E1 (Figure 4.7-4) is not sufficient to pull the tip into the center of the channel after the electrode body begins to slide along the LW.

This indicates that a stronger magnetic field was needed here and beyond what could be delivered by our apparatus. This is not true beyond this point (Figure 4.7-5 and Figure 4.7-6), though it is partly due to the geometry of the channel.

4.5 Discussion

Assessments are primarily based on measured insertion forces with *t*-test analysis of the difference of means to confirm statistical significance. It is important to note that we are not making general conclusions about the population of electrodes since the number of electrodes tested is very limited. Rather we are making an assessment about the insertion itself. For example, regarding the first set of experiments, this would mean that if the same insertions were conducted again comparing R2 and E2, we would be 95% confident that a real insertion difference, although small, would occur between 8-9 mm of insertion depth. Similarly, if experiment 2 was redone for E2, we would be 95% confident that beyond 8 mm of insertion depth, magnetic guidance will begin to reduce insertion forces dramatically.

The effect of modifying the electrode tip to accommodate a small magnet is electrode dependent. The alteration of R2 does not significantly affect its insertion characteristics. However, altering R1 changes it behavior near 300°. One possible reason is that the tip of R1 is tapered, and by adding a magnet, the tip became rounded (Figure 4.3). We note that our measurements of R1 and R2 are comparable to measurements obtained by other groups using these electrodes [12, 47].

Guiding the electrodes through the channel reduced insertion forces for all electrodes tested, although the improvement for E1 was minimal. Results achieved through magnetically guiding E2 are comparable to the best results achieved with perimodiolar electrodes inserted with the AOS technique [23, 25]. The results with E3 showed good overall force reduction and also come with the benefit of requiring a smaller external magnetic source.

Even though E1 required more bending torque at 180° than could be delivered using our EM, this is not sufficient to explain the minimal improvement measured. A stronger magnetic field would have only helped for a short part of the insertion since sufficient bending torque was applied past this region (Figure 4.7-5 and Figure 4.7-6). We are left to conclude that the MED-EL Flex20 electrode, as currently designed, may not be a good candidate for our magnetic-guidance concept.

Based on the magnetic-field profile for all electrodes tested, the point at which the maximum field is needed is at approximately 180°. Beyond this location, the necessary field strength changes based on the flexibility of the electrode tip and the geometry of the channel.

One important result is that direct tip contact with the LW is eliminated throughout the insertion. Even at the location where the electrode body first contacts the LW, it is likely to be less traumatic because it is distributed over a longer length than is typical. Two benefits arise from this. First, many studies have noted that a large percentage of basilar-membrane perforations have occurred at the first turn of the LW [1, 2, 26, 48, 49]. In such cases, the tip is often deflected by the LW out-of-plane into the basilar membrane [49]. Second, the likelihood of incomplete insertions increases dramatically if tip contact with the spiral ligament is severe enough [50]. By eliminating direct tip contact with the LW throughout the entirety of the insertion, both of these incidences are likely to be reduced.

There is an additional intangible benefit to magnetic guidance that is not quantified in our experiments. Although we are primarily setting the applied-field direction to generate a magnetic torque to pull the tip of the electrode away from the LW, because the field vector is always set in the bending plane orthogonal to the modiolar axis, any angular deviation of the tip from this plane is met with a torque proportional to the deviation that will try to pull the tip back onto this plane. The overall effect would be akin to a magnetic spring hindering the tip deviating toward the basilar membrane. The benefit of this effect will be quantified in subsequent work.

All experiments were conducted through a cochleostomy proxy. With the ongoing interest in atraumatic insertions, especially where hearing preservation is a priority, many clinicians are opting for electrode insertion through the round window. Steering electrodes that are initially inserted through the round window poses a unique challenge in that the curvature of the cochlear hook is opposite that of the cochlear lumen. We believe that the technique described herein for steering the electrode is perfectly suited for this challenge. This is the motivation for Part II of this series [51].

4.6 Conclusion

Magnetically guiding lateral-wall electrodes during insertions can reduce measured forces by as much as 50% with certain electrodes and can eliminate direct contact between the electrode tip and the lateral wall in its entirety. This is achievable through a minor modification to existing lateral-wall electrodes, maintaining their beneficial flexibility over stylet-based perimodiolar electrodes. Specifically, we found that insertions of the MED-EL Flex24 electrode can benefit significantly from magnetic guidance, whereas the improvements with the MED-EL Flex20 electrode are less pronounced.

4.7 Acknowledgements

The authors gratefully acknowledge support from Anandhan Dhanasingh of MED-EL for fabricating the electrodes used in these experiments. Research reported in this chapter was supported by the National Institute on Deafness and Other Communication Disorders of the National Institutes of Health under Award Number R01DC013168. The content is solely the responsibility of the authors and does not necessarily represent the official views of the National Institutes of Health.

4.8 References

[1] P. Wardrop, D. Whinney, S. J. Rebscher, J. T. Roland, Jr., W. Luxford, and P. A. Leake, "A temporal bone study of insertion trauma and intracochlear position of cochlear implant electrodes. I: comparison of Nucleus banded and Nucleus Contour electrodes," *Hear. Res.*, vol. 203, no. 1-2, pp. 54–67, 2005.

[2] F. G. Zeng, S. Rebscher, W. Harrison, X. Sun, and H. Feng, "Cochlear implants: System design, integration, and evaluation," *IEEE Reviews in Biomed. Eng.*, vol. 1, pp. 115–142, 2008.

[3] G. B. Wanna, J. H. Noble, R. H. Gifford, M. S. Dietrich, A. D. Sweeney, D. Zhang, B. M. Dawant, A. Rivas, and R. F. Labadie, "Impact of intrascalar electrode location, electrode type, and angular insertion depth on residual hearing in cochlear implant patients: Preliminary results.," *Otol. Neurotol.*, vol. 36, no. 8, pp. 1343–1348, Sep 2015.

[4] I. A. Bruce, M. Felton, M. Lockley, C. Melling, S. K. Lloyd, S. R. Freeman, and K. M. J. Green, "Hearing preservation cochlear implantation in adolescents," *Otol. Neurotol.*, Aug 2014.

[5] M. L. Carlson, C. L. W. Driscoll, R. H. Gifford, G. J. Service, N. M. Tombers, B. J. Hughes-Borst, B. A. Neff, and C. W. Beatty, "Implications of minimizing trauma during conventional cochlear implantation," *Otol. Neurotol.*, vol. 32, no. 6, pp. 962–968, 2011.

[6] A. D'Elia, R. Bartoli, F. Giagnotti, and N. Quaranta, "The role of hearing preservation on electrical thresholds and speech performances in cochlear implantation," *Otol. Neurotol.*, vol. 33, no. 3, pp. 343–347, 2012.

[7] M. K. Cosetti, D. R. Friedmann, B. Z. Zhu, S. E. Heman-Ackah, Y. Fang, R. G. Keller, W. H. Shapiro, J. T. Roland, Jr, and S. B. Waltzman, "The effects of residual hearing in traditional cochlear implant candidates after implantation with a conventional electrode," *Otol. Neurotol.*, vol. 34, no. 3, pp. 516–21, Apr 2013.

[8] W. Gstoettner, S. Helbig, C. Settevendemie, U. Baumann, J. Wagenblast, and C. Arnoldner, "A new electrode for residual hearing preservation in cochlear implantation: first clinical results," *Acta oto-laryngologica*, vol. 129, no. 4, pp. 372–379, 2009.

[9] C. Jolly, C. Garnham, H. Mirzadeh, E. Truy, A. Martini, J. Kiefer, and S. Braun, "Electrode features for hearing preservation and drug delivery strategies," *Adv. Otorhinolaryngol.*, vol. 67, pp. 28–42, 2010.

[10] H. Skarzynski, A. Lorens, M. Matusiak, M. Porowski, P. H. Skarzynski, and C. J. James, "Partial deafness treatment with the nucleus straight research array cochlear implant," *Audiol. Neurotol.*, vol. 17, no. 2, pp. 82–91, 2012.

[11] H. Skarzynski and R. Podskarbi-Fayette, "A new cochlear implant electrode design for preservation of residual hearing: a temporal bone study," *Acta Otolaryngol.*, vol. 130, no. 4, pp. 435–42, Apr 2010.

[12] O. Adunka, J. Kiefer, M. H. Unkelbach, T. Lehnert, and W. Gstoettner, "Development and evaluation of an improved cochlear implant electrode design for electric acoustic stimulation," *Laryngoscope*, vol. 114, no. 7, pp. 1237–41, Jul 2004.

[13] B. J. Gantz, C. Turner, K. E. Gfeller, and M. W. Lowder, "Preservation of hearing in cochlear implant surgery: advantages of combined electrical and acoustical speech processing," *Laryngoscope*, vol. 115, no. 5, pp. 796–802, May 2005.

[14] F. Hassepass, A. Aschendorff, S. Bulla, S. Arndt, W. Maier, R. Laszig, and R. Beck, "Radiologic results and hearing preservation with a straight narrow electrode via round window versus cochleostomy approach at initial activation.," *Otol. Neurotol.*, vol. 36, no. 6, pp. 993–1000, Jul 2015.

[15] T. Lenarz, T. Stöver, A. Buechner, A. Lesinski-Schiedat, J. Patrick, and J. Pesch, "Hearing conservation surgery using the hybrid-l electrode. results from the first clinical trial at the medical university of hannover.," *Audiol. Neurotol.*, vol. 14 Suppl 1, pp. 22–31, 2009.

[16] T. Lenarz, T. Stover, A. Buechner, G. Paasche, R. Briggs, F. Risi, J. Pesch, and R. Battmer, "Temporal bone results and hearing preservation with a new straight electrode," *Audiol. Neurotol.*, vol. 11 Suppl 1, pp. 34–41, 2006.

[17] P. Mukherjee, H. Uzun-Coruhlu, C. C. Wong, I. S. Curthoys, A. S. Jones, and W. P. R. Gibson, "Assessment of intracochlear trauma caused by the insertion of a new straight research array," *Cochlear Implants Int.*, vol. 13, no. 3, pp. 156–62, Aug 2012.

[18] Y. Nguyen, I. Mosnier, S. Borel, E. Ambert-Dahan, D. Bouccara, A. Bozorg-Grayeli, E. Ferrary, and O. Sterkers, "Evolution of electrode array diameter for hearing preservation in cochlear implantation," *Acta oto-laryngologica*, vol. 133, no. 2, pp. 116–122, 2013.

[19] K. M. Van Abel, C. C. Dunn, D. P. Sladen, J. J. Oleson, C. W. Beatty, B. A. Neff, M. Hansen, B. J. Gantz, and C. L W. Driscoll, "Hearing preservation among patients undergoing cochlear implantation.," *Otol. Neurotol.*, vol. 36, no. 3, pp. 416–421, Mar 2015.

[20] K. S. Min, S. H. Oh, M. Park, J. Jeong, and S. J. Kim, "A polymer-based multichannel cochlear electrode array," *Otol. Neurotol.*, vol. 35, no. 7, pp. 1179–86, Aug 2014.

[21] A. Radeloff, M. H. Unkelbach, M. G. Mack, C. Settevendemie, S. Helbig, J. Mueller, R. Hagen, and R. Mlynski, "A coated electrode carrier for cochlear implantation reduces insertion forces," *Laryngoscope*, vol. 119, no. 5, pp. 959–63, May 2009.

[22] O. Majdani, D. Schurzig, A. Hussong, T. Rau, J. Wittkopf, T. Lenarz, and R. F. Labadie, "Force measurement of insertion of cochlear implant electrode arrays in vitro: comparison of surgeon to automated insertion tool," *Acta Otolaryngol.*, vol. 130, no. 1, pp. 31–36, 2010.

[23] J. T. Roland, Jr., "A model for cochlear implant electrode insertion and force evaluation: Results with a new electrode design and insertion technique," *Laryngoscope*, vol. 115, no. 8, pp. 1325–1339, 2005.

[24] D. Schurzig, R. J Webster, III, M. S. Dietrich, and R. F. Labadie, "Force of cochlear implant electrode insertion performed by a robotic insertion tool: Comparison of traditional versus advance off–stylet techniques," *Otol. Neurotol.*, vol. 31, no. 8, pp. 1207–1210, 2010.

[25] C. A. Todd, F. Naghdy, and M. J. Svehla, "Force application during cochlear implant insertion: An analysis for improvement of surgeon technique," *IEEE Trans. Biomed. Eng.*, vol. 54, no. 7, pp. 1247–1255, 2007.

[26] E. Boyer, A. Karkas, A. Attye, V. Lefournier, B. Escude, and S. Schmerber, "Scalar localization by cone-beam computed tomography of cochlear implant carriers: a comparative study between straight and periomodiolar precurved electrode arrays.," *Otol. Neurotol.*, vol. 36, no. 3, pp. 422–429, Mar 2015.

[27] S. J. Rebscher, A. Hetherington, B. Bonham, P. Wardrop, D. Whinney, and P. A. Leake, "Considerations for design of future cochlear implant electrode arrays: Electrode array stiffness, size, and depth of insertion," *JRRD*, vol. 45, no. 5, pp. 731–747, 2008.

[28] A. Coordes, A. Ernst, G. Brademann, and I. Todt, "Round window membrane insertion with perimodiolar cochlear implant electrodes," *Otol. Neurotol.*, vol. 34, no. 6, pp. 1027–1032, 2013.

[29] R. J. S. Briggs, M. Tykocinski, R. Lazsig, A. Aschendorff, T. Lenarz, T. Stöver, B. Fraysse, M. Marx, Jr. J. T. Roland, P. S. Roland, C. G. Wright, B. J. Gantz, J. F. Patrick, and F. Risi, "Development and evaluation of the modiolar research array–multi-centre collaborative study in human temporal bones," *Cochlear Implants Int.*, vol. 12, no. 3, pp. 129–139, 2011.

[30] T. S. Rau, A. Hussong, M. Leinung, T. Lenarz, and O. Majdani, "Automated insertion of preformed cochlear implant electrodes: evaluation of curling behaviour and insertion forces on an artificial cochlear model," *Int. J. CARS*, vol. 5, no. 2, pp. 173–81, Mar 2010.

[31] B. Y. Arcand, P. T. Bhatti, N. V. Butala, J. Wang, C. R. Friedrich, and K. D. Wise, "Active positioning device for a perimodiolar cochlear electrode array," *Microsys.Tech.*, vol. 10, pp. 478–483, 2004.

[32] B. Chen, H. N. Kha, and G. M. Clark, "Development of a steerable cochlear implant electrode array," in *IFMBE Int. Conf. Biomed. Eng.*, 2007, vol. 15, pp. 607–610.

[33] H. Mirzadeh and F. Abbasi, "Segmented detachable structure of cochlear–implant electrodes for close-hugging engagement with the modiolus," *J. Biomed. Mater. Res. B Appl. Biomater.*, vol. 68B, no. 2, pp. 191–198, 2004.

[34] J. Wu, L. Yan, H. Xu, W. C. Tang, and F. Zeng, "A curvature-controlled 3D microelectrode array for cochlear implants," in *IEEE Int. Conf. Solid St. Sens. Act. Microsys.*, 2005, vol. 2, pp. 1636–1639.

[35] J. Zhang, W. Wei, J. Ding, J. T. Roland, Jr., S. Manolidis, and N. Simaan, "Inroads toward robot-assisted cochlear implant surgery using steerable electrode arrays," *Otol. Neurotol.*, vol. 31, no. 8, pp. 1199–1206, 2010.

[36] J. R. Clark, L. Leon, F. M. Warren, and J. J. Abbott, "Magnetic guidance of cochlear implants: Proof-of-concept and initial feasibility study," *J. Med. Devices*, vol. 6, no. 3, pp. 035002, 2012.

[37] J. H. Noble, R. F. Labadie, O. Majdani, and B. M. Dawant, "Automatic segmentation of intracochlear anatomy in conventional CT," *IEEE Trans. Biomed. Eng.*, vol. 58, no. 9, pp. 2625–32, Sep 2011.

[38] K. Hüttenbrink, T. Zahnert, C. Jolly, and G. Hofmann, "Movements of cochlear implant electrodes inside the cochlea during insertion: an x-ray microscopy study," *Otol. Neurotol.*, vol. 23, no. 2, pp. 187–91, Mar 2002.

[39] P. C. Pearlman, M. H. W. van Deurzen, J. P. W. Pluim, and W. Grolman, "Coregistration of preoperative computed tomography and intraoperative three-dimensional rotational x-ray images for cochlear implant surgical evaluation," *Otol. Neurotol.*, Jul 2014.

[40] Y. Nguyen, M. Miroir, G. Kazmitcheff, J. Sutter, M. Bensidhoum, E. Ferrary, O. Sterkers, and A. Bozorg Grayeli, "Cochlear implant insertion forces in microdissected human cochlea to evaluate a prototype array," *Audiol. Neurotol.*, vol. 17, no. 5, pp. 290–8, 2012.

[41] L. Leon, M. S. Cavilla, M. B. Doran, F. M. Warren, and J. J. Abbott, "Scala-tympani phantom with cochleostomy and round-window openings for cochlear-implant insertion experiments," *J. Med. Devices*, vol. 8, no. 4, pp. 041010, 2014.

[42] B. M. Verbist, M. W. Skinner, L. T. Cohen, P. A. Leake, C. James, C. Boëx, T. A. Holden, C. C. Finley, P. S. Roland, J. T. Roland, Jr, M. Haller, J. F. Patrick, C. N. Jolly, M. A.

Faltys, J. J. Briaire, and J. H. M. Frijns, "Consensus panel on a cochlear coordinate system applicable in histologic, physiologic, and radiologic studies of the human cochlea," *Otol. Neurotol.*, vol. 31, no. 5, pp. 722–730, 2010.

[43] G. Kontorinis, T. Lenarz, T. Stöver, and G. Paasche, "Impact of the insertion speed of cochlear implant electrodes on the insertion forces," *Otol. Neurotol.*, vol. 32, no. 4, pp. 565–570, 2011.

[44] G. P. Rajan, G. Kontorinis, and J. Kuthubutheen, "The effects of insertion speed on inner ear function during cochlear implantation: a comparison study," *Audiol. Neurotol.*, vol. 18, no. 1, pp. 17–22, 2013.

[45] P. L. Santa Maria, M. B. Gluth, Y. Yuan, M. D. Atlas, and N. H. Blevins, "Hearing preservation surgery for cochlear implantation: a meta-analysis," *Otol. Neurotol.*, vol. 35, no. 10, pp. e256–69, Dec 2014.

[46] G. Kontorinis, G. Paasche, T. Lenarz, and T. Stöver, "The effect of different lubricants on cochlear implant electrode insertion forces," *Otol. Neurotol.*, vol. 32, no. 7, pp. 1050–6, Sep 2011.

[47] S. Helbig, C. Settevendemie, M. Mack, U. Baumann, M. Helbig, and T. Stöver, "Evaluation of an electrode prototype for atraumatic cochlear implantation in hearing preservation candidates: preliminary results from a temporal bone study," *Otol. Neurotol.*, vol. 32, no. 3, pp. 419–423, 2011.

[48] A. Aschendorff, R. Kubalek, B. Turowski, F. Zanella, A. Hochmuth, M. Schumacher, T. Klenzner, and R. Laszig, "Quality control after cochlear implant surgery by means of rotational tomography," *Otol. Neurotol.*, vol. 26, no. 1, pp. 34–37, 2005.

[49] M. L. Carlson, C. L.W. Driscoll, R. H. Gifford, and S. O. McMenomey, "Cochlear implantation: current and future device options," *Otolaryngol. Clin. N. America*, vol. 45, no. 1, pp. 221–248, 2012.

[50] J. Lee, J. B. Nadol, Jr, and D. K. Eddington, "Factors associated with incomplete insertion of electrodes in cochlear implant surgery: a histopathologic study.," *Audiol. Neurotol.*, vol. 16, no. 2, pp. 69–81, 2011.

[51] L. Leon, F. M. Warren, and J. J. Abbott, "An in-vitro insertion-force study of magnetically guided, lateral-wall, cochlear-implant electrodes, part I: Via cochleostomy," *Otol. Neurotol.*, (under review).

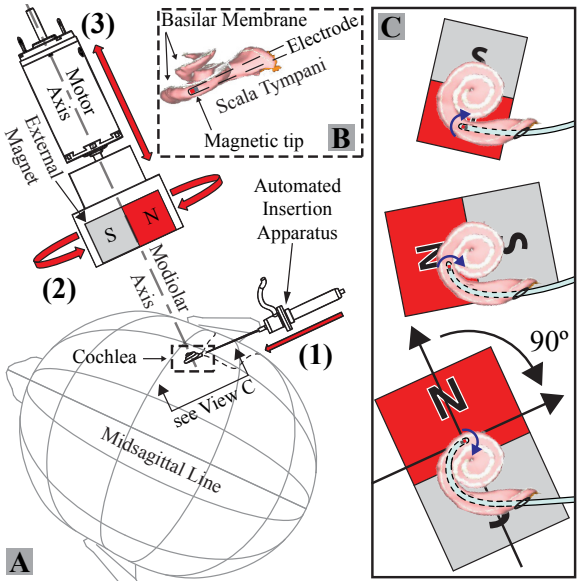

Figure 4.1. A. Magnetically guided insertions are achieved using only three controlled degrees-of-freedom: (1) insertion of an electrode with a magnetic tip, (2) rotation of the external magnet about the modiolar axis, and (3) translation of the external magnet along the modiolar axis. B. Close-up view of the scala tympani with the basilar membrane labeled (and shaded in white). C. The external magnet applies torque (shown as blue curved arrows) to the electrode's magnetic tip. To minimize any attractive force on the tip toward the external magnet, the angle between the magnetic orientations (represented by black arrows in the lower-right image pointing from each magnet's south pole to north pole) is maintained at approximately 90°.

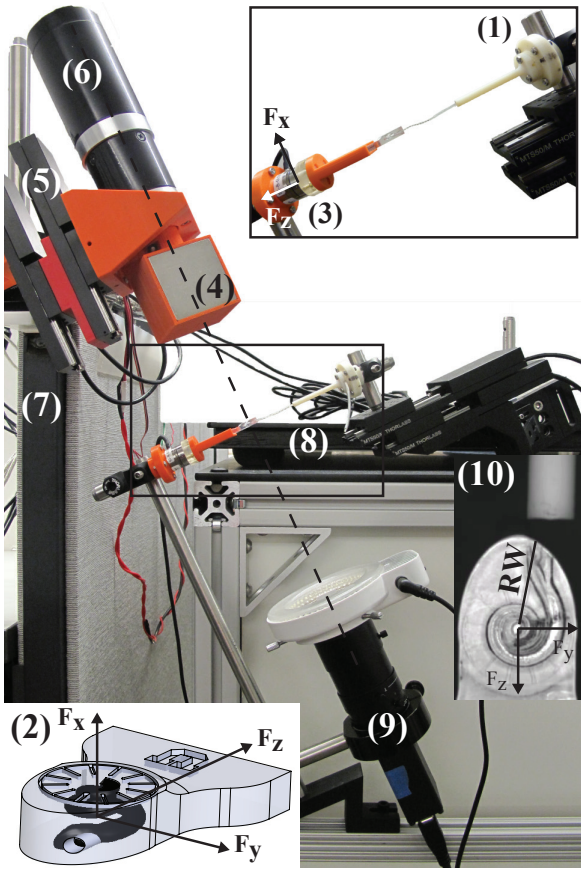

Figure 4.2. Experimental setup, with explanations of the various components in the text.

	Reference	1 magnet	2 magnets	Length
$Flex^{20}$	R1	E1*	---	20 mm
$Flex^{24}$	R2	E2*	E3	24 mm

* with stronger silicone rubber at the tip

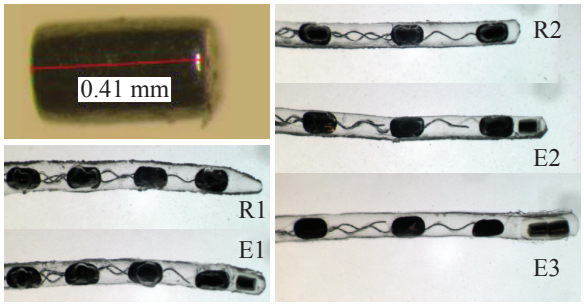

Figure 4.3. Electrodes used in this study.

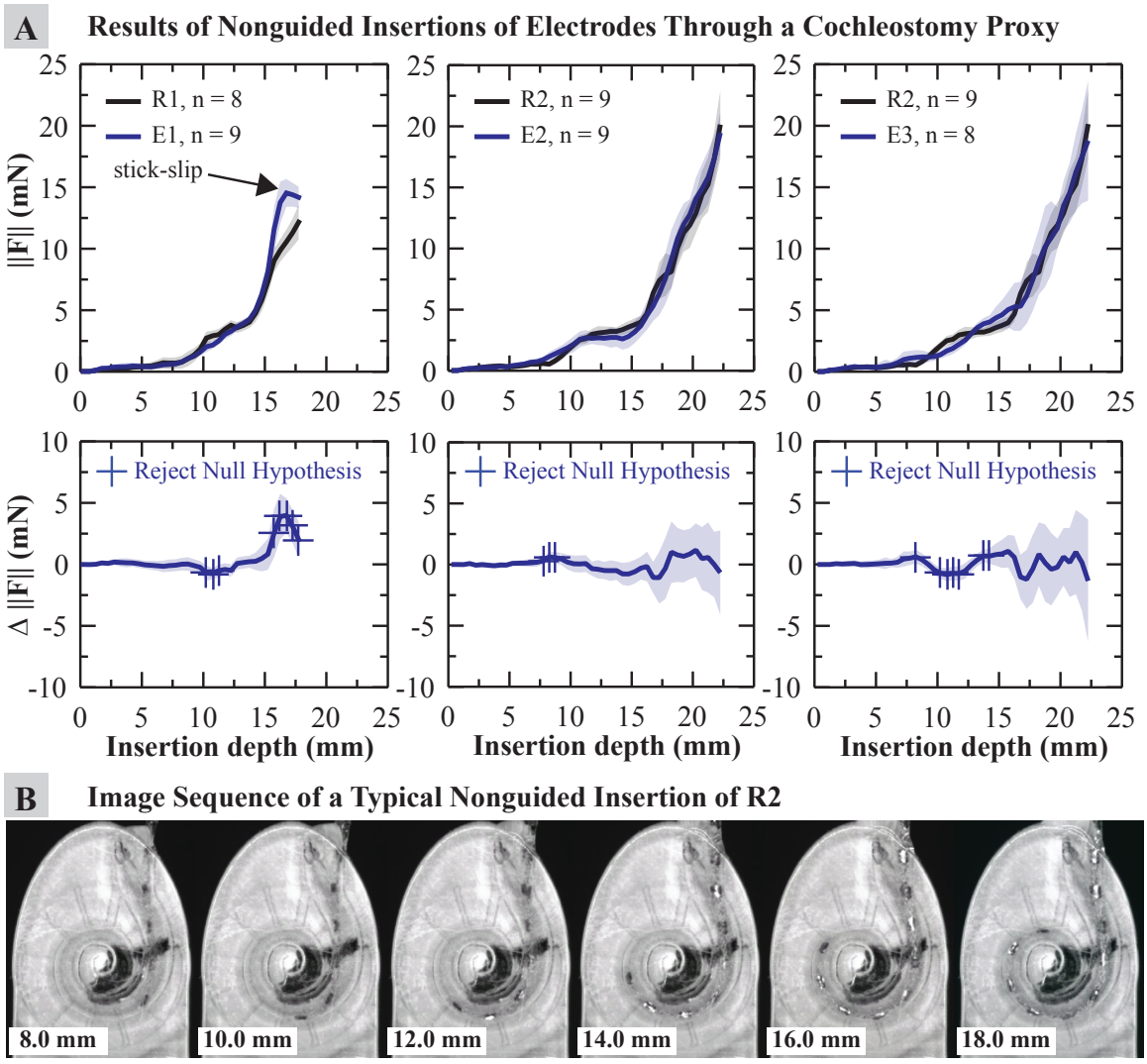

Figure 4.4. A. (Top) Results of experiment 1 compare insertion forces of electrodes inserted at a constant speed of 0.2 mm/s, without the use of magnetic guidance. 95% confidence intervals are shown as shaded regions. Force values shown on the plots are the magnitude $\|\mathbf{F}\| = \sqrt{F_x^2 + F_y^2 + F_z^2}$ of the averaged sensor values for every 0.5 mm of electrode insertion (to reduce sensor noise). The number of trials conducted for the electrode tested is indicated in the legend. (Bottom) *t* tests compute the difference of means with markers that indicate where along the insertion the null-hypothesis can be rejected with 95% confidence. B. A series of image snapshots depicting a typical insertion of a lateral-wall electrode. The linear insertion depth at which the image is taken is labeled on the lower-left of each image.

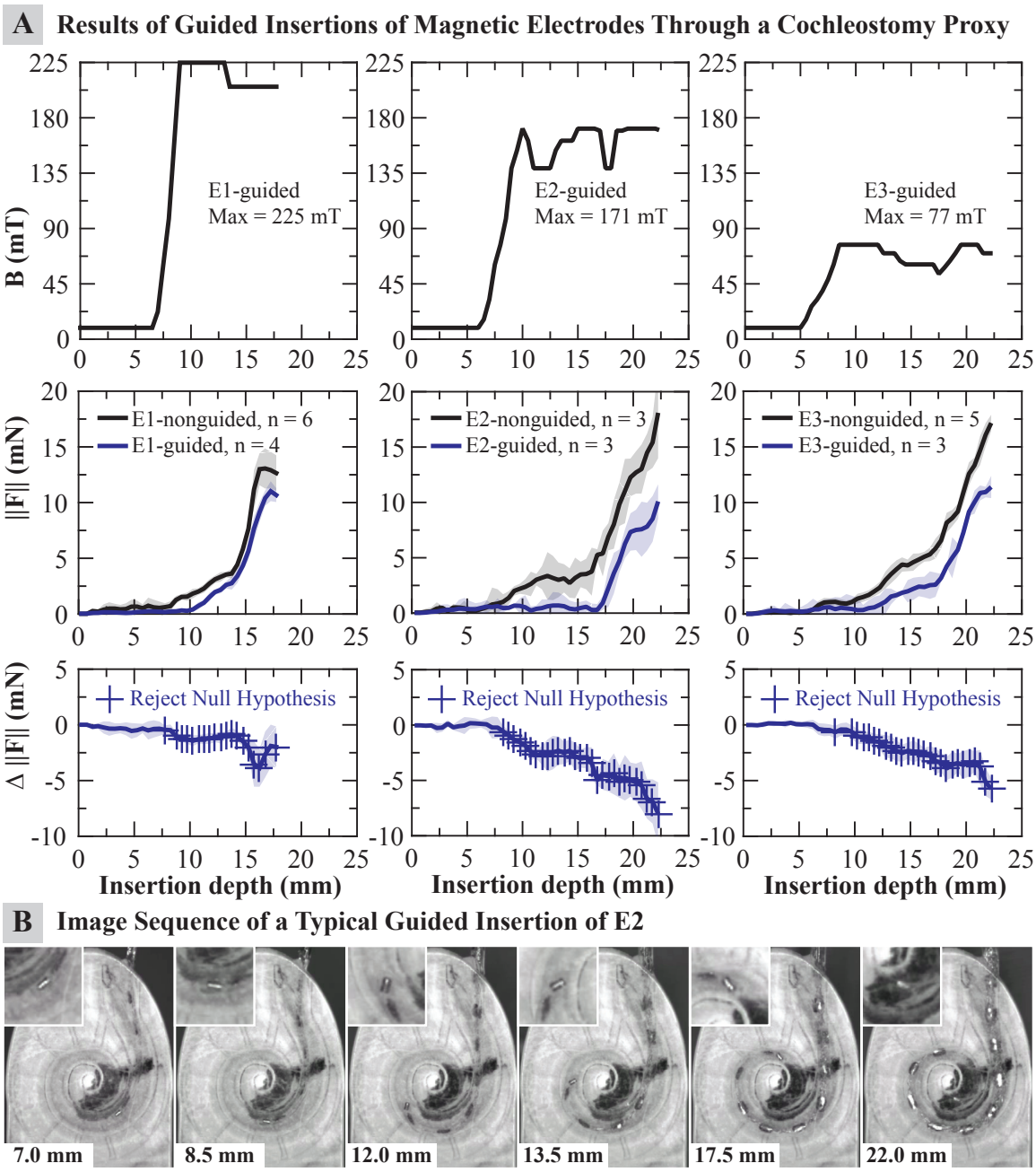

Figure 4.5. A. Results of experiment 2 compare nonguided and magnetically guided insertions of the electrodes with magnets shown in Figure 4.3. The top row shows the applied magnetic field used to achieve the guided insertions. Measured insertion forces (with 95% confidence levels shaded) and *t*-test analysis are placed below the magnetic field profiles. B. Images chosen to represent a typical guided insertion of an electrode with magnet (E2 in this example) wherein the tip is navigated through the first turn.

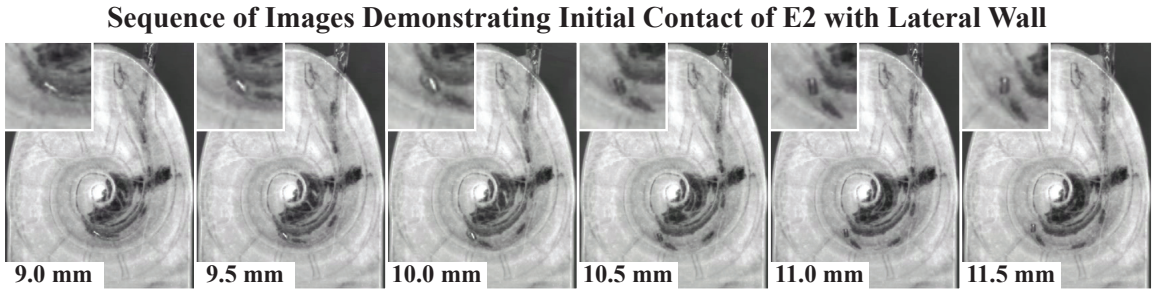

Figure 4.6. Images showing the nature of the contact between the magnetically guided electrode (E2) and the lateral wall of the first turn. Near 180° from the round window, applying torque to the tip can no longer pull the body of the electrode off the lateral wall even though the tip never directly contacts the lateral wall.

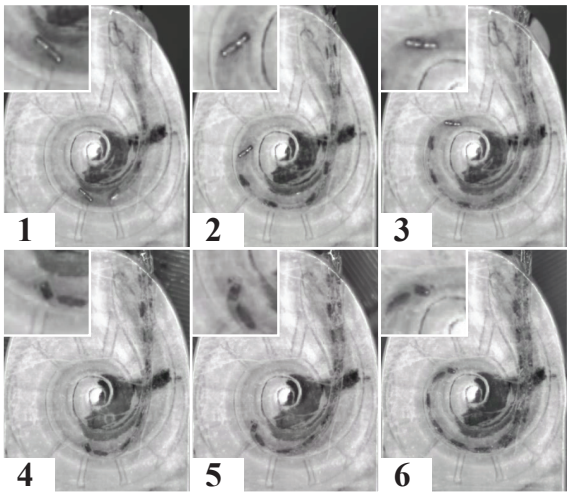

Figure 4.7. Images comparing the tip behavior of electrodes E3 (top row) and E1 (bottom row) under magnetic guidance at several locations.

CHAPTER 5

AN IN-VITRO INSERTION-FORCE STUDY OF MAGNETICALLY GUIDED, LATERAL-WALL, COCHLEAR-IMPLANT ELECTRODES, PART II: VIA THE ROUND WINDOW

Insertion experiments using clinical, lateral-wall-type electrodes through a simulated round-window opening demonstrate that a statistically significant ($p < 0.05$) reduction in insertion forces can be achieved using magnetic guidance. Guiding the electrode-array tip through the cochlear hook and the basal turn, in the same insertion, is demonstrated for the first time. All existing methods to guide the electrode array can only be accomplished through the basal turn.

5.1 Abstract

Insertion forces can be reduced by magnetically guiding the tip of lateral-wall, cochlear-implant electrodes during insertion via the round-window. Alteration of the electrode tip to accommodate a tiny magnet is required but does not change the insertion characteristic of the electrode.

To date, steerable electrodes are designed to curve in the direction of the basal turn. This is not ideal for round-window insertions, as the cochlear hook's curvature is in the opposite direction. We have experimented with lateral-wall electrodes that have been modified to include magnets at their tips. By applying magnetic torque to the tip, in opposite directions, an electrode can be navigated through the cochlear hook and the basal turn.

Automated insertions of electrodes with magnets are conducted into a scala-tympani phantom with a round-window proxy. A force sensor is attached to the phantom to provide the measurements needed to evaluate our hypotheses. An external magnet is

coordinated to the insertion of the electrode and directs the electrode tip down the lumen through the entire insertion.

t-test results indicate that magnetic guidance does reduce insertion forces by as much as 50% with certain electrode models. Direct tip contact through the cochlear hook and the basal turn is completely eliminated for all electrodes with magnets. Stick-slip behavior of the electrode does seem to differ if the tip shape is altered to accommodate the magnet.

Magnetic guidance can eliminate tip contact with the medial walls through the cochlear hook and the lateral walls of the basal turn. Significant reduction of insertion force can be achieved with certain electrode models.

5.2 Introduction

In Part 1 of this study, we described a method to magnetically guide the tip of a robotically inserted lateral-wall (LW) cochlear-implant electrode to reduce insertion forces during insertion via cochleostomy [1]. In this second part of the study, we describe how the method can be modified for insertions via the round window (RW). With increased focus on hearing preservation in cochlear implantation, especially given the benefits of combined electric-acoustic stimulation, methods to minimize intracochlear damage have become a priority in electrode placements [2,3]. This has renewed interest in using the RW for electrode insertions [4–7] with the recent literature favoring the RW over cochleostomies when hearing preservation is the primary consideration [8, 9].

Prior to the development of more flexible electrodes, cochleostomies were favored because the stiffer multichannel electrodes required a straight route into the lumen to avoid the cochlear hook (CH) region [10]. In fact, the CH is problematic enough that several studies have examined the appropriate initial insertion vector needed for atraumatic results [7, 11–15]. The need to evaluate this initial vector is due to the proximity of the basilar membrane (BM) and osseous spiral lamina (OSL) to the RW opening [16], along with the challenge of guiding the electrode tip satisfactorily down the lumen without first impacting these particular structures. For many, cochleostomies are still preferred because the electrode insertion vector can be aligned with the lumen of the scala tympani (ST) making for easier insertions [9, 17]. However, this is becoming less of a concern with the recent trend toward more flexible and thinner LW electrodes to reduce the effects of impact

with intracochlear structures.

Although there are still many proponents of using cochleostomies [17], even when hearing preservation is desired [9], LW electrodes are now routinely inserted through the RW, the primary benefit of which is direct entry into the ST, at the outset, with minimal drilling-related trauma [18]. This is guaranteed because the ST terminates at the RW. In contrast, accurate placement of cochleostomies is mandatory to ensure initial ST insertions. Unfortunately, it has been shown that there is a 20% probability that the cochleostomy will be sited incorrectly by practicing surgeons, leading to potential electrode misplacement into the scala vestibuli from the very outset [19]. Even in cases where soft-surgery techniques are employed, cochleostomy sites may be different than originally intended [20]. Also, evidence from clinical practice indicates that using the RW for insertions produces a high percentage of complete ST placement [21], and electrodes that are placed entirely within the ST tend to produce better hearing outcomes [3].

Recent evidence suggests that, unlike LW electrodes, perimodiolar electrodes may not be very safe for RW insertions [22–24]. A problem is that the stylet, which is needed to insert these devices, increases the overall thickness while reducing the flexibility, both of which are not suited for RW approaches and may make it more difficult for the electrode to pass through the CH [20, 24]. An advantage to perimodiolar electrodes is that, when inserted properly, they curl away from the LW of the first turn, reducing contact with intracochlear structures in the process. With this in mind, we present a method to steer a LW electrode that is inserted through the RW. In Part 1 of this study, which examined magnetically guided insertions through a simulated cochleostomy, the goal was to apply enough magnetic torque to bend the tip away from the LW of the cochlea's first turn. In this second part of the study, since the insertion is done through a simulated RW opening, the electrode tip must first be bent away from the medial wall (MW) of the CH before later being bent away from the LW of the cochlea's first turn (Figure 5.1). To our knowledge, this has never been attempted previously. The primary reason is that steerable electrodes, both experimental prototypes and perimodiolar versions used in the clinic, have been designed with a preferred direction of curvature matching that of the cochlea's first turn and are better suited for the straight, initial trajectory accomplished through a cochleostomy. With RW insertions, however, the initial entry angle places the electrode tip near the MW, very

close to the BM and the OSL. Properly steering the electrode through this section would require a curvature direction opposite the remainder of the insertion, which is not possible with existing steerable electrodes. Our method, however, can apply torque in either direction, bending the tip away from either wall as needed, and requires minimal modification to the tip of existing LW electrodes. This, in our opinion, is the main contribution of the work summarized herein.

We test two hypotheses: (1) embedding a small magnet at the tip of a LW electrode does not significantly alter its RW insertion characteristics; (2) electrode insertion forces can be reduced by magnetically guiding LW electrodes that are inserted through a RW.

5.3 Materials and Methods

Details of our clinical concept are provided in Part 1 of this study and are only summarized here. Magnetically guided electrode insertions are accomplished by coordinating the motion of an external magnet to the electrode insertion with only three controlled degrees-of-freedom necessary: (1) the insertion of the electrode, (2) the rotation of the external magnet about the modiolar axis, and (3) the position of the external magnet relative to the cochlea along the modiolar axis. The translation and rotation of the external magnet are determined so that the necessary magnetic torque is generated on the tip (bending the tip away from the walls of the cochlea) while minimizing attractive magnetic forces toward the BM [25]. The entire sequence is automated and preplanned so that real-time feedback of the tip location is not required. Knowledge of the modiolar axis provides the information needed to orient the bending torque principally within the plane of the cochlear turns. It should be noted that the electrode is not pulled through the lumen; it is pushed into the cochlea through an automated insertion device while the electrode tip is guided away from the cochlear wall to assist the insertion.

To simulate this concept, an automated experimental apparatus was constructed. It is identical to the apparatus used in Part 1 of this study. The only notable exception is that the ST phantom (Figure 5.2-A) is designed with a simulated RW opening rather than a cochleostomy opening [26]. This difference requires the electrode holder to be aligned to a different entry angle (Figure 5.2-B). This was determined by trial-and-error to produce reliable insertions and is within the range of values (4°–25°) used for insertion experiments

in cadaver heads by Wimmer et al. [27].

Two separate experiments are conducted, and in both experiments, measured insertion forces are the metric to evaluate our hypotheses. The first experiment compares reference electrodes (i.e., without embedded magnets) against their magnetically tipped counterparts, with all electrodes inserted through the RW proxy at a constant speed of 0.2 mm/s and without the use of magnetic guidance. In the second experiment, guided insertions of the electrodes with magnets are accomplished using a supervised automated procedure and involve a three-step sequence that is repeated until the end of the insertion as follows: (1) increment the insertion depth by 0.5 mm, (2) rotate the external magnet to a depth-specific value stored in a look-up table, and (3) translate the external magnet relative to the phantom using a depth-specific value stored in a look-up table. The process to determine the values stored in the two look-up tables was described in Part 1 of this study. The only difference, as it pertains here, is that this process is also applied through the CH (Figure 5.1), whereas in Part 1 of this study, this section was ignored since the simulated cochleostomy brought the electrode directly into the lumen after entry. In addition, after the path curvature reverses, the torque is applied in the opposite direction of that found through the CH (Figure 5.2-C and Figure 5.2-D). For the control group, we insert the electrodes with magnets in 0.5 mm increments and with the external magnet stationary and positioned away from the electrodes.

Prior to each trial conducted in all experiments described above, the phantom is filled with saline solution [28] and a small amount of silicone lubricant [29, 30] is applied to the electrode tip.

All electrodes used were provided by MED-EL (Innsbruck, Austria), and consisted of three electrodes with magnets and two reference electrodes. All electrodes tested were described in Part 1 of this study. To prevent confusion, the labels used here are identical to the labels used in Part 1 of this study. For example, E1 is meant to represent, in both parts of the study, a Flex20 electrode with one embedded magnet. However, only for the Flex24 electrode with two magnets (E3) was the same actual electrode used in both studies; different E1 and E2 electrodes were used.

5.4 Results

As in Part 1 of this study, all angular insertion depth measurements locate the electrode tip with respect to the RW. All linear depth measurements represent movement of the insertion stage. At 0 mm linear insertion depth, the insertion stage positions the most apical electrode band just outside the ST channel. Entering through the RW rather than a cochleostomy adds about 1 mm to the path. For clarity, we define first turn as the section of the lumen from 120° to 210°, measured from the center of the RW.

Force values shown in the plots (Figure 5.3 and Figure 5.4) are the averaged sensor magnitude for every 0.5 mm of electrode insertion (to reduce sensor noise). The number of trials conducted for each electrode tested is indicated in the legend. *t*-test analysis was computed on the difference of means and provided below the insertion forces with markers indicating where along the insertion the null hypothesis can be rejected with 95% confidence. That is, at the insertion depth indicated by the marker, we are 95% confident that the difference observed is not random. The 95% confidence intervals are displayed as shaded regions.

The results of Experiment 1 are compiled in Figure 5.3. While the overall force trend (Figure 5.3-A) is similar for all electrodes being compared, the results from the *t* tests are mixed. Table 5.1 organizes the *t*-test results into the maximum effect ($\|\Delta\mathbf{F}\|$) per location cluster where the difference is statistically meaningful. The most significant difference occurs between E1 and R1 at 10–12.5 mm of insertion. Video evidence shows large stick-slip behavior for R1 that appears muted in E1 and results in a maximum decrease of about 6.7 mN. The next largest difference appears near the end of the insertions that compare E1-R1 and E2-R2. Video did not provide any obvious reason for this difference. Overall, the difference for E2-R2 never exceeded 3 mN at any point along the insertion.

A series of images are provided in Figure 5.3-B, illustrating the electrode tip (of R2) as it travels from initial entry into the ST channel, through the CH region, transitioning into the first turn, until tip contact with the LW. The electrode slides along the LW beyond the last point illustrated. The total insertion travel depicted is 9 mm.

The results of Experiment 2 are compiled in Figure 5.4, along with the magnetic-field profiles used to accomplish the guided insertions. The results from the *t* tests indicate that magnetically guiding the electrodes through the channel did statistically reduce in-

sertion forces for all tested, though with varying results. Insertion-force reduction was consistently achieved by E3 beyond 10 mm with near 50% reduction at several locations including the end. E2 also consistently achieved statistically significant insertion-force reduction, though not until about 14 mm, with near negligible insertion forces between 14–17 mm insertion depth (240°–315°). Between 17-18 mm, the insertion force reduction, though large, is not statistically meaningful because larger than typical stick-slip occurred during one of the trials of E2-nonguided. This has the effect of expanding the confidence intervals and increasing the threshold for rejecting the null hypothesis. We compare this phenomenon to the force increase due to stick-slip at 19 mm for E3-guided. In this case, the force increase was consistent for all trials, yielding smaller confidence intervals and a lower threshold to reject the null hypothesis. The maximum magnetic field applied to E2 was more than double that applied to E3, due to the larger magnetic dipole embedded in the tip of E3. Insertion-force reduction was achieved with E1 beyond 7 mm, though less pronounced.

A sequence of images visualizing a typical guided insertion (of E1) through the CH and entering the first turn is provided in Figure 5.4-B. The electrode tip is immediately directed down the lumen (Figure 5.4-B(1)) and avoids the medial wall (Figure 5.4-B(2)). Eventual contact with the medial wall does occur, but with the tip pointed away from it (Figure 5.4-B(3)), after which the electrode slides along the medial wall. At the first turn, the torque is reversed (Figure 5.4-B(4)) so that the electrode can be navigated through the basal turn. At some point, the tip "stalls (Figure 5.4-B(5)) until the apical section of the electrode begins sliding on the lateral wall, still with the tip pointed away from it (Figure 5.4-B(6)). Selected images of E2 and E3 are also provided (Figure 5.5) for comparison. In all electrodes with magnets tested, the tip is guided successfully through the CH, eliminating direct tip contact with the MW. As the electrode enters the first turn, the torque is reversed successfully so that direct tip contact with the LW is also eliminated. The angular insertion depth where the apical section of the electrodes first contact the LW of the first turn is electrode dependent, and was determined to be about 120°, 140°, and 170° for E1, E2, and E3, respectively.

5.5 Discussion

As stated in Part 1 of this study, evaluation of our hypotheses is based on *t*-test analysis of the difference between the measured insertion forces. Conclusions about the population of electrodes, however, are not possible because the number of electrodes tested is very limited. Our conclusions are based on an evaluation of the insertions themselves, and because our experiments involve multiple trials of the same insertion, the *t* tests allow us to predict what would likely happen if the same experiments on the same electrodes were to be done again. While this does not allow us to make conclusions about future electrodes with magnets (since that would require a population study), the process to produce these electrodes with magnets is repeatable. This gives us reason to think that similar results are achievable in the future.

As discussed in Part 1 of this study, the natural tip shape of R1 is tapered, but by adding a magnet to this tip, the shape becomes more rounded. In both cases in which the tip shape was altered (recall that the electrodes E1 used in Parts 1 and 2 of these studies are actually different electrodes), the stick-slip behavior of the electrode seems also to have been altered. In Part 1 of this study, the tip alteration resulted in large stick-slip behavior that did not exist otherwise, increasing the insertion forces by about 5 mN. In this study, it had the opposite effect; the stick-slip exhibited by R1 was actually muted, reducing the insertion force by about 5 mN.

Although the tip shape was not fundamentally altered for the other electrodes (E2 and E3), the measured difference in insertion force, especially where the null hypothesis can be rejected, was generally found to be larger than that observed in Part 1 of this study. It seems that modifying the electrode tip has a greater effect on RW insertions than on cochleostomy insertions. Still, the maximum difference never exceeded 4 mN at any point along the insertion except at the very end of the insertions, comparing E2-R2.

A benefit of using lateral-wall electrodes is that the electrode does not have a preferential curvature direction. This eliminates the need to properly align the electrode's preferential curvature prior to insertion as is required with perimodiolar models. Further, a known problem for perimodiolar electrodes is that any torsion that twists the electrode causes it to be no longer aligned properly to curl away from the LW [22]; this is not an issue here because the magnetic dipole at the electrode tip is symmetric about the long

axis of the electrode. Magnetic guidance will not be affected by electrode twisting before or during the insertion.

The limitations of insertion-force metrics are worth discussing. In our opinion, this type of metric is most appropriate when used for comparing the relative flexibility among competing electrodes or the relative impact of insertion techniques. Absolute sensor values cannot be used to determine potential trauma on intracochlear structures such as the BM, even if the force threshold of the membrane is known [31], because it is likely that the force sensor will understate the tip-contact force. As an example, the electrode tip contacts the MW of the CH in all nonguided insertions, yet without any detectable jump in sensor values. This is consistent with findings from a study in which BM perforation was undetected in a temporal bone specimen mounted directly to an identical force sensor to that used in our studies [28].

By eliminating direct tip contact with the MW immediately after entry through the RW, one potential trauma site to the BM and the OSL [32] can be eliminated through our technique. In a typical nonguided insertion, the electrode tip is directed toward these delicate structures upon entry through the RW. As demonstrated in the guided insertions, the tip is directed down the lumen immediately and made to avoid the MW in the CH. In addition, optimized insertion vectors, along with the necessary drilling often required to achieve them [7, 14], are likely no longer crucial.

A second site of potential trauma [32, 33] is along the first turn, where contact with the LW sometimes deflects the electrode tip out-of-plane into the BM. To avoid this type of impingement, the electrodes are navigated successfully so that the initial contact is distributed over the apical section of the electrode, rather than localized at the tip, and with the tip always directed away from the wall. We believe this likely to be less traumatic.

In addition, the use of a magnetic field intended to pull the tip of the electrode away from the MW and LW has the benefit of providing a passive magnetic spring that attempts to keep the orientation of the tip parallel to the BM, which will further mitigate the risk of the magnetic tip deviating out-of-plane into the BM. This protection of the BM, which can be deduced from first principles, cannot be observed in the insertion-force data.

The tips of E1, E2, and E3 reach 135°, 150°, and 180°, respectively, before initial contact with the LW is made by the apical section of the electrode (see Figure 5.4-B(6), Figure

5.5-3, and Figure 5.5-6). Contrast this to the cochleostomy trials (Part 1 of this study) wherein each electrode tip was navigated to about 180° before the same event occurred. This implies that entering directly into the lumen via the cochleostomy provides more consistent avoidance of the LW.

We compare the magnetic-field profiles used here with those used to accomplish the insertions via cochleostomy in Part 1 of this study. For both E2 and E3, the maximum magnetic field needed for these experiments is about 28% higher than what was needed in Part 1, whereas the maximum magnetic field needed to guide E1 in these experiments was actually 28% lower than in Part 1 of this study. Realizing that additional work is needed to substantiate this, it is possible that the flexibility of individual electrodes, even based on the same electrode model, may vary. However, the relatively small difference between fields required suggests that a single clinical magnetic-guidance system could be designed for use in both cochleostomy and RW insertions.

In both parts of this study, we generated the insertion profiles offline, and then ran those insertions in an open-loop fashion. For the sake of performing controlled and repeatable experiments, we chose to generate the profiles following a specific procedure that we described in Part 1, but there is no evidence that the procedure results in optimal insertions. In our intended concept, the insertions will be modified in real time using a sensor measuring the force at the location where the insertion stage holds the electrode, as has been demonstrated previously [34]. This will likely enable improved insertions, as well as monitoring to prevent any unsafe rises in the insertion force.

Finally, some of our prototype electrode arrays were made with a substantial gap between the embedded magnet and the distal electrode band, and we observed substantial bending in the gap region, which has low stiffness due to the lack of any wires to act as an elastic backbone. This is undesirable as it resulted in an artificial limit to the applied torque we were able to apply to pull the array away from the LW before risking a collision of the tip with the MW. In future prototypes, it will be important to embed the tip magnet close to the distal electrode band.

5.6 Conclusion

In this study, we demonstrated that magnetic guidance of a robotically inserted lateral-wall cochlear-implant electrode equipped with a permanent magnet at its tip results in a significant reduction in insertion forces when inserted via the round window. To our knowledge, this is the first attempt at actively steering clinical-type electrodes of any type through both the cochlear hook and the first turn. Direct tip contact at the medial wall of the cochlear hook and at the lateral wall of the first turn can be eliminated while maintaining the inherent safety of flexible, lateral-wall electrodes. Insertion-force reduction was greatest with the MED-EL Flex24 electrode and less pronounced with the MED-EL Flex20 electrode.

5.7 Acknowledgements

The authors gratefully acknowledge support from Anandhan Dhanasingh of MED-EL for fabricating the electrodes used in these experiments. Research reported in this chapter was supported by the National Institute on Deafness and Other Communication Disorders of the National Institutes of Health under Award Number R01DC013168. The content is solely the responsibility of the authors and does not necessarily represent the official views of the National Institutes of Health.

5.8 References

[1] L. Leon, F. M. Warren, and J. J. Abbott, "An in-vitro insertion-force study of magnetically guided, lateral-wall, cochlear-implant electrodes, part I: Via cochleostomy," *Otol. Neurotol.*, (under review).

[2] A. P. Campbell, M. T. Dillon, C. A. Buchman, and O. F. Adunka, "Hearing preservation cochlear implantation," *Curr. Otorhinolaryngol. Rep.*, vol. 1, no. 2, pp. 69–79, 2013.

[3] G. B. Wanna, J. H. Noble, M. L. Carlson, R. H. Gifford, M. S. Dietrich, D. S. Haynes, B. M. Dawant, and R. F. Labadie, "Impact of electrode design and surgical approach on scalar location and cochlear implant outcomes," *Laryngoscope*, 2014.

[4] R. J.S. Briggs, M. Tykocinski, J. Xu, F. Risi, M. Svehla, R. Cowan, T. Stover, P. Erfurt, and T. Lenarz, "Comparison of round window and cochleostomy approaches with a prototype hearing preservation electrode," *Audiol. Neurotol.*, vol. 11 Suppl 1, pp. 42–8, 2006.

[5] D. A. Gudis, M. Montes, D. C. Bigelow, and M. J. Ruckenstein, "The round window: is it the "cochleostomy" of choice? experience in 130 consecutive cochlear implants," *Otol. Neurotol.*, vol. 33, no. 9, pp. 1497–1501, 2012.

[6] S. Havenith, M. J. W. Lammers, R. A. Tange, F. Trabalzini, A. della Volpe, G. J. M. G. van der Heijden, and W. Grolman, "Hearing preservation surgery: cochleostomy or round window approach? a systematic review," *Otol. Neurotol.*, vol. 34, no. 4, pp. 667–74, Jun 2013.

[7] P. S. Roland, C. G. Wright, and B. Isaacson, "Cochlear Implant Electrode Insertion: The Round Window Revisited," *Laryngoscope*, vol. 117, no. 8, pp. 1397–1402, 2007.

[8] A. Causon, C. Verschuur, and T. A. Newman, "A retrospective analysis of the contribution of reported factors in cochlear implantation on hearing preservation outcomes.," *Otol. Neurotol.*, vol. 36, no. 7, pp. 1137–1145, Aug 2015.

[9] E. F. O'Connor and A. Fitzgerald, "Hearing preservation surgery: current opinions," *Adv. Otorhinolaryngol.*, vol. 67, pp. 108–115, 2010.

[10] F. Hassepass, S. Bulla, W. Maier, R. Laszig, S. Arndt, R. Beck, L. Traser, and A. Aschendorff, "The new mid-scala electrode array: a radiologic and histologic study in human temporal bones," *Otol. Neurotol.*, vol. 35, no. 8, pp. 1415–20, Sep 2014.

[11] H. A. Breinbauer and M. Praetorius, "Variability of an ideal insertion vector for cochlear implantation.," *Otol. Neurotol.*, vol. 36, no. 4, pp. 610–617, Apr 2015.

[12] R. J.S. Briggs, M. Tykocinski, K. Stidham, and J. B. Roberson, "Cochleostomy site: implications for electrode placement and hearing preservation," *Acta Otolaryngol.*, vol. 125, no. 8, pp. 870–876, 2005.

[13] X. Meshik, T. A. Holden, R. A. Chole, and T. E. Hullar, "Optimal cochlear implant insertion vectors," *Otol. Neurotol.*, vol. 31, no. 1, pp. 58, 2010.

[14] Y. Shapira, A. A. Eshraghi, and T. J. Balkany, "The perceived angle of the round window affects electrode insertion trauma in round window insertion - an anatomical study.," *Acta Otolaryngol.*, vol. 131, no. 3, pp. 284–289, Mar 2011.

[15] K. S. van der Marel, J. J. Briaire, B. M. Verbist, T. J. Muurling, and J. H. M. Frijns, "The influence of cochlear implant electrode position on performance.," *Audiol. Neurotol.*, vol. 20, no. 3, pp. 202–211, 2015.

[16] P. M. M. C. Li, H. Wang, C. Northrop, S. N. Merchant, and J. B. Nadol, Jr, "Anatomy of the round window and hook region of the cochlea with implications for cochlear implantation and other endocochlear surgical procedures," *Otol. Neurotol.*, vol. 28, no. 5, pp. 641–648, 2007.

[17] J. Addams-Williams, L. Munaweera, B. Coleman, R. Shepherd, and S. Backhouse, "Cochlear implant electrode insertion: in defence of cochleostomy and factors against the round window membrane approach," *Cochlear Implants Int.*, vol. 12 Suppl 2, pp. S36–9, Aug 2011.

[18] C. Richard, J. N. Fayad, J. Doherty, and F. H. Linthicum Jr, "Round window versus cochleostomy technique in cochlear implantation: Histological findings," *Otol. Neurotol.*, vol. 33, no. 7, pp. 1181, 2012.

[19] O. F. Adunka and C. A. Buchman, "Scala tympani cochleostomy I: results of a survey," *Laryngoscope*, vol. 117, no. 12, pp. 2187–2194, 2007.

[20] B. Fraysse, Á. R. Macías, O. Sterkers, S. Burdo, R. Ramsden, O. Deguine, T. Klenzner, T. Lenarz, M. M. Rodriguez, E. Von Wallenberg, and C. James, "Residual hearing conservation and electroacoustic stimulation with the nucleus 24 contour advance cochlear implant," *Otol. Neurotol.*, vol. 27, no. 5, pp. 624–633, 2006.

[21] I. Todt, G. Rademacher, J. Wagner, F. Göpel, D. Basta, E. Haider, and A. Ernst, "Evaluation of cochlear implant electrode position after a modified round window insertion by means of a 64-multislice ct," *Acta Otolaryngol.*, vol. 129, no. 9, pp. 966–70, Sep 2009.

[22] A. Coordes, A. Ernst, G. Brademann, and I. Todt, "Round window membrane insertion with perimodiolar cochlear implant electrodes," *Otol. Neurotol.*, vol. 34, no. 6, pp. 1027–1032, 2013.

[23] A. Jeyakumar, S. F. Peña, and T. M. Brickman, "Round window insertion of precurved electrodes is traumatic," *Otol. Neurotol.*, vol. 35, no. 1, pp. 52–7, Jan 2014.

[24] M. A. Souter, R. J.S Briggs, C. G. Wright, and P. S. Roland, "Round window insertion of precurved perimodiolar electrode arrays: how successful is it?," *Otol. Neurotol.*, vol. 32, no. 1, pp. 58–63, 2011.

[25] J. R. Clark, L. Leon, F. M. Warren, and J. J. Abbott, "Magnetic guidance of cochlear implants: Proof-of-concept and initial feasibility study," *J. Med. Devices*, vol. 6, no. 3, pp. 035002, 2012.

[26] L. Leon, M. S. Cavilla, M. B. Doran, F. M. Warren, and J. J. Abbott, "Scala-tympani phantom with cochleostomy and round-window openings for cochlear-implant insertion experiments," *J. Med. Devices*, vol. 8, no. 4, pp. 041010, 2014.

[27] W. Wimmer, B. Bell, M. E. Huth, C. Weisstanner, N. Gerber, M. Kompis, S. Weber, and M. Caversaccio, "Cone beam and micro-computed tomography validation of manual array insertion for minimally invasive cochlear implantation," *Audiol. Neurotol.*, vol. 19, no. 1, pp. 22–30, 2014.

[28] Y. Nguyen, M. Miroir, G. Kazmitcheff, J. Sutter, M. Bensidhoum, E. Ferrary, O. Sterkers, and A. Bozorg Grayeli, "Cochlear implant insertion forces in microdissected human cochlea to evaluate a prototype array," *Audiol. Neurotol.*, vol. 17, no. 5, pp. 290–8, 2012.

[29] O. Adunka, J. Kiefer, M. H. Unkelbach, T. Lehnert, and W. Gstoettner, "Development and evaluation of an improved cochlear implant electrode design for electric acoustic stimulation," *Laryngoscope*, vol. 114, no. 7, pp. 1237–41, Jul 2004.

[30] G. Kontorinis, G. Paasche, T. Lenarz, and T. Stöver, "The effect of different lubricants on cochlear implant electrode insertion forces," *Otol. Neurotol.*, vol. 32, no. 7, pp. 1050–6, Sep 2011.

[31] D. Schuster, L. B. Kratchman, and R. F. Labadie, "Characterization of intracochlear rupture forces in fresh human cadaveric cochleae," *Otol. Neurotol.*, Sep 2014.

[32] M. L. Carlson, C. L.W. Driscoll, R. H. Gifford, and S. O. McMenomey, "Cochlear implantation: current and future device options," *Otolaryngol. Clin. N. America*, vol. 45, no. 1, pp. 221–248, 2012.

[33] F. G. Zeng, S. Rebscher, W. Harrison, X. Sun, and H. Feng, "Cochlear implants: System design, integration, and evaluation," *IEEE Reviews in Biomed. Eng.*, vol. 1, pp. 115–142, 2008.

[34] D. Schurzig, R. F. Labadie, A. Hussong, T. S. Rau, and R. J. Webster III, "Design of a tool integrating force sensing with automated insertion in cochlear implantation.," *IEEE ASME Trans. Mechatron.*, vol. 17, no. 2, pp. 381–389, Apr 2012.

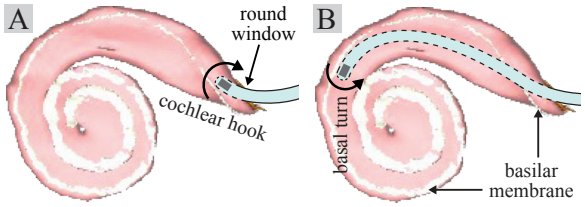

Figure 5.1. The ability to steer an electrode (modified with a magnet at its tip) through the cochlear hook (A) and the basal turn of the cochlea (B) requires the electrode to bend in opposite directions. The scala-tympani model depicted here, with the basilar membrane shaded in white, is generated from software provided to the public by Eaton-Peabody Laboratory (Boston, MA).

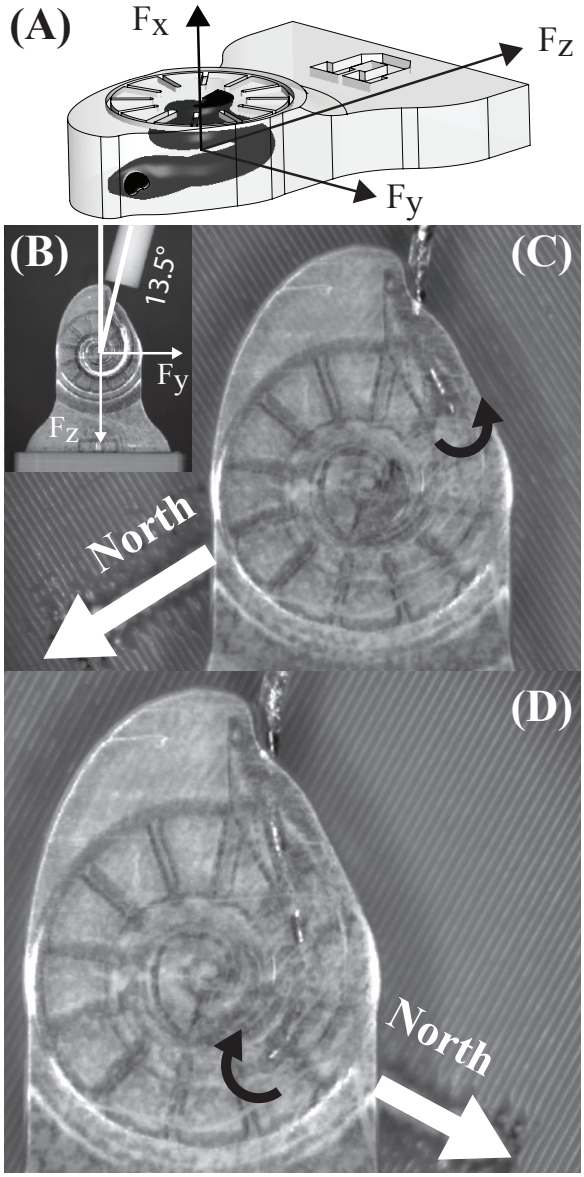

Figure 5.2. Electrodes are inserted through a scala-tympani phantom, designed with a round-window opening (A). The electrode holder is aligned as shown (B) to achieve repeatable insertions. In the guided experiments, an external magnet is used to apply bending torque to the electrode tip to avoid the medial wall of the cochlear hook (C) and the lateral wall of the basal turn (D). To achieve this, the north axis of the external magnet must be correctly oriented relative to the magnetic tip to apply bending torque in opposite directions (as indicated by the black, curved arrows).

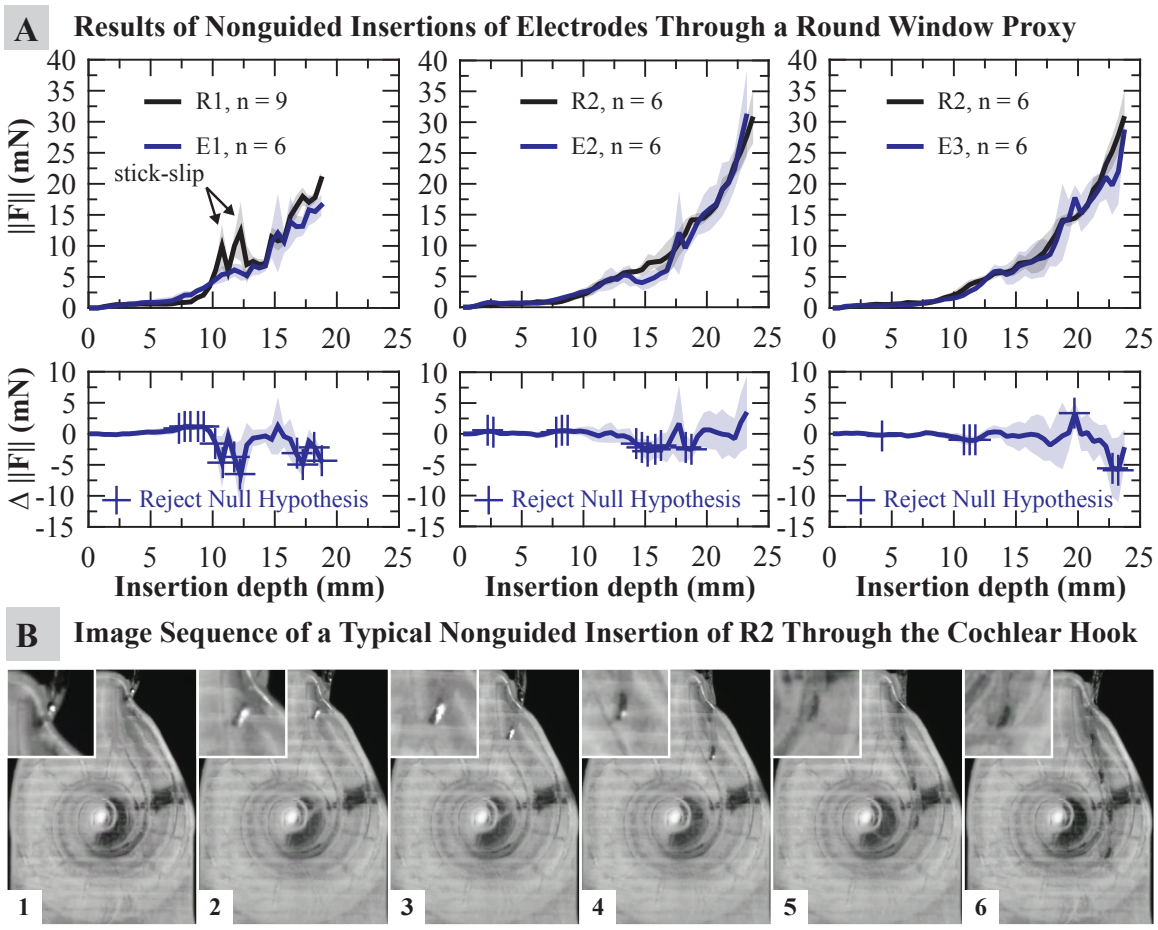

Figure 5.3. A. (Top) Results of experiment 1 compare insertion forces of electrodes inserted at a constant speed of 0.2 mm/s, without the use of magnetic guidance. 95% confidence intervals are shown as shaded regions. Force values shown on the plots are the magnitude $\|\mathbf{F}\| = \sqrt{F_x^2 + F_y^2 + F_z^2}$ of the averaged sensor values for every 0.5 mm of electrode insertion (to reduce sensor noise). The number of trials conducted for the electrode tested is indicated in the legend. (Bottom) t tests compute the difference of means with markers that indicate where along the insertion the null-hypothesis can be rejected with 95% confidence. B. A series of image snapshots depicting a typical insertion of a lateral-wall electrode when inserted through the round-window proxy. Immediately upon entry, the electrode tip is directed toward the medial wall (C-1). Soon thereafter, the electrode tip contacts the medial wall (C-2) and slides along it (C-3 and C-4) until the path curvature reverses (C-5). The electrode tip then contacts the LW near 120° (C-6).

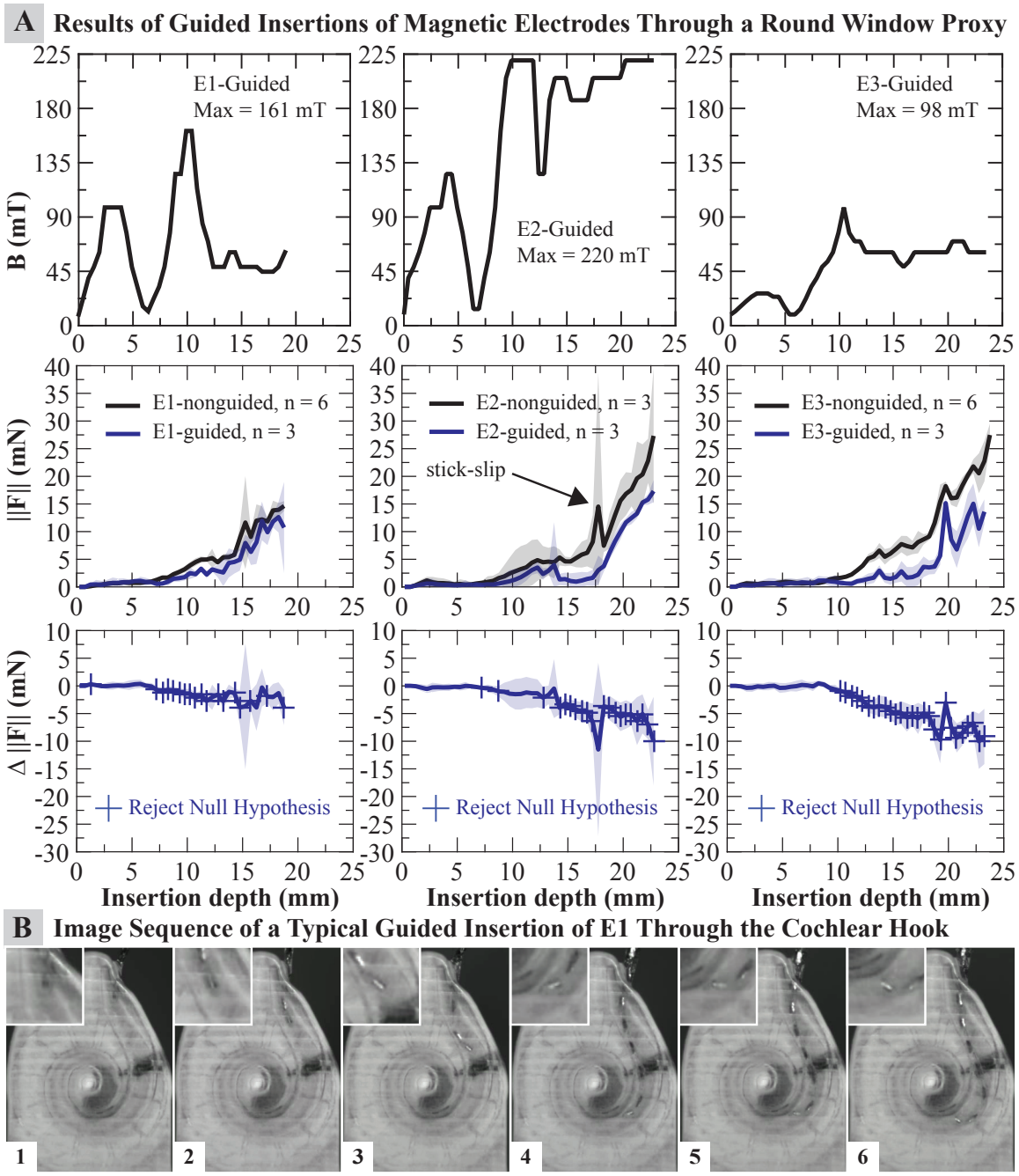

Figure 5.4. A. Results of experiment 2 compare nonguided and magnetically guided insertions of the electrodes with magnets. The top row shows the applied magnetic field used to achieve the guided insertions. Measured insertion forces (with 95% confidence levels shaded) and *t*-test analysis are placed below the magnetic field profiles. B. Images chosen to represent a typical guided insertion of an electrode with magnet (E1 in this example) wherein the tip is navigated through the cochlear hook.

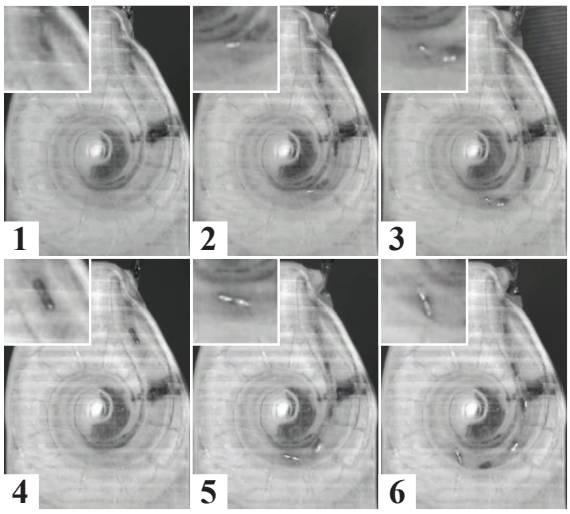

Figure 5.5. The behavior of E2 (top row) and E3 (bottom row) under magnetic guidance is depicted at selected locations: through the cochlear hook (left), at the first turn (middle), and upon first contact with the lateral wall (right).

Table 5.1. Table organizing the *t*-test results from Figure 5.3 into location clusters where the force difference is statistically significant along with their corresponding maximum measured difference. Units for depth and $\Delta \|\mathbf{F}\|_{max}$ are mm and mN, respectively.

E_1, R_1		E_2, R_2		E_3, R_2	
depth	$\Delta \|\mathbf{F}\|_{\max}$	depth	$\Delta \|\mathbf{F}\|_{\max}$	depth	$\Delta \|\mathbf{F}\|_{\max}$
7.0–9.5	1.2	2.0–3.0	0.5	4.0–4.5	0.2
10.0–12.5	6.7	7.5–9.0	0.6	10.5–12.0	1.1
16.5–19.0	4.8	14.0–16.5	2.8	19.5–20.0	3.3
		18.0–19.0	2.6	22.5–23.5	5.8

CHAPTER 6

OPTIMAL SIZE AND PLACEMENT OF THE MAGNETIC DIPOLE-FIELD SOURCE FOR MAGNETICALLY GUIDED ELECTRODE INSERTIONS

This chapter summarizes an optimal configuration (size and location) of a magnetic dipole-field source for use in a clinic to achieve magnetically guided insertions of cochlear-implant electrode arrays. In all prior work, it had been configured to travel on a path that would be coincident with the cochlea's modiolar axis, which was an unnecessary constraint that was useful to demonstrate feasibility but may not be ideal in the clinic.

6.1 Abstract

Magnetically guided insertions of cochlear-implant electrode arrays have been demonstrated, at clinical scale, to reduce insertion forces, which is believed to be correlated to a reduction in trauma. In those prior studies, the magnetic dipole-field source (MDS) was configured to travel on a path that would be coincident with the cochlea's modiolar axis, which was an unnecessary constraint that was useful to demonstrate feasibility. In this chapter, we determine the optimal configuration (size and location) of the MDS needed to accomplish guided insertions with a 100 mT field strength required at the cochlea, and we provide a methodology to perform such an optimization more generally. Based on computed-tomography (CT) scans of 30 patients, the magnetic dipole-field source should be lateral-to and slightly anterior-to the cochlea with an approximate radius (mean and standard deviation across patients) of 64 mm and 4.5 mm, respectively. We compare these results to the modiolar configuration and find that the volume of the MDS can be reduced by a factor of 5 with a 43% reduction in its radius by moving it to the optimal location. We conservatively estimate that the magnetic forces generated by the optimal

configuration are two orders of magnitude below the threshold needed to puncture the basilar membrane. Although patient-specific optimal configurations are computed in this chapter, a one-size-fits-all version with a radius of approximately 75 mm is more robust to registration error and likely more practical.

6.2 Introduction

Cochlear implants are neural-prosthetic devices implanted into the cochlea to directly stimulate the auditory nerve, bypassing the hearing mechanics of the auditory system and restoring effective hearing to those with profound sensorineural hearing loss. During the surgery, the surgeon either drills a hole in the cochlea (known as a cochleostomy) or makes an incision into the round-window membrane to insert an array of electrodes embedded in silicone (commonly referred to as the "electrode array") into the scala-tympanic (ST) chamber of the cochlea.

The insertion of the electrode array is known to cause intracochlear damage if the insertion forces exceed the inherent strength of the tissue [1]. The most traumatic damage occurs if the electrode array perforates the basilar membrane and deviates into the adjacent scala. The usual site for such trauma is along the first turn where contact with the lateral wall sometimes deflects the electrode-array tip (EAT) out-of-plane and into the basilar membrane [1–3]. This type of trauma is a strong predictor for permanent loss of residual hearing [4]. Evidence also suggests that hearing outcomes improve by avoiding this type of trauma [5]. Preservation of residual hearing and reduction of insertion trauma is now a strong priority in cochlear implantation.

A method to magnetically guide the EAT through the ST during insertion has been demonstrated using clinical lateral-wall-type electrode arrays with embedded magnets at their tips. Repeatable, automated insertions were conducted in at-scale ST phantoms designed with simulated cochleostomy [6] and round-window [7] openings. A magnetic dipole-field source (MDS), external to both the electrode array and the phantom, applied the necessary magnetic torque to the EAT, actively bending it away from the ST walls, and reducing the insertion forces by as much as 50% over nonguided insertions. Moreover, at the first turn in the basal plane, where a high percentage of basilar-membrane perforations occur, the tip of the electrode array was never in contact with the lateral wall. These studies

confirmed earlier 3-to-1 scale proof-of-concept studies [8].

The bending torque that is applied to the tip is given by the equation

$$\boldsymbol{\tau} = \mathbf{m} \times \mathbf{B} \tag{6.1}$$

where $\boldsymbol{\tau}$ is the torque in units $\{\mathrm{N{\cdot}m}\}$, $\mathbf{m}$ is the dipole moment of the magnet at the EAT in units $\{\mathrm{A{\cdot}m^2}\}$, and $\mathbf{B}$ is the magnetic field vector at the EAT in units $\{\mathrm{T}\}$ (Figure 6.1-left). As illustrated (Figure 6.1-center), the path of the electrode and the EAT is mostly constrained on a plane orthogonal to the modiolus; we will refer to this as the basal plane. Therefore, to bend the tip around the critical first turn where the EAT would normally contact the lateral walls, the component of the torque vector parallel to the modiolar axis should be maximized so as to bend the EAT principally within this plane. In other words, we want to minimize any component of the torque that could bend the EAT out of the plane and into the basilar membrane. This is accomplished by generating a magnetic-field vector that rotates on the basal plane while leading the EAT's dipole moment by up to 90°. All of our prior work achieved this by configuring the trajectory of the MDS to rotate about and translate along the modiolar axis. This is illustrated in Figure 6.1-right in configuration 1 and is referred to herein as the modiolar configuration. However, there is an advantageous reason for the MDS to approach the patient along a different trajectory: the size of the MDS can be reduced by positioning it closer to the cochlea (as illustrated in the other two configurations). The goal here is to generate the required bending torque on the EAT from any location or trajectory that offers a clinical advantage, without the previous constraints placed on the MDS.

It has been shown that a rotating magnet, positioned anywhere relative to a fixed point in space, can generate at this fixed point a rotating magnetic field vector on any desired plane simply by rotating the magnet about a unique rotation axis [9]. This concept is illustrated in Figure 6.1-right where the rotating magnet is shown in three hypothetical configurations, each with a unique axis-of-rotation ($\hat{\boldsymbol{\Omega}}$) to generate a magnetic field vector at the cochlea that rotates on the basal plane and about the modiolar axis. Thus, from any arbitrary position outside the patient's head, the rotating magnet can generate the necessary rotating magnetic field for guided insertions.

Note that in all the configurations shown, the direction from the MDS's center to the

cochlea does not change. This allows the magnet to rotate about a constant axis-of-rotation while translating along a single degree-of-freedom toward or away from the patient's head. Part of the surgical planning could require the MDS to be positioned to some minimum clearance from the surface of the head with the linear stage extended to its maximum range of travel. Then, the linear stage could be retracted along the planned translation direction to the beginning of its range of motion. Such an alignment procedure would preclude any potential collision with the patient.

Throughout this work, we assume that the MDS comprises a spherical permanent magnet. Spherical magnets have the desirable property that the point-dipole model perfectly describes their magnetic field. In addition, our group has already developed a robotic end-effector that comprises a spherical permanent magnet [10]. Alternatively, an electromagnetic source such as an Omnimagnet [11], whose magnetic field is accurately described by the point-dipole model outside of its minimum bounding sphere, could be used in place of a spherical permanent magnet. In that case, it would not be necessary to translate the MDS relative to the patient's head, because the strength of its magnetic dipole can be controlled. However, large currents would be necessary to generate the required dipole strength from an Omnimagnet of a given minimum bounding sphere compared to the same sized spherical permanent magnet.

In this chapter, we explore the optimal configuration, defined as the smallest MDS needed to accomplish guided insertions and its location relative to the cochlea. In Section 6.3, we present all of the necessary modeling equations that relate the size, strength, and location of the MDS to the magnetic field that can be generated at the cochlea. In Section 6.4, computed-tomography (CT) scans of 30 patients are segmented to create three-dimensional models of the surfaces of the patients' heads, along with the location and orientation of the cochlea. In Section 6.5, we determine the optimal configuration (size and location) of the MDS for each of the 30 patients. We compare the results to the MDS required in the modiolar configuration and find that the MDS size can be substantially reduced by moving it to the optimal location. Although we are primarily relying on magnetic *torque* applied to the EAT to bend the electrode array, in general, there will also be a magnetic *force* applied to the EAT. In Section 6.6, we provide a conservative force estimate that indicates that magnetic forces are unlikely to apply any forces that might be dangerous

to the delicate basilar membrane. In Section 6.7, we perform a sensitivity analysis to the size, strength, and positioning of the MDS. Although we compute patient-specific optimal configurations in this chapter, it is likely more practical to develop a one-size-fits-all MDS, which will be overdesigned for the majority of patients. In Section 6.8, we consider the robust placement of the MDS in light of this fact.

6.3 Magnetic Modeling

The necessary magnetic field to achieve successful guided electrode-array insertions has been determined by our prior work [6, 7]. In that study, Flex-24 electrode arrays provided by MED-EL (Innsbruck, Austria) with a $4.73\times10^{-5}\,\mathrm{A{\cdot}m^2}$ permanent magnet embedded in the EAT were guided successfully through a plastic ST phantom [12]. The maximum magnetic field used in those experiments was determined to be 80 mT and 100 mT if inserted through a simulated cochleostomy and round window, respectively. We will use 100 mT as the nominal magnetic-field requirement herein.

The magnitude of the dipole moment $\mathbf{M}$, in units $\{\mathrm{A{\cdot}m^2}\}$, for a spherical permanent-magnet MDS of radius r in units $\{\mathrm{m}\}$ is given by

$$\|\mathbf{M}\| = \frac{4\pi r^3 B_r}{3\mu_o} \tag{6.2}$$

where $\frac{4}{3}\pi r^3$ is the volume of the spherical magnet, $\mu_0 = 4\pi \times 10^{-7}\ \mathrm{T{\cdot}m{\cdot}A^{-1}}$ is the permeability of free space, and B_r is the residual flux density in units $\{\mathrm{T}\}$, which is an intrinsic property of the magnetic material.

The magnetic field vector $\mathbf{B}$ in units $\{\mathrm{T}\}$ that is generated at the cochlea by a spherical magnet, modeled as a dipole $\mathbf{M}$, can be computed by the point-dipole equation

$$\mathbf{B} = \frac{\mu_0}{4\pi \|\mathbf{p}\|^3}\left(\frac{3\,(\mathbf{M}{\cdot}\mathbf{p})}{\|\mathbf{p}\|^2}\mathbf{p} - \mathbf{M}\right) \tag{6.3}$$

where $\mathbf{p}$ is the vector from the magnet's center to the cochlea in units $\{\mathrm{m}\}$. We will define the location of the cochlea as the intersection of the modiolar axis and the basal plane [12].

We can simplify the use of (6.3) based on our intended use of the MDS. We intend to mount the MDS on a one-degree-of-freedom linear stage with its linear trajectory pre-planned so as to avoid any contact with the patient at any point during its translation. During initial positioning, we envision the MDS to be placed as close to the surface of

the head as allowable. This will represent the point on the trajectory where the distance between the MDS and the cochlea is shortest. This is illustrated by the MDS that is almost touching the head surface in all three of the hypothetical configurations shown in Figure 6.1-right. In general, the shorter the distance between the MDS and the cochlea, the smaller the MDS can be and still generate the needed magnetic field.

Now suppose that at its closest approach to the patient, the MDS rotates about the required rotation axis ($\hat{\mathbf{\Omega}}$) in order to generate a rotating field vector that lies on the basal plane. For every complete revolution of $\mathbf{M}$ about $\hat{\mathbf{\Omega}}$, there will always be instances in which $\mathbf{M} \cdot \mathbf{p} = 0$. Thus, for a given $\mathbf{p}$, the field magnitude will vary based on the relationship between $\mathbf{M}$ and $\mathbf{p}$, and it will reach a minimum magnitude of

$$\|\mathbf{B}\|_{min} = \frac{\mu_0 \|\mathbf{M}\|}{4\pi \|\mathbf{p}\|^3} \tag{6.4}$$

Since we are searching for the location where the MDS can be smallest, we cannot know the trajectory of the MDS in advance nor the relationship between $\mathbf{M}$ and $\mathbf{p}$, so to be conservative, we will assume that the field magnitude is always at this minimum possible for a given $\mathbf{p}$.

Assuming that the field magnitude necessary to achieve guided insertions of electrode arrays is known [6, 7], then combining (6.2) and (6.4) yields the equation to compute the required minimum radius of the MDS.

$$r = \left(\frac{3 \|\mathbf{B}\|_{min}}{B_r} \right)^{1/3} \|\mathbf{p}\| \tag{6.5}$$

Taking each surface point on the head, we can simulate a spherical magnet touching the point and normal to the local surface as defined by the surface normal (Figure 6.2). By defining this surface point as $\mathbf{s}$ and its surface normal of unit length as $\hat{\mathbf{n}}$, the vector from the center of the magnet to the cochlea is

$$\mathbf{p} = -\mathbf{s} - (r + \delta)\hat{\mathbf{n}}. \tag{6.6}$$

where r is the radius of the magnet and δ is the clearance from the surface point to the surface of the magnet along $\hat{\mathbf{n}}$. In the case where the magnet touches the patient, the clearance is $\delta = 0$.

The distance from the magnet center to the cochlea can be calculated using the (modified) law of cosines as

$$\|\mathbf{p}\|^2 = \|\mathbf{s}\|^2 + (r+\delta)^2 + 2(r+\delta)s_n \tag{6.7}$$

where $s_n = \|\mathbf{s}\|\cos\theta$ and θ is illustrated in Figure 6.2. s_n can also be considered the projection of $\|\mathbf{s}\|$ onto $\hat{\mathbf{n}}$.

Next, rearrange (6.5) into the form given by

$$K\|\mathbf{p}\|^2 - r^2 = 0 \tag{6.8}$$

where the nondimensional term

$$K = \left(\frac{3\|\mathbf{B}\|_{min}}{B_r}\right)^{\frac{2}{3}} \tag{6.9}$$

expresses a ratio of the required magnetic field ($\|\mathbf{B}\|_{min}$) to a magnetic property of the material (B_r). By combining (6.7) with (6.8) and rearranging it into the form of a quadratic equation

$$(K-1)r^2 + (2K\delta + 2Ks_n)r + (K\|\mathbf{s}\|^2 + K\delta^2 + 2K\delta s_n) = 0 \tag{6.10}$$

r required at some surface point $\mathbf{s}$ can be solved for using the quadratic formula. The standard quadratic formula yields two solutions, and the solutions are not guaranteed to be real. Fortunately, we can constrain some of the parameters, based on our application, to yield a valid solution to (6.10) (i.e., $r \in \mathbb{R}^+$): $K > 0$, $\|\mathbf{s}\| > 0$, and $\delta \geq 0$.

We ignore all surface points with surface normals directed back toward the cochlea by selecting only the surface points in which $\mathbf{s}\cdot\hat{\mathbf{n}} \geq 0$ (i.e., $s_n \geq 0$). This typically eliminates some of the points on the ear or nose as shown in Figure 6.3.

Finally, by further restricting $0 < K < 1$, the solution to (6.10) always yields $r \in \mathbb{R}^+$ and is given by

$$r = \frac{K(\delta + s_n) + \sqrt{K(K(s_n^2 - \|\mathbf{s}\|^2) + \|\mathbf{s}\|^2 + \delta^2 + 2\delta s_n)}}{(1-K)} \tag{6.11}$$

The constraint on K implies that the required magnetic field strength at the cochlea must not be more than $\frac{1}{3}$ the residual flux density of the magnet.

$$3\|\mathbf{B}\|_{min} < B_r \tag{6.12}$$

Since the field measured on the surface of a spherical magnet falls within the range $\|\mathbf{B}\| \in \left[\frac{B_r}{3}, \frac{2B_r}{3}\right]$, (6.12) represents a conservative estimate of the field that can be generated by a spherical magnet in an arbitrary direction $\hat{\mathbf{p}}$.

6.4 Segmentation of CT Scans

Using (6.11) to compute the magnet size required at a given location relative to the patient's head requires a set of surface points and their associated surface normals. To our knowledge, a representative head-surface model of sufficient fidelity has not been published in which the location of the cochlea is also identified. In practice, patient-specific head surfaces can be obtained, and the location of the cochlea and orientation of the modiolus can be identified, from segmented CT slices. This yields a three-dimensional map of surface points and their surface normals for our analysis. Results can then be considered statistically across the population.

CT scans of anonymous patients were obtained from the University of Utah (Table 6.1). Standard CT temporal-bone imaging procedures were used in each case. In addition, two sets of cadaver scans were obtained from the National Library of Medicine's Visible Human Project [13]. In all the sets, the pixel resolution is less than 1 mm. The slice resolution varied significantly from set to set.

Standard MATLAB (Natick, MA) commands, identified in *italics* in this section, are used to generate the three-dimensional patient-specific surfaces. The CT data are available as DICOM binary data and packaged as 12-bit grayscale image intensity values and a header with meta-data regarding the CT scan and the imaging protocol used. The images and headers are extracted using *dicomread* and *dicominfo*, respectively. The meta-data is needed to convert from image frame to the CT frame. We use the standard right-anterior-superior (RAS) convention in which $+x$ is directed to the patient's right side, $+y$ is directed anteriorly, and $+z$ is directed superiorly.

Grayscale images are converted to black-and-white using *im2bw* where the threshold to determine if the pixel should be considered black or white is set automatically by *graythresh*. Each slice of each set is segmented to extract the boundary of the skull using *bwboundaries*, which automatically outlines the boundaries of the main features in the image. There are usually multiple boundaries detected, and the one that clearly is associated with the skull is chosen. In cases where the scene is too cluttered to conveniently use *bwboundaries*, we use *bwtraceboundaries* and select the pixel where the trace should be started. We show an example of the boundaries in Figure 6.4-A. The grayscale image is depicted with the automatically generated boundaries overlayed on the image

in red. Though not shown, the area enclosed by the boundaries would be white in the black-and-white equivalents.

This boundary is used to build a slice-specific image mask to remove all features outside this mask; this is generated using *poly2mask* (Figure 6.4-B). The mask is a logical array where all locations inside the mask are set to true and all locations outside the mask are set to false. This mask can be visualized by mapping false and true to black and white, respectively. To remove the background, all pixels of the grayscale image that are outside this mask will have their intensity values set to zero. This yields an image of just the head without any of the background.

Next, this image mask is eroded (i.e., made smaller) using *imerode* for the purpose of handling internal features of the head, such as the nasal cavity (Figure 6.4-C). This is necessary because these features could be interpreted as part of the head surface (by the function *isosurface* described later). To handle this, we set all the intensity values for all the pixels inside this eroded mask to the maximum intensity value of the image slice.

The result is an image where the background is removed and the interior features are washed out, with a thin border of grayscale pixels at the head surface (Figure 6.4-D). The resulting segmented images are then stacked to create a three-dimensional array of intensity values per pixel and slice. This is illustrated in Figure 6.4-E (but only showing every tenth slice).

This array of intensity values can also be regarded as a scalar function of three parameters $I = f(x, y, z)$ where x and y are the pixel coordinates, z is the slice coordinate, and I is the scalar intensity value at those coordinates. As a result, this function can be interpolated to find the coordinate (x, y, z) where the intensity map transitions away from the background intensity. Interpolation then yields the approximate coordinates of the head surface. To accomplish this, a homogenous transform is used to convert the pixel and slice coordinates from the image frame to the global CT frame. Then, the scalar function is filtered using *smooth3* to generate smoother surface normals. Next, *isosurface* is used to interpolate for the coordinates at the desired intensity value. We chose an intensity value of 5 as representative of the transition from the background to the head surface (the images are provided as 12-bit unsigned integers where 0 is mapped to black and 4095 is mapped to white). The surface normals corresponding to the surface points interpolated by *isosurface*

are finally generated by *isonormals*. The combination of surface points and surface normals define the final head surface, as illustrated in Figure 6.4-F.

Finally, the cochlea and the modiolar axis are located for both sides of each patient (Figure 6.5). In one study [14], the average angle between the modiolar axis and the transverse plane of the skull was determined to be nearly zero ($1.8^\circ \pm 3^\circ$, n=10). So, for simplicity, we will assume that the modiolar axis lies on the slice plane where the cochlea is located.

An alternative method for computing surface normals (using *surfnorm* on the boundaries produced by *bwboundaries* and *bwtraceboundaries*) was found to be more noisy. Consequently, the method described above was chosen. However, the possibility of noisy surface normals motivated an alternative, surface-normal independent, method to verify the results computed by (6.11). This is described in Section 6.5.1.3.

6.5 Optimal Configuration

6.5.1 Methods

6.5.1.1 Using Surface Normals

For each surface point obtained from the segmentation, and that satisfy $\mathbf{s} \cdot \hat{\mathbf{n}} \geq 0$, the MDS radius r is computed by (6.11). To ensure that this MDS does not collide with any point on the head surface, the corresponding $\mathbf{p}$ is computed using (6.6), assuming $\delta = 0$. If $\mathbf{p} + \mathbf{s} \geq r$ is true over the entire set of all surface points $\mathbf{s}$, no collision occurs, and this configuration is valid. The valid surface point that yields the smallest r is considered optimal. The corresponding $\mathbf{p}$ determines its optimal placement relative to the cochlea.

6.5.1.2 On the Modiolus

For comparison, we also determine the smallest MDS allowable if it is constrained to be on the modiolar axis, as in our prior work. Points are sampled on the modiolar axis at increments of 0.1 mm and represent the set of hypothetical locations for the MDS. At each sampled point, the smallest MDS (of radius r with $\delta = 0$) needed to generate the required magnetic field is computed using (6.5) where $\|\mathbf{p}\|$ is simply the distance from the sampled point to the cochlea. The last step is to perform collision detection at each sampled point to determine if the MDS will collide with any of the surface points on the head. If there are no collisions, then the sampled point is valid. The same condition is applied for collision

detection as in Section 6.5.1.1. The valid point yielding the smallest radius is the smallest MDS allowable for the modiolar configuration.

6.5.1.3 Using Brute Force

To verify the results computed by (6.11), an alternative method that is independent of surface normals is also conducted. The method is identical to that described in Section 6.5.1.2, except that the entire space exterior to the head is uniformly sampled at the resolution of the patient-specific CT scan. Thus for each sampled point, there will be an associated radius r that represents the smallest MDS required to generate $\|\mathbf{B}\|_{min}$ at the cochlea if the MDS were centered at that sampled point. The optimal configuration using this method is the sampled point that yields the smallest r without any collisions.

6.5.2 Results

6.5.2.1 Using Surface Normals

We present in Table 6.2 compiled results over the entire dataset of patients. The optimal location is identified by the distance $\|\mathbf{p}\|$ and the direction from the cochlea to the MDS center. The direction can be expressed compactly by the unit vector $-\hat{\mathbf{p}}$. Recall that $\hat{\mathbf{p}}$ is the unit vector in the opposite direction, i.e., from the MDS center to the cochlea. r and r_m are the computed radii at the optimal and modiolar configurations, respectively. Since the optimal MDS location is associated with a surface point, this is also provided as a distance ($\|\mathbf{s}\|$) and direction ($\hat{\mathbf{s}}$) from the cochlea in Table 6.3. The angle between this surface point and its surface normal (θ) is also listed. All unit vectors assume the RAS convention. At the bottom of both tables are some basic statistics for the entire set.

Across all the patients analyzed, there is a 30 mm range in the distances from the cochlea to the MDS center. This is the most variable of the parameters listed. The optimal MDS placement is mostly lateral-to and slightly anterior-to the cochlea. This is a fortuitous result because the typical approach to the cochlea requires an incision behind the ear [15], making it impractical to position the MDS behind the ear. Our results indicate that the optimal configuration will not interfere with the surgical insertion. There does not seem to be a clear trend for the z-coordinate of the MDS as there seems to be a balance in the instances where the MDS should be placed superior to or inferior to the cochlea. The direction to the optimal surface point tends to be more anterior than the direction to the

MDS center.

6.5.2.2 On the Modiolus

By moving the MDS away from the modiolar configuration, its size can be significantly reduced. For example, in the specific case of P28, as shown in Figure 6.6, the radius is reduced by 50%, resulting in an 8-fold decrease in the volume. If averaged over the whole set (Table 6.2), the radius is reduced by approximately 43%, yielding an approximate 5-fold decrease in the volume of the magnetic sphere. Also, the range and standard deviation in radius values are cut approximately in half in the optimal configuration. There is variability in the side-to-side optimal results within each individual, but in the aggregate, the left and right values were very similar.

6.5.2.3 Using Brute Force

A table of results, similar to Table 6.2, is provided in Table 6.4. With the exception of a few cases, the brute-force search method yielded slightly smaller radii values than the surface-normals method. On the aggregate, however, the surface-normals method yields an average radius of only about 1 mm larger, making it slightly conservative and thus better for our purpose. The main drawback to the brute-force method is that computation times are considerably longer because it typically yields approximately 1000 times more points to examine than the surface-normals method.

6.6 Magnetic Force

In all prior work, the MDS used to generate the magnetic field at the cochlea was assumed to be in the modiolar configuration. One benefit of this configuration is that the magnetic force that could potentially attract the EAT into the basilar membrane was negligible and could be disregarded during the insertion [8]. However, at the optimal configuration, this assumption should be verified since avoiding trauma to the basilar membrane is widely considered vital for hearing preservation [4]. The threshold for puncturing the basilar membrane has been measured to be approximately 42 mN [16]. We compute the worst case and assume that the entire force vector is directed into the basilar membrane. While this is not accurate, it does present a conservative upper bound.

The magnetic force applied to the tip is given by

$$\mathbf{f} = \nabla (\mathbf{B} \cdot \mathbf{m}) = \left[\begin{array}{ccc} \frac{\partial}{\partial x}\mathbf{B} & \frac{\partial}{\partial y}\mathbf{B} & \frac{\partial}{\partial z}\mathbf{B} \end{array} \right]^{\mathbf{T}} \mathbf{m} \tag{6.13}$$

where $\mathbf{B}$ is computed by (6.3) and $\mathbf{m}$ is the dipole moment of the EAT. For a given $\|\mathbf{p}\|$, the largest magnitude and spatial derivative of the field vector occurs along the dipole axis of $\mathbf{M}$ (i.e., where $\mathbf{M}$ and $\mathbf{p}$ are parallel). The maximum possible force magnitude at a given $\|\mathbf{p}\|$ is therefore computed by differentiating $\|\mathbf{B}\|$ with respect to $\|\mathbf{p}\|$, with $\mathbf{M}$ parallel to $\mathbf{p}$, yielding

$$\|\mathbf{f}\| = \left\| \frac{\partial}{\partial \|\mathbf{p}\|} \left(\frac{\mu_0 \|\mathbf{M}\| \|\mathbf{m}\|}{2\pi \|\mathbf{p}\|^3} \right) \right\| = \frac{3\mu_0 \|\mathbf{M}\| \|\mathbf{m}\|}{2\pi \|\mathbf{p}\|^4} \tag{6.14}$$

As a nominal value for $\|\mathbf{m}\|$, we will use the magnets embedded in the EAT in our prior work [6, 7], which has been determined to be 4.73×10^{-5} A·m^2. This represents the combined magnetic dipole for two 0.41-mm-long by 0.25-mm-diameter cylindrical magnets made of grade N52 NdFeB.

At the optimal position, for all cases examined, the maximum magnetic force possible never exceeded 0.31 mN, with an average and standard deviation of 0.267 mN and 0.019 mN, respectively. For comparison, we also compute the maximum magnetic force possible if the MDS were positioned at the modiolar configuration for each patient and found that the average and standard deviation is 0.150 mN and 0.012 mN, respectively. Note that by moving the MDS from the modiolar configuration to the optimal configuration, the maximum possible magnetic force averaged over the set is increased by nearly 80%. In context, however, the force is still over 100 times smaller than what is needed to puncture the basilar membrane. Therefore, it seems reasonable to state that any additional magnetic force that may pull the EAT into the basilar membrane arising from the MDS being moved to the optimal configuration does not truly pose any appreciable risk to the basilar membrane.

6.7 Sensitivity Analysis

Achieving the optimal configuration requires perfect registration of the MDS with respect to the cochlea. A sensitivity analysis to registration, magnetic material properties, and any clearance requirements between the MDS and the patient would be useful. This is motivated by the reality that these factors may reduce the magnetic field generated at

the cochlea and thereby limit the amount of insertion-force reduction that can be achieved with magnetically guided insertions.

For each parameter of interest, using (6.11), r can be solved for over the possible range of the parameter while fixing the remainder of the inputs to their nominal values. With this in mind, we first list the nominal values used by the search method, followed by the range of expected values for the parameters, and conclude with plots that show the sensitivity of r to the input parameters within the range defined.

The nominal value for B_r is 1.465 T, which corresponds to a NdFeB magnet of grade N52. For commercially available magnets from K&J Magnetics (Pipersville, PA), the range of B_r for grades N35–N52 is 1.19–1.465 T.

We chose to use a nominal value of 100 mT for the required magnetic field strength $\|\mathbf{B}\|_{min}$. For the range of $\|\mathbf{B}\|_{min}$, we will explore 80–120 mT.

The nominal value for the gap (δ) was set to 0 mm and describes the situation where the spherical magnet just touches the head. However, the spherical magnet itself will likely be contained in a housing. An existing MDS in our lab, using a 50-mm-diameter N42 NdFeB sphere, has been designed with a 7- mm-thick housing [10]. So if this MDS were to be used, then $\delta = 7$ mm assuming the housing of the MDS touches the head. We will use a range of values from 0–25 mm for δ to conduct the sensitivity analysis.

For parameters $\|\mathbf{s}\|$ and θ, there are no initial nominal values as they are the results of the optimization search. As an alternative, we will consider the optimal surface point as the nominal value of each patient for the purpose of this analysis. $\|\mathbf{s}\|$ and θ for each patient and side are listed in Table 6.2. To determine the range of $\|\mathbf{s}\|$ and θ, we examine the region around the optimal surface point for each patient. We use a 10 mm radius sphere and find all the surface points that are within the boundaries of this sphere (Figure 6.7). All surface points are then aggregated over the entire dataset and yield a histogram that identifies the range of possible values for $\|\mathbf{s}\|$ and θ and where those values are concentrated most (Figure 6.8). We find that both parameters tend to be normally distributed around the averaged optimal surface point. The range of $\|\mathbf{s}\|$ is between 35–65 mm based on the 10 mm registration sphere as described earlier. Then for each patient, all the surface points within this uncertainty sphere are used to compute r using (6.11), and to be conservative, we take the largest radius for each patient (r_{max}) to compute statistics. We find that across

all patients, $59.1 \leq r_{max} \leq 79.1$ mm with an average and standard deviation of 70.8 mm and 4.57 mm, respectively. Note that this does not take into consideration collision checks. It is likely that the lower bound on $\|\mathbf{s}\|$ is not realizable because that would typically imply moving the MDS closer to the ear, which would have resulted in a collision and be regarded as invalid. A case can be made, therefore, that it would be more practical to limit the range of $\|\mathbf{s}\|$ to values that exceed the distance to the optimal surface point. In the sensitivity analysis, including this lower bound requires little additional effort, and so it is provided for completeness.

Sensitivity results are grouped into two categories. The first category represents the effect from the magnetic field desired and the magnetic property of the MDS, as expressed by the nondimensional parameter K. In Figure 6.9-left, we display K over the range of $\|\mathbf{B}\|$ outlined earlier (i.e., 80–120 mT) and the range of magnetic grades commercially available. This range of K is then used to compute the values of r in Figure 6.9-right. This is computed for each patient and each side separately and plotted together on a single graph. We assume the nominal value of δ, $\|\mathbf{s}\|$, and θ for these results.

The second category represents the effect from increasing the clearance between the magnet and the surface of the patient. In Figure 6.10, r is computed as a function of δ over the range defined earlier (i.e., 0–25 mm). This is also computed for each patient and each side separately and plotted together on a single graph. We assume the nominal value of K, $\|\mathbf{s}\|$, and θ for these results.

6.8 Oversized MDS

We now consider the design of a one-size-fits-all MDS for magnetically guided insertions. In order to generate the necessary magnetic field across as many patients as needed, the MDS will need to be oversized for the vast majority of patients. To gain some insight into this, we choose a 75 mm radius MDS. This is only about 1.5 mm larger than the maximum value for r listed in Table 6.2.

All the valid locations generated by the brute-force method for each patient and each side are identified for the oversized MDS. Recall that valid locations are those in which two constraints must be satisfied. First, the MDS centered at this location must be able to generate the required magnetic field at the cochlea. Second, the MDS must not collide with

any part of the patient's head at this location. An example using P28 is provided in Figure 6.11 where every point represents a valid location of the 75 mm oversized MDS. All points that are posterior to the cochlea are shown in red; all points anterior to the cochlea are shown in black. Since the optimal radius for P28 is approximately 59 mm, an MDS whose radius is 75 mm represents a 28% increase in the radius over what is needed. This yields many valid points at which the MDS can be located. In practice, it is best to ignore all the locations that are posterior to the cochlea because the insertion is conducted behind the ear, and placing an MDS anywhere behind the ear is impractical. Further, potential points superior and inferior to the top-most and bottom-most CT slice are ignored since there is not surface data available for collision detection.

Let us define the point cloud that contains all the valid points that are also anterior to the cochlea. We can compute the centroid of this point cloud, $\mathbf{v}$, by averaging these valid points; the results are presented in Table 6.5. Attempting to place the MDS at the centroid will yield a location that is robust (i.e., insensitive) to registration and other errors. In general, the shape of the point cloud also suggests more robustness along the y- and z-directions as compared to the x-direction. In principle, this should not be a problem because the initial alignment of the MDS requires the edge of the MDS to contact the surface of the head. This physical constraint will help enforce the tighter tolerance needed in the x-direction.

6.9 Discussion

In this chapter, we have rigorously described the process by which anyone could determine, on their own, the minimum MDS size and its location for a given patient, and for a given EAT magnet strength and required torque.. For a device maker interested in building an MDS to meet the general population, it might be worthwhile to obtain a larger number of head surfaces to supplement the dataset examined here. For this purpose, our dataset of rendered surface points and surface normals can be available upon request by contacting the corresponding author. While we envision a one-size-fits-all MDS as more practical to a patient-specific MDS, our description of a 75 mm MDS in Section 6.8 should not be construed as a recommendation. First, the dimension was arbitrarily chosen to slightly exceed the maximum r in Table 6.2. It may be more desirable to specify a size from

an average and standard deviation based on a larger population. Second, the results in Section 6.8 assumed no clearance between the head surface and the magnet (i.e., $\delta = 0$) and assumed the nominal value of K. In practice, the available magnetic grade (see Figure 6.9) and the designed housing thickness (see Figure 6.10) might drastically impact the size of the MDS. In addition, we have determined in our prior work [6, 7] that the required magnetic field can vary substantially based on electrode-array models. Therefore, it may even be necessary to have electrode-array-specific MDS models as well. Even the progress toward thinner and more flexible electrode arrays may yield a smaller MDS in the future. Finally, a specific surface-registration tolerance might be preferred by the clinicians. This would require a distribution similar to Figure 6.8 to be performed, and the MDS size would change accordingly. Under these various circumstances, the device maker can either conduct a full optimal configuration analysis (Section 6.5) or use the sensitivity curves in Section 6.7 for their MDS design.

The magnetic guidance strategy works best if both the lumen and modiolar axis are determined for each patient. Fortunately, it is standard practice to include a CT-based radiological assessment as just one part of the complete preoperative medical assessment for cochlear implant candidacy. There is very little reason for not planning patient-specific magnetically guided insertions given the ease in which cochlea segmentation can be done [17]. Further, since software can be implemented to generate a patient-specific head surface (as described in Section 6.4), the method outlined in Section 6.8 can be used to determine a patient-specific centroid location for a one-size-fits-all MDS that is most robust to registration error. Although our work describes this centroid with respect to the cochlea, it can be expressed relative to markers on the patient itself (such as bone anchors [18]). In such a scenario, an image tracker could register the MDS to the centroid location with high accuracy [19].

This procedure can be adjusted if this level of complexity is unwanted. For example, if neither the centroid nor markers on the patient is available, then the MDS can be registered to the patient-specific optimal surface point instead. This point is typically anterior to the ear and between the top and bottom of the ear (see examples in Figure 6.7 and Figure 6.12). A further simplification would be to use to averaged optimal surface point given in Table 6.2. In this scenario, we will simply choose a point on the head surface anterior to the ear,

halfway between the top and bottom of the ear, and as close to the ear canal as possible without collision. This is less robust but it should be adequate because this takes advantage of the large tolerance along the y- and z-directions for placing an oversized MDS (Figure 6.11).

In traditional ear surgery, a large retractor is used to reflect the ear forward so that the surgeon can look inside the area with a microscope. It is possible that this could interfere with the MDS placement. However, since the MDS is intended to be used with an automated electrode-insertion tool, the retractor could be removed since visualizing the facial recess is unnecessary to accomplish automated electrode insertions.

Standard temporal-bone CT protocols start the scan below the mastoid process and end just above the petrous ridge [20]. This effectively yields data sufficient only to render the middle portion of the head, typically including the eyes and nose. With the exception of P28, all CT scans of the patients were done this way. Only the cadaver scans (C1 and C2) included the section below the nose to the shoulder. Fortunately, the optimal magnet size and location likely would not change with more slices. The smallest possible magnet will be located where the distance is shortest to the cochlea, barring collision with the head. In Figure 6.12, we show contour maps of distances from the cochlea to the surface points. In addition, the point where the optimal MDS touches the surface is indicated by a large blue dot.

6.10 Conclusion

A method has been presented to determine the patient-specific configuration (size and location) of a spherical-permanent-magnet dipole-field source, using standard CT temporal bone scans, for magnetically guided cochlear-implant electrode-array insertions. To generate 100 mT at the cochlea, the optimal configuration of the dipole-field source should be lateral-to and slightly anterior-to the cochlea with an approximate radius (mean and standard deviation across patients) of 64 mm and 4.5 mm, respectively. When compared to the configuration assumed in prior work, the optimal location yields a 43% reduction in the dipole-field source's radius and a nearly 5-fold reduction in its volume. Although potential magnetic forces that may direct the tip into the basilar membrane are increased by nearly 80% at the optimal configuration compared to the modiolar configuration, they

are still two orders of magnitude below the threshold needed to puncture the membrane. Sensitivity curves were generated for the minimum radius at the optimal configuration and demonstrate that the optimization is most sensitive to the magnetic field requirement. A one-size-fits-all configuration with a dipole-field source of approximately 75 mm will yield a solution that is robust to registration error.

6.11 Acknowledgements

The authors would like to thank those who provided the datasets used to render the head shapes for this study: Richard H. Wiggins, III, M.D. from the University of Utah's Department of Radiology and Imaging Sciences for providing the anonymous CT patient scans, and the U. S. National Library of Medicine (National Institutes of Health) for providing access to the Visible Human Project. We also acknowledge the University of Utah's Center for High Performance Computing for providing computing resources.

Research reported in this chapter was supported by the National Institute on Deafness and Other Communication Disorders of the National Institutes of Health under Award Number R01DC013168. The content is solely the responsibility of the authors and does not necessarily represent the official views of the National Institutes of Health.

6.12 References

[1] F. G. Zeng, S. Rebscher, W. Harrison, X. Sun, and H. Feng, "Cochlear implants: System design, integration, and evaluation," *IEEE Reviews in Biomed. Eng.*, vol. 1, pp. 115–142, 2008.

[2] P. Wardrop, D. Whinney, S. J. Rebscher, J. T. Roland, Jr., W. Luxford, and P. A. Leake, "A temporal bone study of insertion trauma and intracochlear position of cochlear implant electrodes. I: comparison of Nucleus banded and Nucleus Contour electrodes," *Hear. Res.*, vol. 203, no. 1-2, pp. 54–67, 2005.

[3] M. L. Carlson, C. L.W. Driscoll, R. H. Gifford, and S. O. McMenomey, "Cochlear implantation: current and future device options," *Otolaryngol. Clin. N. America*, vol. 45, no. 1, pp. 221–248, 2012.

[4] G. B. Wanna, J. H. Noble, R. H. Gifford, M. S. Dietrich, A. D. Sweeney, D. Zhang, B. M. Dawant, A. Rivas, and R. F. Labadie, "Impact of intrascalar electrode location, electrode type, and angular insertion depth on residual hearing in cochlear implant patients: Preliminary results.," *Otol. Neurotol.*, vol. 36, no. 8, pp. 1343–1348, Sep 2015.

[5] G. B. Wanna, J. H. Noble, M. L. Carlson, R. H. Gifford, M. S. Dietrich, D. S. Haynes, B. M. Dawant, and R. F. Labadie, "Impact of electrode design and surgical approach on scalar location and cochlear implant outcomes," *Laryngoscope*, 2014.

[6] L. Leon, F. M. Warren, and J. J. Abbott, "An in-vitro insertion-force study of magnetically guided, lateral-wall, cochlear-implant electrodes, part I: Via cochleostomy," *Otol. Neurotol.*, (under review).

[7] L. Leon, F. M. Warren, and J. J. Abbott, "An in-vitro insertion-force study of magnetically guided, lateral-wall, cochlear-implant electrodes, part II: Via the round window," *Otol. Neurotol.*, (under review).

[8] J. R. Clark, L. Leon, F. M. Warren, and J. J. Abbott, "Magnetic guidance of cochlear implants: Proof-of-concept and initial feasibility study," *J. Med. Devices*, vol. 6, no. 3, pp. 035002, 2012.

[9] A. W. Mahoney and J. J. Abbott, "Generating rotating magnetic fields with a single permanent magnet for propulsion of untethered magnetic devices in a lumen," *IEEE Trans. Robotics*, vol. 30, no. 2, pp. 411–420, 2014.

[10] S. E. Wright, A. W. Mahoney, K. M. Popek, and J. J. Abbott, "A spherical-magnet end-effector for robotic magnetic manipulation," in *IEEE Int. Conf. Robotics and Automation*, 2015, pp. 1190–1195.

[11] A. J. Petruska and J. J. Abbott, "Omnimagnet: An omnidirectional electromagnet for controlled dipole-field generation," *IEEE Trans. Magnetics*, vol. 50, no. 7, pp. 8400810, 2014.

[12] L. Leon, M. S. Cavilla, M. B. Doran, F. M. Warren, and J. J. Abbott, "Scala-tympani phantom with cochleostomy and round-window openings for cochlear-implant insertion experiments," *J. Med. Devices*, vol. 8, no. 4, pp. 041010, 2014.

[13] V. Spitzer, M. J. Ackerman, A. L. Scherzinger, and D. Whitlock, "The visible human male: A technical report," *J. Am. Med. Inform. Assoc.*, vol. 3, no. 2, pp. 118, 1996.

[14] J. Xu, S. A. Xu, L. T. Cohen, and G. M. Clark, "Cochlear view: postoperative radiography for cochlear implantation," *Am. J. Otol.*, vol. 21, no. 1, pp. 49–56, 2000.

[15] P. S. Roland, W. Gstöttner, and O. Adunka, "Method for hearing preservation in cochlear implant surgery," *Oper. Tech. Otolaryngol.*, vol. 16, no. 2, pp. 93–100, 2005.

[16] D. Schuster, L. B. Kratchman, and R. F. Labadie, "Characterization of intracochlear rupture forces in fresh human cadaveric cochleae," *Otol. Neurotol.*, Sep 2014.

[17] J. H. Noble, R. F. Labadie, O. Majdani, and B. M. Dawant, "Automatic segmentation of intracochlear anatomy in conventional CT," *IEEE Trans. Biomed. Eng.*, vol. 58, no. 9, pp. 2625–32, Sep 2011.

[18] F. M. Warren, R. Balachandran, J. M. Fitzpatrick, and R. F. Labadie, "Percutaneous cochlear access using bone-mounted, customized drill guides: demonstration of concept in vitro," *Otol. Neurotol.*, vol. 28, no. 3, pp. 325–329, 2007.

[19] T. L. Bruns and R. J. Webster III, "An image guidance system for positioning robotic cochlear implant insertion tools," in *SPIE Medical Imaging*, 2017.

[20] L. E. Romans, *Computed Tomography for Technologists: A Comprehensive Text*, Wollters Kluwer Health - Lippincott Williams & Wilkins, 2010.

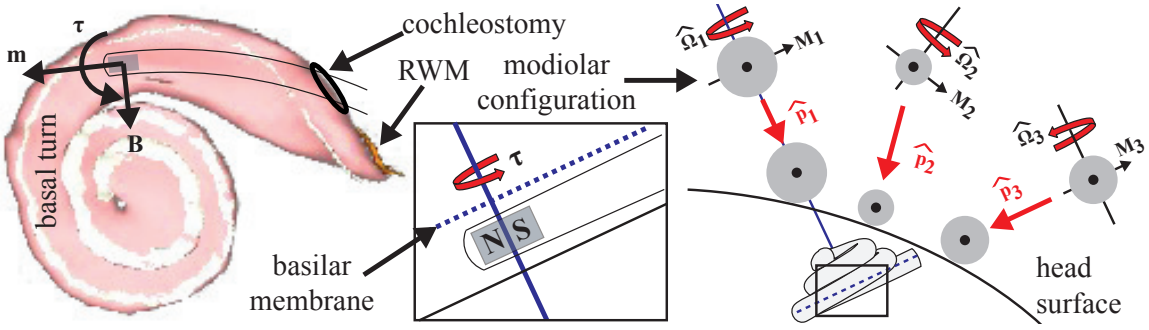

Figure 6.1. Left: Magnetic bending torque ($\boldsymbol{\tau}$) applied to the EAT during insertion is accomplished by a magnetic-field vector (**B**) leading the dipole moment (**m**) by 90°. RWM = Round Window Membrane. Image generated using software provided by Eaton-Peabody Laboratory (Boston, MA). Center: Close-up view of the EAT with its magnet, and the desired bending torque ($\boldsymbol{\tau}$) relative to the basilar membrane. Right: Three hypothetical configurations are presented in which the MDS approaches the patient's head along sample trajectories (red straight arrows) while rotating (red curved arrows) about a fixed axis $\hat{\boldsymbol{\Omega}}$. These trajectories are not the surface normals of the patient's head in general.

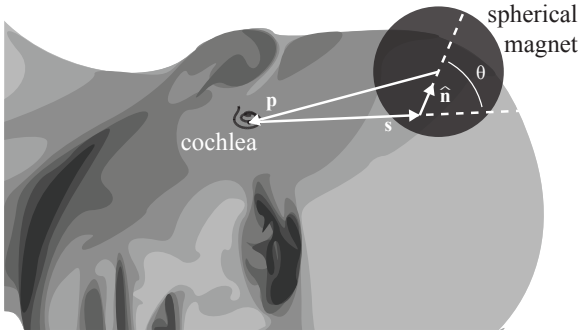

Figure 6.2. Vectors defining an arbitrary surface point (**s**) and its unit surface normal ($\hat{\mathbf{n}}$) with respect to the cochlea. **p** is the vector from the center of the spherical magnet, which is touching the head at **s**, to the cochlea. θ is the angle between **s** and $\hat{\mathbf{n}}$.

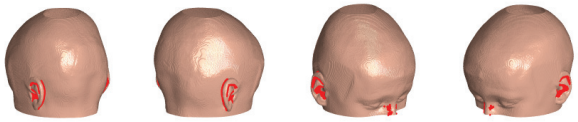

Figure 6.3. Surface rendering of a patient, with red points indicating where $\mathbf{s} \cdot \hat{\mathbf{n}} < 0$ are excluded from the analysis.

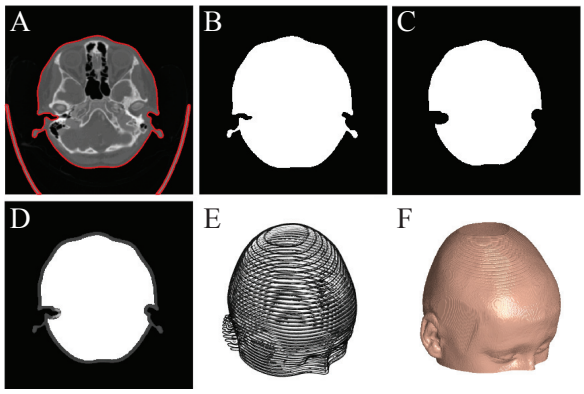

Figure 6.4. Illustration of the main segmentation steps.

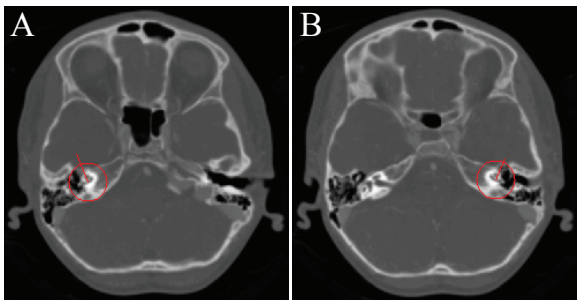

Figure 6.5. The cochlea location and the modiolar axis are identified for the right (A) and left side (B) of each patient.

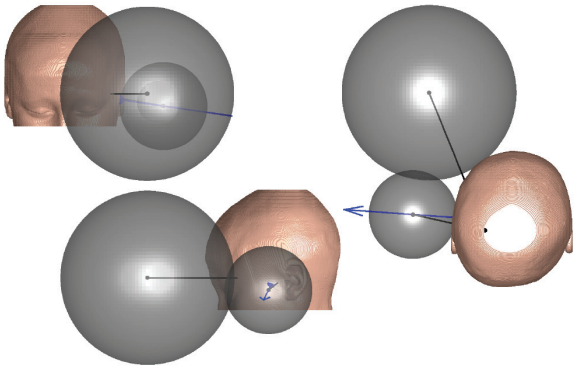

Figure 6.6. The size of the MDS is drastically reduced by moving it away from the modiolar axis to the optimal configuration. Black lines are drawn from the cochlea to the MDS center. Arrows indicate the surface normal at the optimal surface point (blue dot).

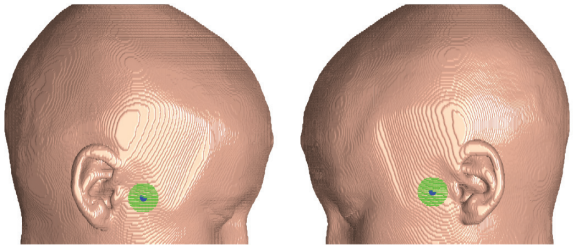

Figure 6.7. All surface points (in green) within 10 mm from the optimal surface point (in blue) for P28.

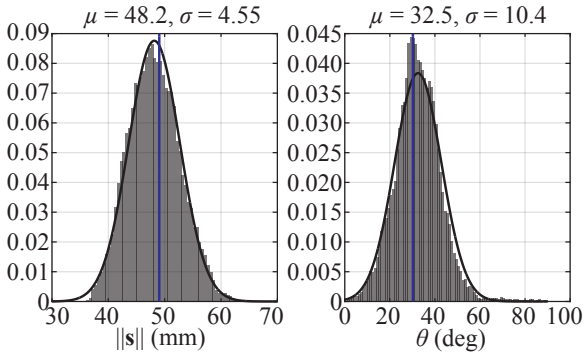

Figure 6.8. Surface points within 10 mm from the optimal surface point of each individual patient are aggregated into histograms and normalized to approximate a probability density function wherein the total bar area is ≤ 1. A normal distribution is fitted to the set with its mean μ and standard deviation σ given above the histograms. The blue vertical lines are the average $\|\mathbf{s}\|$ and θ of Table 6.2 (approximately 49 mm and 30°, respectively).

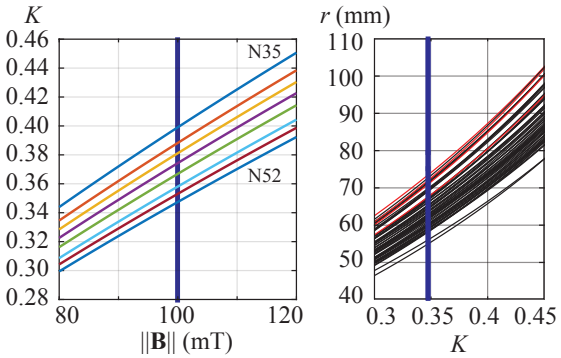

Figure 6.9. Left: Expected range of K given the expectation of $\|\mathbf{B}\|$ and commercially available B_r. The blue vertical line is the nominal value for $\|\mathbf{B}\|$. Right: r as a function of K for all patients analyzed (C1 and C2 results are shown in red). The blue vertical line is the nominal value for K.

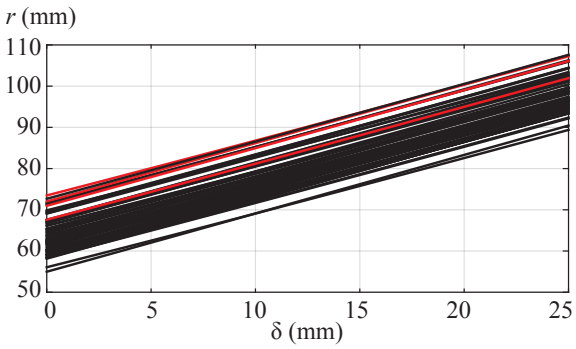

Figure 6.10. r as a function of δ for all patients analyzed (C1 and C2 results are shown in red).

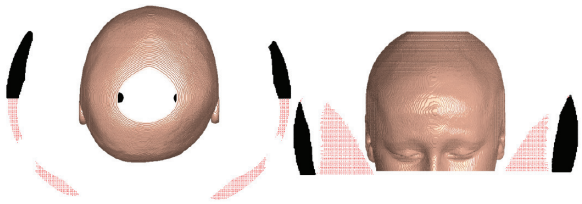

Figure 6.11. All valid locations to place an MDS that has been oversized to 75 mm radius. For P28, this represents a 28% increase in the radius over what is actually needed. Black points are anterior to the cochlea. Red points are posterior to the cochlea. The black circles inside the head (left) locate the cochlea

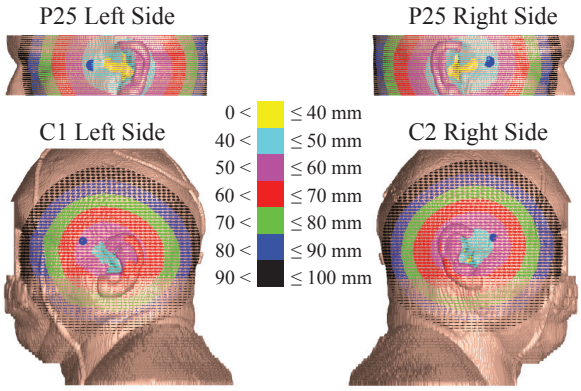

Figure 6.12. Contour map of $\|\mathbf{s}\|$ for P25 and C1. Blue dot indicates where the optimal MDS touches the surface of the head.

Table 6.1. Summary of database used to generate patient-specific head surfaces. P1–P28 are scans of anonymous patients provided by the University of Utah (UU). C1–C2 are scans of cadavers obtained from the National Library of Medicine (NLM).

ID	Gender (M/F)	Age (yrs)	Source	Resolution (mm)		Total Slices
				Pixel	Slice	
P1	F	62	UU	0.41	0.6	89
P2	F	52	UU	0.41	2	39
P3	F	33	UU	0.41	2	37
P4	F	60	UU	0.41	2	37
P5	M	26	UU	0.44	5	16
P6	F	42	UU	0.41	2	30
P7	F	85	UU	0.41	4	16
P8	F	21	UU	0.39	5	15
P9	F	32	UU	0.41	5	15
P10	F	65	UU	0.47	0.6	115
P11	F	39	UU	0.49	3	23
P12	M	48	UU	0.44	2	39
P13	F	51	UU	0.43	1	68
P14	M	64	UU	0.46	5	17
P15	F	47	UU	0.34	2	25
P16	M	79	UU	0.59	2	36
P17	F	48	UU	0.43	2	33
P18	F	52	UU	0.33	0.7	82
P19	F	29	UU	0.57	2	32
P20	F	39	UU	0.41	2	31
P21	F	37	UU	0.59	2	36
P22	F	36	UU	0.38	5	12
P23	F	60	UU	0.41	0.6	98
P24	M	36	UU	0.46	2	31
P25	F	67	UU	0.39	1	78
P26	M	83	UU	0.41	1	47
P27	F	44	UU	0.32	2	31
P28	M	8	UU	0.45	1	161
C1	M	–	NLM	0.79	1.45	183
C2	F	–	NLM	0.54	1	249

Table 6.2. Optimal configuration of the MDS as defined by its radius (r) and location relative to the cochlea ($\mathbf{p}$). Vectors are expressed in the RAS convention where $+x$ is directed to the person's right side, $+y$ is directed anteriorly, and $+z$ is directed superiorly. The MDS radius at the modiolar configuration (r_m) is provided for comparison. Units are in {mm} except for the unitless direction vector $-\hat{\mathbf{p}} = -\left[\hat{p}_x\ \hat{p}_y\ \hat{p}_z\right]^T$ from the cochlea toward the MDS center.

	Left Side						Right Side					
ID	$\|\mathbf{p}\|$	$-[\hat{p}_x$	$\hat{p}_y$	$\hat{p}_z]^{\mathrm{T}}$	r	r_m	$\|\mathbf{p}\|$	$-[\hat{p}_x$	$\hat{p}_y$	$\hat{p}_z]^{\mathrm{T}}$	r	r_m
P1	101	[-0.95	0.31	-0.10]	59.6	109	106	[0.92	0.31	-0.22]	62.4	102
P2	117	[-0.91	0.38	-0.15]	69.1	94.1	114	[0.94	0.30	0.15]	67.1	113
P3	113	[-0.99	0.13	-0.06]	66.8	127	104	[0.99	0.13	-0.07]	61.2	119
P4	106	[-0.95	0.30	0.06]	62.7	97.6	107	[0.97	0.22	-0.08]	62.8	105
P5	121	[-1.00	0.09	-0.02]	71.3	125	111	[0.98	0.16	0.12]	65.1	105
P6	106	[-0.93	0.35	-0.12]	62.2	131	108	[0.93	0.34	-0.13]	63.5	105
P7	113	[-0.97	0.22	0.11]	66.7	114	114	[0.99	0.14	0.10]	67.4	103
P8	108	[-0.94	0.28	-0.21]	63.9	115	105	[0.94	0.32	-0.10]	61.9	115
P9	106	[-0.97	0.21	-0.12]	62.4	103	100	[0.96	0.23	-0.15]	59.0	117
P10	105	[-0.93	0.36	0.11]	61.6	118	112	[0.88	0.47	0.03]	66.2	121
P11	114	[-0.97	0.19	0.13]	67.1	113	115	[0.98	0.12	0.15]	67.5	116
P12	119	[-0.93	0.31	0.21]	69.9	107	121	[0.98	0.19	-0.09]	71.4	107
P13	117	[-0.95	0.31	-0.07]	69.1	109	111	[0.96	0.25	-0.13]	65.3	114
P14	122	[-0.91	0.41	0.05]	71.7	109	118	[0.92	0.34	-0.17]	69.4	113
P15	102	[-0.98	0.18	-0.08]	60.4	98.0	93.3	[1.00	0.04	-0.08]	55.0	99.1
P16	106	[-0.92	0.40	-0.06]	62.2	132	109	[0.91	0.40	-0.10]	64.3	117
P17	102	[-0.94	0.24	-0.25]	60.3	110	99.3	[0.95	0.26	-0.19]	58.5	100
P18	102	[-0.96	0.26	-0.06]	60.3	114	102	[0.97	0.24	-0.10]	60.0	116
P19	118	[-0.97	0.17	0.15]	69.6	109	123	[0.97	0.19	0.16]	72.7	118
P20	110	[-0.94	0.28	-0.21]	64.5	105	112	[0.94	0.28	-0.19]	66.1	121
P21	95.1	[-0.95	0.24	-0.18]	56.1	97.3	101	[0.95	0.30	0.01]	59.8	105
P22	107	[-0.96	0.24	-0.15]	63.0	113	110	[0.90	0.42	-0.09]	64.8	115
P23	108	[-0.98	0.16	-0.11]	63.6	115	111	[0.98	0.20	0.00]	65.4	117
P24	100	[-0.96	0.29	-0.02]	59.1	112	100	[0.95	0.32	-0.02]	59.2	121
P25	99.0	[-0.91	0.41	0.04]	58.4	96.5	98.6	[0.96	0.27	-0.01]	58.1	110
P26	103	[-0.98	0.11	-0.15]	60.8	128	102	[0.97	0.23	0.02]	60.2	131
P27	105	[-0.95	0.32	0.04]	61.6	106	105	[0.94	0.33	0.00]	61.9	113
P28	98.9	[-0.96	0.21	-0.17]	58.3	115	100	[0.97	0.15	-0.17]	58.9	124
C1	125	[-0.97	0.21	0.08]	73.5	114	115	[0.97	0.19	0.12]	67.6	114
C2	122	[-0.98	0.21	0.02]	72.0	114	120	[0.98	0.17	-0.11]	71.0	109
Min	95.1				56.1	94.1	93.3				55.0	99.1
Max	125				73.5	132	123				72.7	131
Range	29.6				17.4	37.6	30.0				17.7	31.9
Avg	109	[-0.96	0.26	-0.04]	64.3	112	108	[0.97	0.25	-0.04]	63.8	113
Std	8.05	[0.13	0.59	0.79]	4.75	10.0	7.45	[0.20	0.66	0.73]	4.39	7.58

Table 6.3. The optimal surface point associated with the optimal MDS configuration of Table 6.2 is defined by **s**. Vectors are expressed in the RAS convention where $+x$ is directed to the person's right side, $+y$ is directed anteriorly, and $+z$ is directed superiorly. Units are in {mm} except for θ in degrees and the unitless direction vector $\hat{\mathbf{s}} = \left[\hat{s}_x\ \hat{s}_y\ \hat{s}_z\right]^T$ from the cochlea toward the optimal surface point.

	Left Side					Right Side				
ID	$\|\mathbf{s}\|$	$[s_x$	s_y	$s_z]^{\mathrm{T}}$	θ	$\|\mathbf{s}\|$	$[s_x$	s_y	$s_z]^{\mathrm{T}}$	θ
P1	46.5	[-0.78	0.59	-0.22]	35.7	52.3	[0.70	0.68	-0.23]	45.5
P2	50.2	[-0.80	0.56	-0.21]	21.7	51.1	[0.80	0.58	0.18]	31.7
P3	49.4	[-0.93	0.25	-0.28]	25.8	48.3	[0.89	0.46	0.05]	37.5
P4	47.6	[-0.82	0.56	0.13]	30.8	47.9	[0.86	0.51	-0.08]	31.8
P5	52.1	[-0.95	0.22	-0.21]	23.4	49.6	[0.89	0.14	0.42]	31.6
P6	48.9	[-0.74	0.65	-0.16]	36.7	49.4	[0.75	0.61	-0.24]	35.1
P7	47.7	[-0.94	0.34	-0.02]	17.2	48.8	[0.98	0.19	-0.10]	20.5
P8	52.4	[-0.72	0.58	-0.38]	42.8	51.0	[0.73	0.66	-0.20]	43.3
P9	47.9	[-0.85	0.39	-0.36]	33.0	44.5	[0.84	0.46	-0.28]	29.8
P10	47.9	[-0.75	0.65	0.13]	35.1	53.0	[0.65	0.76	0.10]	39.3
P11	52.1	[-0.84	0.46	0.29]	34.7	49.7	[0.90	0.23	0.36]	24.7
P12	56.4	[-0.73	0.45	0.52]	40.7	53.3	[0.89	0.31	-0.32]	27.8
P13	52.5	[-0.81	0.56	-0.17]	31.3	47.7	[0.89	0.32	-0.34]	22.7
P14	54.9	[-0.73	0.68	0.09]	32.3	50.9	[0.84	0.37	-0.39]	23.8
P15	44.6	[-0.90	0.34	-0.27]	25.5	39.4	[0.96	0.17	-0.20]	17.5
P16	48.3	[-0.73	0.68	-0.06]	34.8	47.9	[0.77	0.61	-0.19]	27.3
P17	47.3	[-0.76	0.49	-0.42]	36.5	45.9	[0.77	0.53	-0.35]	36.4
P18	46.8	[-0.82	0.57	-0.11]	34.8	47.4	[0.81	0.55	-0.19]	37.6
P19	51.7	[-0.92	0.39	0.01]	26.5	53.5	[0.88	0.42	0.22]	24.9
P20	51.2	[-0.77	0.61	-0.17]	37.9	52.7	[0.77	0.61	-0.18]	38.9
P21	45.3	[-0.79	0.60	-0.16]	40.6	47.5	[0.78	0.63	0.03]	38.2
P22	44.9	[-0.91	0.28	-0.30]	16.3	51.1	[0.69	0.71	-0.12]	37.2
P23	46.2	[-0.93	0.19	-0.32]	21.6	50.0	[0.87	0.48	-0.10]	32.1
P24	45.3	[-0.81	0.58	-0.04]	32.5	45.3	[0.80	0.59	0.04]	32.3
P25	45.9	[-0.71	0.70	0.09]	36.7	41.6	[0.95	0.24	-0.18]	16.9
P26	43.2	[-0.94	0.20	-0.27]	15.1	44.2	[0.89	0.43	0.13]	24.3
P27	45.7	[-0.88	0.43	-0.19]	26.3	48.6	[0.77	0.64	-0.04]	36.5
P28	42.1	[-0.90	0.40	-0.19]	20.0	44.5	[0.88	0.43	-0.20]	29.9
C1	57.4	[-0.84	0.51	0.21]	35.8	51.4	[0.86	0.44	0.25]	31.3
C2	51.3	[-0.93	0.37	0.04]	15.8	51.6	[0.92	0.25	-0.31]	22.0
Min	42.1				15.1	39.4				16.9
Max	57.4				42.8	53.5				45.5
Range	15.3				27.6	14.2				28.6
Avg	48.8	[-0.86	0.50	-0.10]	29.9	48.7	[0.87	0.49	-0.08]	30.9
Std	3.78	[0.29	0.54	0.79]	8.07	3.49	[0.28	0.59	0.76]	7.41

Table 6.4. Optimal configuration of MDS as defined by its radius (r) and its location relative to the cochlea ($\mathbf{p}$), using the brute-force method. Vectors are expressed in the RAS convention where $+x$ is directed to the person's right side, $+y$ is directed anteriorly, and $+z$ is directed superiorly. Units are in {mm} except for the unitless direction vector $-\hat{\mathbf{p}} = -\left[\hat{p}_x\ \hat{p}_y\ \hat{p}_z\right]^T$ from the cochlea toward the MDS center.

	Left					Right				
ID	$\|\mathbf{p}\|$	$-[\hat{p}_x$	$\hat{p}_y$	$\hat{p}_z]^{\mathrm{T}}$	r	$\|\mathbf{p}\|$	$-[\hat{p}_x$	$\hat{p}_y$	$\hat{p}_z]^{\mathrm{T}}$	r
P1	100	[-0.96	0.28	-0.08]	58.8	100	[0.95	0.28	-0.13]	59.1
P2	112	[-0.95	0.32	0.00]	65.8	114	[0.94	0.30	0.14]	67.1
P3	112	[-0.99	0.12	-0.04]	66.1	103	[0.99	0.12	-0.09]	60.8
P4	105	[-0.96	0.28	0.04]	62.1	106	[0.98	0.20	-0.09]	62.7
P5	120	[-0.99	0.11	0.04]	70.9	109	[0.99	0.13	0.09]	64.3
P6	103	[-0.94	0.29	-0.17]	60.9	105	[0.96	0.23	-0.17]	61.6
P7	113	[-0.98	0.17	0.14]	66.4	112	[0.97	0.14	0.18]	66.1
P8	105	[-0.93	0.16	-0.33]	62.1	104	[0.93	0.17	-0.34]	61.5
P9	105	[-0.98	0.18	-0.12]	62.0	100	[0.96	0.22	-0.17]	59.0
P10	104	[-0.94	0.34	0.08]	61.4	100	[0.95	0.29	0.06]	58.8
P11	113	[-0.98	0.15	0.11]	66.8	113	[0.99	0.07	0.08]	66.7
P12	111	[-0.96	0.26	0.07]	65.6	114	[0.96	0.26	0.07]	67.1
P13	117	[-0.96	0.27	-0.11]	68.8	109	[0.96	0.26	-0.09]	64.5
P14	117	[-0.94	0.31	-0.13]	69.0	117	[0.93	0.34	-0.13]	68.9
P15	102	[-0.98	0.05	-0.18]	60.4	93.1	[1.00	0.08	-0.02]	54.9
P16	104	[-0.93	0.37	-0.06]	61.1	110	[0.92	0.38	-0.10]	64.6
P17	101	[-0.95	0.21	-0.22]	59.4	97.4	[0.96	0.21	-0.21]	57.4
P18	101	[-0.96	0.23	-0.13]	59.7	101	[0.97	0.19	-0.16]	59.5
P19	118	[-0.99	0.14	0.08]	69.8	123	[0.98	0.18	0.13]	72.2
P20	109	[-0.94	0.26	-0.20]	64.0	110	[0.96	0.24	-0.15]	64.8
P21	94.9	[-0.96	0.22	-0.19]	55.9	97.2	[0.95	0.21	-0.23]	57.3
P22	105	[-0.95	0.32	0.01]	62.1	102	[0.94	0.31	-0.12]	60.2
P23	103	[-0.99	0.14	-0.01]	61.0	108	[0.99	0.14	-0.03]	63.9
P24	100	[-0.96	0.28	-0.02]	59.1	101	[0.95	0.31	-0.04]	59.3
P25	94.4	[-0.94	0.35	-0.03]	55.7	97.5	[0.95	0.31	0.02]	57.5
P26	102	[-0.98	0.18	-0.07]	60.4	101	[0.98	0.21	0.01]	59.6
P27	104	[-0.95	0.30	0.06]	61.0	101	[0.96	0.28	0.08]	59.4
P28	97.9	[-0.97	0.16	-0.16]	57.7	99.2	[0.98	0.13	-0.16]	58.5
C1	123	[-0.98	0.20	0.03]	72.7	114	[0.99	0.15	0.07]	67.5
C2	122	[-0.98	0.18	-0.02]	71.9	119	[0.99	0.10	-0.11]	70.2
Min	94.4				55.7	93.1				54.9
Max	123				72.7	123				72.2
Rng	28.9				17.1	29.4				17.4
Avg	107	[-0.97	0.23	-0.05]	63.3	106	[0.98	0.21	-0.05]	62.5
Std	7.89	[0.15	0.58	0.80]	4.65	7.40	[0.13	0.52	0.84]	4.36

Table 6.5. Placement, relative to the cochlea, of an MDS oversized to 75 mm radius. Vectors are expressed in the RAS convention. The values represent the centroid of all the valid points anterior to the cochlea where the oversized MDS can be placed without collision and satisfy the magnetic field requirement. Units are in mm except for the unitless direction vector $\hat{\mathbf{v}} = \left[\hat{v}_x\ \hat{v}_y\ \hat{v}_z\right]^T$.

	Left				Right			
ID	$\|\mathbf{v}\|$	$[v_x$	v_y	$v_z]^T$	$\|\mathbf{v}\|$	$[v_x$	v_y	$v_z]^T$
P1	122	[-0.95	0.32	-0.03]	122	[0.96	0.29	-0.04]
P2	124	[-0.94	0.33	-0.01]	124	[0.95	0.29	0.08]
P3	125	[-0.99	0.16	-0.03]	123	[0.98	0.17	-0.08]
P4	123	[-0.96	0.29	0.01]	123	[0.97	0.24	-0.06]
P5	126	[-0.99	0.12	0.04]	124	[0.98	0.20	0.05]
P6	122	[-0.94	0.31	-0.11]	122	[0.95	0.30	-0.08]
P7	124	[-0.98	0.20	0.03]	124	[0.98	0.20	0.05]
P8	122	[-0.97	0.24	-0.08]	121	[0.97	0.23	-0.05]
P9	122	[-0.98	0.21	-0.03]	121	[0.97	0.24	-0.05]
P10	122	[-0.92	0.39	0.01]	121	[0.95	0.32	0.02]
P11	125	[-0.98	0.15	0.09]	125	[0.99	0.13	0.11]
P12	124	[-0.96	0.26	0.04]	125	[0.97	0.24	0.03]
P13	125	[-0.96	0.27	-0.09]	123	[0.95	0.31	-0.09]
P14	125	[-0.94	0.34	-0.08]	125	[0.93	0.36	-0.10]
P15	122	[-0.97	0.21	-0.08]	120	[0.97	0.22	-0.07]
P16	123	[-0.92	0.39	-0.03]	124	[0.91	0.40	-0.10]
P17	122	[-0.96	0.26	-0.10]	121	[0.96	0.28	-0.08]
P18	121	[-0.97	0.23	-0.06]	121	[0.98	0.20	-0.07]
P19	125	[-0.98	0.16	0.11]	126	[0.98	0.17	0.11]
P20	124	[-0.95	0.28	-0.13]	124	[0.96	0.24	-0.13]
P21	121	[-0.97	0.25	-0.02]	121	[0.96	0.28	-0.01]
P22	122	[-0.95	0.30	-0.05]	122	[0.95	0.32	-0.05]
P23	123	[-0.97	0.23	-0.05]	124	[0.98	0.20	-0.04]
P24	121	[-0.95	0.31	-0.03]	121	[0.94	0.33	-0.04]
P25	120	[-0.93	0.35	-0.04]	121	[0.95	0.31	-0.02]
P26	122	[-0.98	0.20	-0.05]	121	[0.97	0.23	-0.02]
P27	122	[-0.96	0.27	-0.01]	121	[0.96	0.27	0.00]
P28	120	[-0.97	0.24	-0.07]	121	[0.98	0.20	-0.10]
C1	127	[-0.98	0.17	0.04]	125	[0.98	0.15	0.11]
C2	126	[-0.98	0.19	0.01]	125	[0.98	0.18	-0.05]
Min	120				120			
Max	127				126			
Rng	6.44				6.04			
Avg	123	[-0.96	0.26	-0.03]	123	[0.97	0.25	-0.03]
Std	1.74	[0.21	0.74	0.64]	1.68	[0.21	0.64	0.74]

CHAPTER 7

RECOMMENDATIONS FOR FUTURE WORK

This chapter summarizes possible research directions based on the results of this dissertation. All topics presented remain within the theme of magnetics applied to cochlear implantation.

7.1 Customized Electrode Arrays

With the exception of the 3-to-1 scale dummy electrode used in our initial proof-of-concept experiments [1], the electrodes used in these studies were existing lateral-wall-type clinical versions that have been slightly modified at the tip. The electrode is placed in a mold with the magnet near the tip and silicone rubber is used to encapsulate the magnet to the electrode tip. The fabrication process is repeatable and can be performed on any lateral-wall-type electrode. This approach is desirable in that it provides a clear path to adoption.

However, electrodes specifically designed for magnetic guidance may yield better results. For example, current electrodes have a tapered thickness wherein the tip is thinner than the base. This is intended to prevent buckling of the electrode. It is possible that buckling occurs primarily when the tip of the electrode "digs" into the lateral wall and prevents the electrode from further sliding. The surgeon, not detecting this, continues to insert the electrode, which initiates the buckling action. By providing a thicker base, the electrode tip has a better chance to progress through this "sticky" section before the remainder of the electrode buckles. In our method, since the tip is always directed away from the lateral wall, it may allow thinner electrodes to be inserted, perhaps even enabling smaller, more minimally invasive cochleostomies.

In addition, the tapered thickness yields an electrode that is more flexible at the tip than at the base. The application of magnetic bending torque to the tip does not yield an equally distributed curling action on the electrode body. It is clear from the results in Sections 4.4

and 5.4 that the majority of the curling action is localized near the tip. Although it makes bending the tip away from the lateral wall easier to accomplish, curling the entire electrode body is more difficult to achieve. Based on first principles, it seems reasonable to expect greater reduction of insertion forces if the bending torque can be more distributed across the entire length, and thus reduce more of the total pressure distributed over the lateral wall. This would require the electrode to be redesigned to have a more uniform stiffness throughout the entire length of the body.

Since the electrode is steered at the distal tip, this may finally allow the use of ultra-flexible electrodes. This is similar in concept to steerable, highly flexible catheters pioneered by Stereotaxis (St. Louis, MO) for surgical applications. Their units generate desired magnetic field vectors to which the distal magnetic catheter tip will align itself. By changing the direction of the field vector, the tip can be directed in any orientation needed, and by implementing this approach with highly flexible catheters, their surgical tools can be navigated through very tight corners.

For these reasons, it seems worthwhile to examine the optimal electrode stiffness that will maximize the benefit of using magnetic guidance. To determine an optimal uniform stiffness, the electrode could be modeled as a beam where the angular deflection at the tip is a function of the bending torque applied to the tip and the angular spring constant of the beam. A path planning approach can be used to map the configuration space of the electrode (i.e., bending torque, angular spring constant, and insertion depth) to the tip position inside the scala-tympani channel. Collision detection would then determine if the specific configuration results in the tip touching the cochlear wall. There may be a range of angular spring constants, for a range of input torques, that yield no collisions throughout the insertion. Further, an optimization search could be used to determine the optimal angular spring constant based on certain metrics such as lowest input torque or largest gap between the tip and the cochlear walls.

A similar approach can also be conducted to determine the optimal graded stiffness along the length of the electrode body. The electrode can be modeled as a planar manipulator with n links rather than a beam of uniform stiffness. The configuration space will increase from 3 parameters to $2 + n$ parameters. Although a large n would, in principle, yield better resolution, collaboration with a device maker is suggested since there are

limitations to what can be achieved. This process could yield the ideal stiffness in each of the linkages (i.e., electrode sections) to best navigate through the lumen based on a single bending torque applied to the tip.

7.2 Complete Insertions

As indicated earlier in Section 7.1, it is possible that the resistance is due to the tip "digging" into the lateral wall. Although buckling may occur if the insertion is not stopped, a far worse outcome is that the tip may fracture the spiral ligament since this organ lies on the lateral wall of the cochlea [2]. Therefore, a recommended protocol is to halt the electrode insertion at the first sign of resistance [3]. Adherence to this protocol, however, may yield incomplete insertions of the electrode, rendering some of the contacts useless. Occurences of complete insertions might increase in practice by directing the tip away from the lateral wall, which our strategy can achieve.

To test this hypothesis, the insertion-force threshold in which surgeons will likely halt manual electrode insertions should be determined. This can be conducted with either cadaver cochleae or a scala-tympani proxy mounted to a force sensor. Since the patient's scala-tympani channel is not visible to the surgeon during the insertions, the proxy should not be transparent so as not to provide visualization of the electrode inside the channel. Force measurements would be recorded during the manual insertion. If the insertion is halted prematurely, the maximum force measured would be considered the force threshold that would halt the insertion. The insertion depth would be determined by the number of electrodes that were actually inserted into the cadaver cochleae or the nontransparent proxy. The results can be aggregated over the sampled population to determine the average threshold that would halt the manual insertion and the average insertion depth actually achieved with this manual protocol. Then for comparison, magnetically guided insertions can be conducted to obtain the insertion forces per insertion depth. It is conceivable that the threshold is never exceeded using magnetic guidance. It is also possible that the use of magnetic guidance will yield an insertion-force profile where the threshold is exceeded but at a deeper insertion point compared to manual insertions. If either case is true, the strategies outlined in this dissertation would yield more consistently complete insertions than the current manual-insertion protocol.

7.3 Dynamic Magnetic Guidance

The entirety of this disseration has assumed knowledge of the cochlea lumen in advance. In the clinic, this can be implemented through segmentation of the cochlea prior to surgery [4]. The complexity of guided insertions would decrease significantly if insertions could be accomplished completely blind (i.e., without any prior knowledge of the lumen).

One method is to continually rotate the field vector on the basal plane so that the tip wiggles during insertion. It is likely that the behavior of the electrode tip, and perhaps the electrode body, will be dependent on the frequency of the rotating magnetic field vector. By exploiting the natural resonance of the electrode, it may be possible to generate substantial dynamic wiggling with much smaller magnets at the electrode tip or with a smaller magnetic dipole-field source. However, because the scala-tympani is filled with fluid, this type of behavior may create significant churn in the fluid, and to our knowledge, there are no existing studies that determine physiological effects from agitating this fluid.

It is unlikely that there will be a large difference in insertion forces because the electrode body is not being curled away from the lateral wall. Therefore, the decrease in the pressure distributed across the lateral wall will not be as pronounced as in the method described in this dissertation that causes a bulk deformation of the electrode. Still, this technique may induce enough wiggling to prevent the tip from "digging" into the lateral wall. It may also reduce the accumulated friction between the electrode body and the cochlear walls to enable a smoother insertion, eliminating large spikes in the insertion force.

It may be more convenient to use an electromagnetic field source to implement this strategy, especially if the vibration, by exploiting the electrode's natural resonance, enables the use of much smaller magnetic fields. Further, the optimal vibration frequency may be insertion-depth dependent, and the frequency of the rotating field can be more conveniently generated by an electromagnetic-field source rather than a permanent magnet that must be rotated using a mechanical actuator, especially if higher frequencies are needed. A further benefit is that the electromagnetic-field source could be switched off, making it safer to store or transport in the clinic.

If it is determined from experiments using dynamic magnetic guidance that there is actually one optimal vibration frequency throughout the entirety of the insertion, then the implementation of this strategy in the clinic can be simplified even further. The same effect

may be achieved by designing a vibrating element, tuned for the optimal frequency, into the insertion tool that grips the proximal end of the electrode, provided the vibration is sufficiently coupled into the electrode body. That is, vibration at the proximal end should propagate to the distal end of the electrode and cause a random motion of the tip that might prevent it from "digging" into the lateral wall.

7.4 Force-controlled Insertions

Since perforation of the basilar membrane is a strong predictor for permanent loss of residual hearing [5], implementing automated force-control strategies may be the key to eliminating this type of trauma. In recent work [6], researchers have successfully implemented a force sensor at the tip of a prototype electrode and have verified its effectiveness in guinea pig cochlea *in vivo*. It is unclear, however, if these sensors are magnetically insensitive or can be packaged alongside the necessary magnet at the electrode tip.

In the meantime, a force sensor can be placed at the proximal end of the electrode and used as sensor feedback for force-controlled insertion strategies. The challenge of using a force sensor at the proximal end is that any attractive force applied by the magnetic dipole-field source on the electrode tip, pulling it into the basilar membrane, is not fully detected at the proximal end because the basilar membrane provides an opposing force unless it punctures. Thus, a force sensor at the proximal end will underestimate forces in the direction of the basilar membrane. Since the largest possible attractive magnetic force into the basilar membrane, determined in Chapter 6, was two orders of magnitude less than the puncture threshold of the basilar membrane, this undetectable force component is likely to be a very small percentage of the total insertion forces measured.

Very little research has been done to correlate possible real-time force signatures with the type of contact made between the electrode and the cochlea, particularly signatures that would predict basilar membrane puncture [7] or tip-foldover [8]. Since not all contact between the electrode and the cochlear walls are equally detrimental, simply using the total insertion force measured as a metric for force-controlled insertions may not yield the best results. Force data could be collected where specific types of electrode-to-cochlea contact are made with susbsequent analysis to identify, if any, specific force signatures. If this can be discovered, then unique force-control algorithms could be developed to deal

with specific trauma probabilities as they are encountered *in vivo*.

7.5 Passive Protection of the Basilar Membrane

The magnetic field is generated at the cochlea such that its field vector lies on the basal plane of the cochlea and orthogonal to the cochlear axis. From first principles, if the tip is deflected away from the plane in which the magnetic field vector exists, there will be a magnetic torque that will attempt to bring the tip back onto this plane. Therefore, any tip deflection toward the basilar membrane (and away from the cochlea's basal plane) will be met with a passive magnetic spring that attempts to pull the tip away from the basilar membrane and back onto the basal plane.

If this hypothesis can be demonstrated, this would represent a major advantage of using magnetic guidance since there are no existing strategies that can provide this type of passive protection of the basilar membrane. So to test this hypothesis, a scala-tympani phantom equipped with a sensor that measures forces orthogonal to the basal plane could be used. The phantoms described in Chapter 3 would need to be redesigned as an open-channel version with only one full spiral revolution. Then at the open side of the channel, a force sensor could be placed to act as a kind of roof to the open channel. Any force directed into the roof would represent a force into the basilar membrane.

Nonguided insertions would first be conducted to determine the amount of force into the basilar membrane as a baseline for typical insertions. Then magnetically guided insertions would be conducted to determine if there is any change in the insertion force directed into the basilar membrane.

7.6 Applications for Perimodiolar Placement

In this dissertation, all electrodes used were of the lateral-wall-type version, which have been designed to rest on the cochlea's lateral wall after the insertion. The other type of electrodes used in the clinic, known as perimodiolar electrodes, are designed to rest on the medial wall of the cochlea due to their preformed curvature. Prior to insertion, they are initially straightened with a stylet, and the electrode-stylet combination is inserted together. Then the electrode, as it is advanced off the stylet, regains its precurved shape, allowing it rest on the cochlea's medial wall, close to the modiolus. A problem is that

the stylet, which is inserted along with the electrode, increases the overall thickness of the electrode while reducing its flexibility. This is known to be problematic for round-window insertions [9–11]. Since the primary purpose of the stylet is to straighten out the electrode prior to insertion, the use of magnetic guidance can potentially replace the stylet if the bending torque is able to uncurl the perimodiolar electrode during the initial part of the insertion. This would facilitate the development of thinner perimodiolar electrodes to be feasibly used.

Another strategy to achieve a final position that is closer to the modiolus, without using perimodiolar electrodes, would be to embed a Nitinol wire through the center of a lateral-wall-type electrode [12]. By shape-setting the Nitinol to the shape of the cochlear spiral, the electrode could be curled toward the medial wall after the insertion is completed. This is typically done by applying heat to the Nitinol and would require thermal analysis to verify safety inside the cochlea. A second challenge is that if the electrode is misaligned, the Nitinol may curl the tip into the basilar membrane rather than curl toward the medial wall as intended. A third challenge is that the use of Nitinol will likely increase the electrode stiffness, making it less safe than the lateral-wall-type electrodes currently used in the clinic. This added hazard could be overcome by using magnetic guidance to curl the electrode away from the lateral wall and preventing the stiffer electrode from directly impinging on the lateral wall. To compensate for the additional electrode stiffness, a larger magnetic dipole-field source might be needed to accomplish this.

7.7 Real-time Sensing

One of the challenges in cochlear implantation is determining the opening through which the electrode is inserted. It can be difficult to visualize the round-window membrane [13] or determine the correct cochleostomy location [14]. The use of embedded sensors in surgical tools to provide localization within an augmented reality paradigm is becoming more available for real-time navigation of surgical devices. For example, Scopis Medical (Berlin, Germany) now has a suite of surgical tools where a magnetic sensor enables the location of the tool to be tracked. The sensor uses an electromagnetic-field source that can be mounted on an arm or placed underneath a head rest. This information is integrated into their software as a rendered virtual tool within a rendered model of the

anatomy.

This concept can be adapted to address some of the challenges in cochlear implantation. First, a rendering of the patient's anatomy, such as the cochlea, could be generated through segmentation of the patient's CT or MRI scans. This becomes the patient-specific environment in which the tool is visualized. Prior to drilling the cochleostomy or making the round-window incision, a flexible instrument equipped with a magnetic sensor can be placed near the area and visualized within the virtual environment for confirmation.

Similarly, a magnetic sensor can be placed at the tip of the electrode for real-time visualization inside a virtualization of the patient's cochlea. If the localization algorithm can provide full six degrees-of-freedom, the following benefits are possible. First, the surgeon can better visualize where the stylet should be stabilized inside the cochlea prior to advancing the electrode off of it. Second, the angular rotation about the electrode's long axis (i.e., the body roll angle) would enable the surgeon to know if a precurved electrode is misaligned. If this is the case, then the electrode should be rotated so that the precurved shape is aligned properly prior to being advanced off the stylet. This body roll angle would also be useful for lateral-wall-type electrodes with single-sided contacts. If the contacts are not directed toward the modiolus, then the electrode should be rotated so that this is achieved. Third, an augmented environment can be used by the surgeon to confirm intuitions about the electrode insertion itself. For example, if the surgeon feels larger-than-normal resistance, the visualization may provide additional information to aid in decision making regarding the electrode insertion.

7.8 References

[1] J. R. Clark, L. Leon, F. M. Warren, and J. J. Abbott, "Magnetic guidance of cochlear implants: Proof-of-concept and initial feasibility study," *J. Med. Devices*, vol. 6, no. 3, pp. 035002, 2012.

[2] J. Lee, J. B. Nadol, Jr, and D. K. Eddington, "Factors associated with incomplete insertion of electrodes in cochlear implant surgery: a histopathologic study.," *Audiol. Neurotol.*, vol. 16, no. 2, pp. 69–81, 2011.

[3] P. S. Roland, W. Gstöttner, and O. Adunka, "Method for hearing preservation in cochlear implant surgery," *Oper. Tech. Otolaryngol.*, vol. 16, no. 2, pp. 93–100, 2005.

[4] J. H. Noble, R. F. Labadie, O. Majdani, and B. M. Dawant, "Automatic segmentation of intracochlear anatomy in conventional CT," *IEEE Trans. Biomed. Eng.*, vol. 58, no. 9, pp. 2625–32, Sep 2011.

[5] G. B. Wanna, J. H. Noble, R. H. Gifford, M. S. Dietrich, A. D. Sweeney, D. Zhang, B. M. Dawant, A. Rivas, and R. F. Labadie, "Impact of intrascalar electrode location, electrode type, and angular insertion depth on residual hearing in cochlear implant patients: Preliminary results.," *Otol. Neurotol.*, vol. 36, no. 8, pp. 1343–1348, Sep 2015.

[6] S. A. Wade, J. B. Fallon, A. K. Wise, R. K. Shepherd, N. L. James, and P. R. Stoddart, "Measurement of forces at the tip of a cochlear implant during insertion.," *IEEE Trans. Biomed. Eng.*, vol. 61, no. 4, pp. 1177–1186, Apr 2014.

[7] Y. Nguyen, M. Miroir, G. Kazmitcheff, J. Sutter, M. Bensidhoum, E. Ferrary, O. Sterkers, and A. Bozorg Grayeli, "Cochlear implant insertion forces in microdissected human cochlea to evaluate a prototype array," *Audiol. Neurotol.*, vol. 17, no. 5, pp. 290–8, 2012.

[8] J. Pile and N. Simaan, "Characterization of friction and speed effects and methods for detection of cochlear implant electrode tip fold-over," in *IEEE Int. Conf. Robot. Autom.*, 2013.

[9] A. Coordes, A. Ernst, G. Brademann, and I. Todt, "Round window membrane insertion with perimodiolar cochlear implant electrodes," *Otol. Neurotol.*, vol. 34, no. 6, pp. 1027–1032, 2013.

[10] A. Jeyakumar, S. F. Peña, and T. M. Brickman, "Round window insertion of precurved electrodes is traumatic," *Otol. Neurotol.*, vol. 35, no. 1, pp. 52–7, Jan 2014.

[11] M. A. Souter, R. J.S Briggs, C. G. Wright, and P. S. Roland, "Round window insertion of precurved perimodiolar electrode arrays: how successful is it?," *Otol. Neurotol.*, vol. 32, no. 1, pp. 58–63, 2011.

[12] B. Chen, H. N. Kha, and G. M. Clark, "Development of a steerable cochlear implant electrode array," in *IFMBE Int. Conf. Biomed. Eng.*, 2007, vol. 15, pp. 607–610.

[13] P. S. Roland, C. G. Wright, and B. Isaacson, "Cochlear Implant Electrode Insertion: The Round Window Revisited," *Laryngoscope*, vol. 117, no. 8, pp. 1397–1402, 2007.

[14] O. F. Adunka and C. A. Buchman, "Scala tympani cochleostomy I: results of a survey," *Laryngoscope*, vol. 117, no. 12, pp. 2187–2194, 2007.

CHAPTER 8

CONCLUSIONS

A strategy to wirelessly guide the tip of a cochlear-implant electrode array using magnetic manipulation has been presented. We started with initial 3-to-1 proof-of-concept experiments to demonstrate the feasibility of this approach. Next, clinical, lateral-wall-type electrode arrays were slightly modified at the tip to include a tiny magnet. A scala-tympani phantom was designed with both simulated cochleostomy and round-window openings to mimic both classes of insertions typically conducted. In particular, it is the first phantom to model a round-window opening and can be used reliably to simulate insertion forces in cadaver cochleae.

Magnetically guided insertions through these phantoms demonstrated statistically significant ($p < 0.05$) reduction in insertion forces, by as much as 50% for some electrode-array models. In particular, guiding the electrode-array tip through the cochlear hook and the basal turn, in the same insertion, was demonstrated for the first time using this technology. Current technology can only steer the electrode array through the basal turn.

Finally, analysis was conducted to determine the optimal size and placement of a magnetic dipole-field source for use in the clinic. Its placement was determined to be consistently lateral to and anterior to the patient's cochlea. Its size depended on numerous factors including the patient, torque requirements, and registration error; sensitivity curves were provided to summarize these factors. By moving the magnetic dipole-field source from the modiolar configuration originally proposed to the optimal configuration, the magnetic volume can be reduced by a factor of 5 on average. At the optimal configuration, it was verified that magnetic forces do not pose any appreciable risk to the basilar membrane. Although patient-specific optimal configurations were characterized, a one-size-fits-all version was described that may be more practical and carried the benefit of substantial robustness to registration error.